# DENDRIMER-BASED TARGETED THERAPY FOR THE TREATMENT OF CNS DISEASES

by

Fan Zhang

A dissertation submitted to the Johns Hopkins University in conformity with the requirements for the degree of Doctor of Philosophy

Baltimore, Maryland

April 2016

# Abstract

Effective treatment of many CNS diseases remains a major challenge due to the lack of specificity for therapeutics to target pathological cells. Many nanoparticles offer promising approaches for controlled, sustained release of therapeutics, yet their applications are limited by the lack of knowledge on how they interact with pathological cells. Microglial cells play a key role in mediating the development of many CNS diseases. In this thesis, we investigated the mechanism for Polyamidoamine (PAMAM) dendrimers (dendrimers) to target microglial cells in different pathologies (e.g. malignant brain tumor, neuroinflammation) that are commonly observed in many CNS diseases. Building from this knowledge, we developed dendrimer-based therapeutics that can target microglia and improve therapeutic efficacy in CNS diseases.

We first determined the mechanism for dendrimers to target microglia in malignant brain tumor and neuroinflammation. In malignant brain tumor, we found systemically delivered dendrimers can target tumor and Tumor Associated Macrophages (TAMs) within 15 minutes and 4 hours respectively after administration. In the presence of neuroinflammation, dendrimers can cross the Blood-Brain Barrier (BBB) and selectively localize in 'activated' microglia at different stages of activation. Further *ex vivo* study revealed that, although these 'activated' microglial cells had impaired movement, they tended to take up dendrimers more rapidly and to a greater extent compared to the microglia under physiological conditions.

We then sought to investigate the physiochemical properties of dendrimer that can affect its intrinsic targeting to the CNS diseases. We found increase dendrimer size from generation 4 (G4) to generation 6 (G6) can increase its tumor uptake 100-fold, while still maintaining its intrinsic targeting to TAMs. Cationic dendrimers demonstrated the highest brain accumulation,

following with neutral and anionic dendrimers, yet only neutral dendrimers were able to diffuse within the brain parenchyma and target 'activated' microglia.

Based on these design criteria, we formulated therapeutic dendrimer through covalently conjugating a glutamate carboxypeptidase II inhibitor (i.e. 2MPPA) to dendrimers (D-2MPPA), using disulfide bond as a linkage. When evaluated in a clinical translatable rabbit model of cerebral palsy, D-2MPPA demonstrated higher brain accumulation and specific glial cell-targeting compared with free 2MPPA. This targeted delivery efficiently inhibited glutamate excitotoxicity, attenuated neuroinflammation, and subsequently improved neurobehavior, with clinical significance.

Advisor: Kannan Rangaramanujam, Ph.D.

Readers: Kannan Rangaramanujam, Ph.D., Sujatha Kannan, M.D., Justin Hanes, Ph.D.;

Hai-Quan Mao, Ph.D., Honggang Cui, Ph.D.

## Acknowledgements

I would like to express my gratitude to my advisor: Dr. Kannan Rangaramanujam who not only gave me precious advice on science, but also passed on a positive and optimistic attitude toward life. His mentorship helped me through many problems in my research, and encouraged me to pursue higher levels in science. I would also like to thank Dr. Sujatha Kannan, who opened the door of medicine to me. Her guidance and trust were critical to the establishment of my Ph.D. work.

Dr. Elizabeth Nance, Dr. Manoj Mishra, and Dr. Wojciech Lesniak were senior lab members, who I was lucky enough to closely work with. Dr. Elizabeth Nance gave me tremendous training in how to conduct research as an engineer, especially in a field involving many different disciplines. Dr. Mishra and Dr. Lesniak brought their expertise in organic chemistry and analytical chemistry in the earlier training of my research, which helped me in developing key research techniques forming the basis of my work.

I have collaborated with many people in my Ph.D. research. Dr. Zhi Zhang, Dr.Panagiotis Mastorakos, Dr.Antonella Mangraviti, Dr.Yi-An Lin, Dr.Joshua Grimm, Dr.Yossef Alnasser, Dr.Betty Tylor, Dr.Irina Burd, and Dr.Mary Ann Wilson. I would not be able to achieve this progress without their help. I also appreciate Dr.Justin Hanes, Dr.Hai-Quan Mao, Dr.Jonah Erlebacher for their time and generosity to give guidance on my research.

I want to thank many fellows in Center for Nanomedicine: Dr.Clark Zhang, Jane Chisholm, Dr.Tao Yu, Kunal Parikh, Dr.Abhijit Date, Dr. Rajasekhar Reddy Rami Reddy, Dr.Siva Pramodh Kambhampati for many joyful moments in the lab.

Lastly, I want to thank David Cohen, Dr.Fengyuan Yang and my mother, Meixian Peng, my father Jinbo Zhang, my cousin Rong Peng and Zixuan Liu for their unconditional support in my

life. It is this support which helped me to go through the hard times, and will continue to support me to go further in life.

# Table of Contents

# List of Tables

# List of Figures

# 1. BACKGROUND AND INTRODUCTION[1]

## 1.1. Nanotechnology and CNS diseases

Achieving effective therapy for many diseases in the central nervous system (CNS) remains a great challenge. To date, clinical treatments for CNS diseases provide only limited improvement in outcomes and are often accompanied by severe side effects. For instance, patients diagnosed with glioblastoma only have a median survival period of 14 months following surgical resection, radiation, or concomitant chemotherapy [1]. The difficulty in achieving improved outcome for CNS diseases stems from the inability to deliver therapeutically relevant doses of the therapeutic to diseased cells or regions. The Blood-Brain Barrier (BBB) poses as the main obstacle that prevents most systematically administrated drugs from entering the CNS.

Nanomedicine offers great potential for improving the therapeutic efficacy or diagnosis efficiency in the clinical settings for many CNS disorders. The use of nanoparticles as drug delivery vehicles is not only widely reported in pre-clinical studies but is now also being implemented in clinical applications. While the entry of drugs to the brain is highly restricted, drug-carrying nanoparticles can significantly improve the CNS pharmacokinetics and biodistribution relative to free drugs [2]. Recent discoveries have shed more light on the CNS disease pathology at the cellular or even molecular level, and have greatly impacted the design of nanomedicine to target specific cell populations in the CNS. This review will describe the pathological roles of major CNS cells (such as neurons, microglia/macrophage, astrocytes, endothelial cells, and brain tumor cells) in CNS disorders. We will then focus on recent advances

[1] Parts of this chapter appears in F. Zhang, Y.A. Lin, S. Kannan, R.M. Kannan, Targeting specific cells in the brain with nanomedicines for CNS therapies. ***J Control Release***, 2015 Dec 11. pii: S0168-3659(15)30265-0.

of nanomedicine design that have been implemented to target specific cell populations in the CNS.

## 1.2. Blood-brain barrier under physiological and pathological conditions

### *1.2.1 BBB under normal physiology*

The BBB is composed of endothelial cells adjoined with tight junctions which act as physical barriers and constrain the passage of most molecules through the barrier to transcellular trafficking. More than 98% of small molecular drugs and almost 100% of large-molecules (>500 Da) are simply excluded from CNS because they cannot cross the BBB [3]. It not only functions as a protective obstruction that blocks possible neurotoxic substances from CNS but also mediates several important functions, such as i) selectively transporting molecules that provides essential nutrients to the brain, ii) effluxing waste products, and iii) regulating homeostasis in the brain [4].

Small molecules are known to pass through endothelial cells by passive diffusion (for lipophilic molecules) or by active transport (as in the case of required nutrients into the brain, such as glucose, amino acids, nucleosides, or nucleobases) [4]. Small lipophilic molecules (<400 Da) exhibit certain abilities to pass the BBB by passive diffusion through the endothelial cells [5]. Unfortunately, many therapeutic molecules do not belong to this category. Most hydrophobic substances over 400 Da fail to enter the brain through this mechanism, often due to the efflux system regulated by ATP-binding cassette (ABC) transporters [5, 6]. These transporters are protective mediator that actively exclude possible neurotoxic substances from entering the CNS and are expressed on the endothelial cells. For instance, P-glycoprotein, an ATP-dependent transport protein localized in the blood luminal membrane, deters the entry of potentially toxic substances by pumping them back to the blood. While many small molecular

drugs are substrates of ABC transporters, they possess fairly limited capabilities of entering the brain.

Large molecules, peptides or proteins, are incapable of passive diffusion across the BBB. Thus, their preferred mode of transport is through transcytosis, given that endothelial cells at the BBB exhibit much lower activity of internalization compared with other endothelia [4]. This mechanism involves either adsorptive-mediated (non-specific) or receptor-mediated (specific) transcytosis to allow macromolecules, captured in vesicles, to be internalized by endothelial cells and eventually exocytosed into the brain [4]. Adsorptive transcytosis involves endothelial internalization induced by non-specific binding caused by the interaction between cell surface and excess positive charges on the macromolecules. Some cationic proteins or peptides, such as cationic albumin, undergo this type of pathway to cross the endothelial cells [7]. On the other hand, internalization of substances can also occur by receptor-mediated transcytosis when ligands interact with their respective endothelial membrane receptors, such as transferrin receptor (TfR), melanotransferrin receptor (MTfR), lactoferrin (LfR), or LDL-receptor-related proteins [8, 9, 10, 11]. Researchers that have designed nanomedicines in an attempt to increase drug delivery to the brain have heavily considered these two pathways, as discussed later.

### *1.2.2 BBB under pathological conditions*

Dysfunction of BBB endothelial cells is an important feature in many CNS pathologies [12]. This dysfunction is often associated with neuroinflammation which leads to alternation of permeability of the BBB. Under these conditions, the tight junctions between endothelial cells are disrupted, which enables additional substances to cross BBB or permits circulating macrophages to infiltrate into the CNS (Figures 1.1 and 1.2). This permeability change can be observed in neuroinflammation initiated by bacterial lipopolysaccharides (LPS), or in disease

pathologies for stroke, traumatic brain injury, MS, and brain tumors [4, 13]. However, the degree of impairment is controlled by the pathology of different diseases, and the severity of the disease and the maturation of blood brain barrier. [14] In brain cancer, the poorly developed BBB leads to the formation of gaps and extensive fenestration [15]. As a result, an increased permeability of BBB was observed. As one of the main characteristics of brain tumor, the leakage of blood brain tumor barrier (BBTB) is highly heterogeneous, significantly difference was reported between tumor core and tumor border [16] and the upper limit of gaps in BBTB can varied from 20-100nm [17]. In some diseases such as AD or PD, the BBB permeability is altered due to decreased level of P-glycoprotein expression, which lowers the efficiency of efflux pumps in transporting neurotoxic substances back to the blood [18, 19, 20, 21, 22]. In brief, the altered properties of blood brain barrier created opportunities for delivering therapeutics across BBB and reach the pathologic location, however, to better take advantage of this, a thoroughly understanding of nanoparticles relation with BBB is required.

## 1.3. Microglia and their role in CNS diseases

### *1.3.1. Microglia in Neurodegenerative Diseases*

The CNS possesses a distinctive immune system since circulating immune cells cannot access to the CNS in physiological conditions. Microglial cells serve as the major resident immune cells in the CNS where they constantly monitor their surroundings and act as the mediator in innate immunity for early control of infections [23, 24]. They serve as key therapeutic targets because their functions are closely associated with the pathologies of many CNS disorders, including ischemic stroke, traumatic brain injury, spinal cord injury, AD, Parkinson's disease (PD), amyotrophic lateral sclerosis (ALS), multiple sclerosis (MS), and most types of brain tumors [23, 24, 25, 26, 27, 28, 29]. Under normal conditions, quiescent microglial

cells constantly survey their surroundings, providing a defense mechanism for the brain. Upon sensing pathogen invasion or tissue damage, they rapidly switch to the activated phenotype that secretes cytokines to initiate secondary inflammatory responses. (Figure 1.1). This phenotype change of microglia, characterized by a morphological change from ramified form to amoeboid form, is often induced by the recognition of pathogen-associated moieties by toll-like receptors (TLRs), a family of receptors that plays a role in both innate and adaptive immunity [23, 24]. When recognizing stimuli by such receptors, microglia can produce cytokines to stimulate either pro-inflammatory or anti-inflammatory responses. It should be noted that the termed "activation" could indicate a range of activated states for microglia, broadly divided into two main phenotypes, M1 and M2, as indicated in other reviews [30, 31]. Activated microglia in the M1 state, or also called "classically activated", promote the production of inflammatory cytokines, such as TNF-α, IL-1β, or IL-6 [23, 24]. On the other hand, M2 microglia contain phenotypes which suppress inflammation by cytokines TGF-β or IL-10 (M2a phenotype), or assist tissue remodeling and matrix deposition (M2c phenotype) [30]. The dynamic between M1 and M2 phenotypes of microglia enables the response to early stages of infection and is responsible for the clearance of cellular debris. However, in many pathological conditions, pro-inflammatory effects can persistently dominate without effective anti-inflammatory responses. For example, M1 microglia may release cytotoxic nitric oxide (NO), reactive oxygen species (ROS), or excessive cytokines (such as TNF-α) that cause neurotoxicity and lead to the injury/death of neurons, oligodendrocytes, and/or damage extracellular matrix [31].

Dysfunction of microglial responses has been observed in CNS diseases associated with both acute and chronic neuroinflammation. In acute inflammation, such as ischemic stroke, spinal cord injury, or traumatic brain injury, microglia activation is triggered by mechanisms that

cope with damage-associated molecular pattern molecules (DAMPs) released from injured cells or cellular necrosis processes [32, 33]. Though this is a crucial step for tissue repair, a failure of follow-up anti-inflammation responses in these instances can result into more damages. As stated before, this activation (dominated by M1 phenotype) could lead to over-production of cytotoxic NO and ROS, which exacerbate the cellular death, or cytokines (for example, IL-1, IL-6, and TNF-α) that amplify inflammation response [34]. Chronic inflammation, in contrast to acute inflammation, is a self-propagating inflammatory response initiated from certain stimuli. This process generally starts from an initial microglia activation, which further develops into increased inflammation and glial activation when M2 responses occur and fail to exert their neuroprotective roles [30]. M1 microglia participates in the chronic inflammation of many neurodegenerative diseases, including AD, PD, ALS, or MS [29, 35, 36, 37]. In these instances, microglia respond to stimuli, such as aggregation of Aβ in AD and α-synuclein in PD, motor neuronal death in ALS, or signals from infiltrating lymphocytes in MS; and further produce more NO, ROS, proinflammatory cytokines (such as TNF-α, IL-1β, IL-6) that eventually cause progressive injury to other neurons/astrocytes without appropriate neuroprotective effects from M2 phenotypes [29, 30, 31, 38, 39, 40, 41]. Since this cascade is often accompanied with BBB impairment in pathology, circulating macrophages can possibly infiltrate into the CNS and function similarly to microglial cells to amplify the inflammatory responses.

The production of proinflammatory cytokines and neurotoxic substances from microglia/infiltrating macrophages are linked to several pathways, including, but not limited to, the activation of NOX2 complex (an NADPH oxidase), mitogen-activated protein kinase (MAPK), and sphingosine kinase 1 (Sphk1) as detailed elsewhere [42, 43, 44]. In general, these pathways can be stimulated by variety of disease proteins (Aβ precursor protein, α-synuclein,

myelin), LPS, cytokines (TNF-α, IL-1β, IL-4, IL-13), or environmental toxins. Since these pathways account for the production of neurotoxic molecules, inhibition of these pathways in microglia can possibly promote neuroprotective effects. For example, inhibition of NOX2 or p38 MAPK by treating dexamethasone or minocycline could attenuate the activation of microglia, as well as the production level of NO and IL-1β [43, 45, 46]. Dimethylsphingosine, an inhibitor of Sphk1, reportedly suppresses the expression of proinflammatory cytokines including TNF-α, IL-1β, and the production of NO of microglial cells [44]. But to optimize the therapeutic effects, these potent drugs require specific, effective delivery to microglia/infiltrating macrophages.

### *1.3.2. Tumor-Associated Microglia/Macrophages in Tumor Microenvironments*

Tumor-associated microglia and infiltrating macrophages (TAMs) pose as important mediators in CNS cancer (Figure 1.2). Various studies regarding the synergic effects between TAMs and gliomas that allow them to co-exist have been reviewed previously [25, 47]. TAMs can be recruited by gliomas by chemokines, cytokines, or matrix metalloproteinases (MMPs)[25]. Although TAMs may polarize to M1 phenotype to give rise to pro-inflammatory effects (for initiating the clearance of potential hazards in CNS), their inflammatory functions are often suppressed in glioma pathology [27, 47, 48, 49, 50]. Gliomas produce anti-inflammatory cytokines such as IL-10, IL-4, IL-6, and TGF-β [25], where tumor cells are able to establish an immunosuppressive microenvironment after recruiting TAMs. Under such condition, TAMs are instead polarized to the M2 phenotype that reduces classic neuroinflammation, and allows further tumor progression [25, 47]. In addition, TAMs themselves can also secrete cytokines (TGF-β) and MMPs (MMP-2, MMP-9, and MT1-MMP) that promote tumor growth and invasion [51, 52, 53, 54]. These findings suggest TAMs can serve as a crucial target, as their pathological functions are strongly associated with tumor cells. Delivering therapeutics to alter

the functions of TAMs or using TAMs as delivery vehicles could potentially provide an effective approach for the treatment of brain tumors.

## 1.4. Polyamidoamine (PAMAM) dendrimers and dendrimer-based drug delivery

### *1.4.1. Introduction to PAMAM dendrimer-the physical and chemical properties*

Dendrimers are branched polymeric molecule with nanoscale size (between 3 to 20nm), nearly monodispersity (polydispersity index close to 1.0), and well-defined architecture. The name 'dendrimer's is a figurative representation of dendrimer's tree like branched structure with 'dendros' meaning tree and 'meros' meaning part. The structure of dendrimer usually consists of a repetitive sequence of monomers, called branching units (dendrons); a core unit where the branching units are growing from in a radial iterative fashion; and a terminal group which is at the end of growing branching units. This controlled step-by-step synthesis contributes to dendrimer's extremely controllable physical and chemical properties [55, 56].

Among the large dendrimer family, Polyamidoamine (PAMAM) dendrimer is the most extensively characterized and widely used, and it is the first commercialized dendrimer. They are synthesized via Michael addition of amino groups of ethylene diamine (EDA) core with methyl acrylate (branching unit), followed by amidation of the resulting esters with EDA, forming generation 0. Repetition of these two synthetic steps leads to next generations. The size of dendrimer grows linearly in diameter as a function of generations, with an increase of ~1nm for each generation. While the surface functional group and molecular weight gets doubled as the increase of generation [55].

PAMAM dendrimers have high density of surface functional groups that can be tailored. For example, the surface ζ potential of dendrimers can vary from positive to negative as the surface functionality change from amine (13.94±1.5 mV) to hydroxyl (−3.4±1.2mV) and carboxyl

(−13.0±1.1mV) [57]. Although PAMAM dendrimers have globular structure in general, their conformation change with the chemical environment such as pH, ionic strength and the polarity of solvent, especially the pH level. Under low pH (~3) environment, the protonated amine groups will lead the whole structure to a more extended conformation due to the electrostatic repulsion between the positively charged $NH_3^+$ groups; under neutral pH, backfolding occurs due to the uncharged interior tertiary amine and the charged surface primary amine, while at basic pH the higher backfolding effect will lead to a more globular confirmation [58].

*1.4.2. Dendrimer as drug delivery vehicle*

The highly tailorable surface functional groups and comparatively hydrophobic core make it possible to either modify the surface or conjugate/complex therapeutics or encapsulate them. Specifically, many studies conjugate drugs to the terminal functional groups of dendrimer through covalent bond using different linking chemistry; the surface of positively charged amine terminated dendrimer can also be used to complex with negatively charge gene therapies; modify the surface of dendrimer using polyethylene glycol (PEG) or targeting ligand such as folic acid can help to achieve desired biological effect. Moreover, the interior of dendrimer can be used to physically entrap guest molecules to achieve drug delivery function. These features make dendrimer ideal drug carriers with high drug payload capacities [59].

PAMAM dendrimers also possess the good barrier penetrating properties to many biological barriers such as the intestines, the blood-tissue barriers and so on. Take the transepithelial property of dendrimer for example. Studies have shown PAMAM dendrimer are transported by a combination of paracellular and transcellular routes, in which dendrimer can open the tight junctions of epithelial barriers (paracellular transport), and enter/leave the cell through a variety of endocytic mechanisms (transcellular transport) [60]. The first evidence of dendrimer targeting

penetrating BBB *in vitro* was observed by Bhadra using PEGylated Generation 4 PAMAM dendrimer [61]. The mechanism behind dendrimer's BBB penetrating property was suggested in later studies: 1) the high density of surface charge can interact with BBB endothelium and cause the disruption; 2) the nanoscale of dendrimer enhanced the entry of dendrimer and by inhibiting the efflux P-glycoproteins [62].

The toxicity of PAMAM dendrimer is associated with many of their physical properties such as size, shape and chemical properties such as the surface functional groups [63]. In PAMAM dendrimer, amine terminated generation 4 dendrimer (G4-$NH_2$) have a higher dose dependent *in vivo* toxicity than hydroxyl terminated dendrimer of same generation (G4-OH). [64, 65, 66] G4-$NH_2$ showed toxicity at dose of 30 mg/kg, while G4-OH showed toxicity only at dose of 1000 mg/kg [58]. The result in this *in vivo* study is consistent with previous *in vitro* studies, which reported that cationic dendrimers are cytotoxic and can destabilize cell membrane, cause cell lysis [67, 68]. Similar studies also focused on the size/generation dependent *in vivo* toxicity of PAMAM dendrimer. For PAMAM dendrimer, higher generation in general exhibits higher toxicity. [58, 60, 61, 69]. These results are in agreement with the results of *in vitro* size/generation depend cytotoxicity studies [65, 66]. However, *in vitro* studies can only give relative index of potential toxicity of PAMAM dendrimers. The ultimate toxicological profile will depend on its pharmacokinetics study *in vivo*. Previous studies on amine terminated PAMAM dendrimer showed G7-$NH_2$ has a higher accumulation in the liver while most G4-$NH_2$ was eliminated by the renal clearance. This result in biodistribution explains the data in toxicity in same study, which indicates that the hepatic hemorrhage and hemobilia after G7-$NH_2$ administration is related to high liver accumulation [58]. Except for surface charge, dendrimer

chemistry and generation/size, some other factors such as administration routes, animal model can also influence the result of dendrimer toxicity.

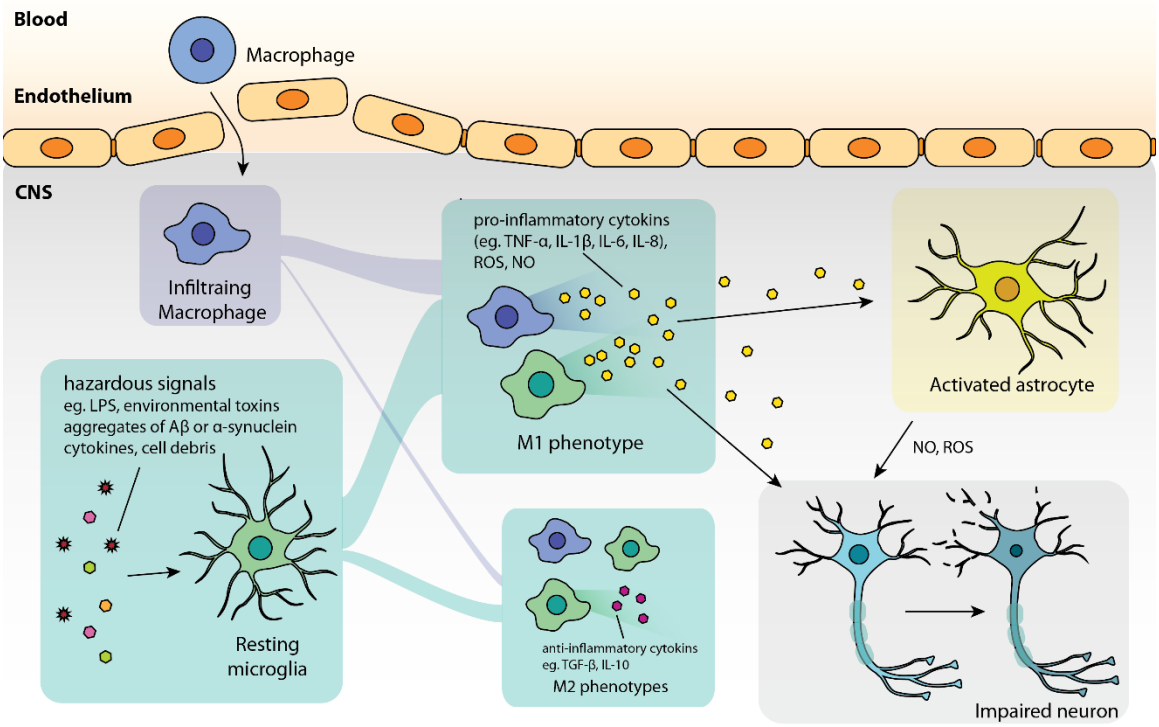


**Figure 1.41. Common features in neuroinflammation.**

In general, microglial cells are initially activated by injury signals, such as damage-associated molecular pattern molecules and cell debris from damaged cells in acute inflammation, aggregates of Aβ in Alzheimer's disease, α-synuclein aggregates from abnormal dopaminergic neurons in Parkinson's disease, SOD1 aggregates from diseased neuron in amyotrophic lateral sclerosis. In such pathologies, microglia (together with infiltrating macrophages) tend to polarize to M1 phenotype that amplifies neuroinflammation by producing pro-inflammatory cytokines (TNF-α, IL-1β, IL-6) as well as ROS and NO which lead to neuronal injury. Some pro-inflammatory cytokines (such as TNF-α, IL-1β) can also activate astrocytes to induce over-production of ROS and NO that exacerbate the injury. The impaired neurons are then susceptible to undergo apoptosis or necrosis, which, in turn, release molecules that further activate microglia.

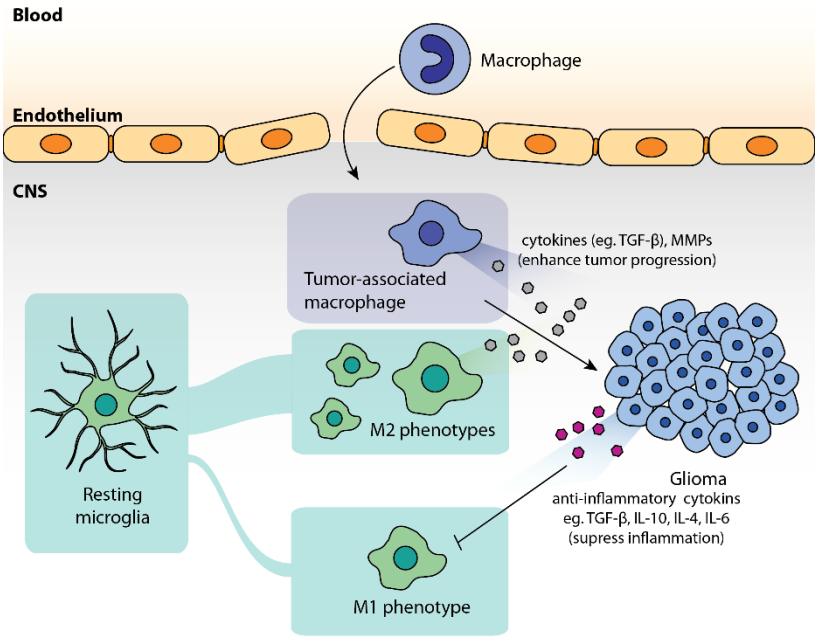


**Figure 1.42. Role of tumor-associated microglia/macrophages and tumor cells in tumor microenvironment.**

Glioma cells generally create an environment that suppresses classic inflammation (or, the functions of M1 phenotypes of microglia/infiltrating macrophage) by cytokines such as TGF-β, IL-10, IL-4, IL-6. Microglia/macrophages, under such circumstance, are polarized to M2 phenotypes and produce cytokines (TGF-β) or MMPs that are associated with tumor progression.

# 2. SYSTEMIC DENDRIMERS TARGET BRAIN TUMORS AND TUMOR ASSOCIATED MACROPHAGES (TAMS)[2]

## 2.1. Introduction

Malignant glioma is the most common and most aggressive primary brain tumor [70] and despite the advances in treatment, the median survival remains at 16.4 months [71]. Key challenges faced in the development of effective therapies relate to (a) the ability of systemically delivered chemotherapeutic agents to penetrate the impaired blood-brain tumor barrier (BBTB) and provide coverage across the entire solid tumor [72] and (b) the ability to target specific cells. Although small molecule-based therapeutics can effectively distribute within the tumor tissue, they are limited by rapid tumor clearance [73] and off-target extravasation, potentially leading to adverse effects [72]. Recent advances in nanotechnology have provided selective tumor accumulation. However, the size of most nanoparticles limits extravasation and tumor penetration, thus limiting homogeneous solid tumor coverage [72, 74]. Careful tuning of particle size and surface charge has been attempted in order to enhance the nanoparticle distribution profile in subcutaneous tumors [75], [76], [77, 78]. Unfortunately, achieving homogeneous coverage of orthotopic brain tumors has been proven even more challenging. This may be attributed to the lower permeability of the BBTB compared to the blood-tumor barrier (BTB) in a subcutaneous tumor, the heterogeneous intervascular spaces and the high interstitial pressure in brain tumors. Although, some strategies have attempted nanoparticle delivery through the BBTB

[2] Parts of this chapter appears in F. Zhang, P. Mastorakos, M.K. Mishra, A. Mangraviti, L. Hwang, J. Zhou, J. Hanes, H. Brem, A. Olivi, B. Tyler, R.M. Kannan, Uniform brain tumor distribution and tumor associated macrophage targeting of systemically administered dendrimers. ***Biomaterials***, 52 (2015), pp. 507–516

via absorptive uptake; passive diffusion through the leaky BBTB fenestrations has only been demonstrated with molecules smaller than 20 nm [79, 80, 81, 82] and unhindered diffusion through the BBTB has been achieved with molecules of 7 nm [83], thus limiting the relevance of most nanoparticle-based therapeutics.

Hydroxyl-terminated generation 4 polyamidoamine (PAMAM G4-OH) dendrimer is a highly tailorable branched macromolecule with a hydrodynamic size (~4 nm) smaller than conventional nanoparticles and near-neutral surface charge (ζ-potential: +4.5 ± 0.1 mV), physicochemical attributes that may allow for effective BBB [84] and tumor extra cellular matrix (ECM) penetration [85]. We have previously shown that, without the use of targeting ligands, these dendrimers can target activated microglia/macrophages after passing the impaired blood-brain barrier (BBB) in a rabbit model of cerebral palsy [86]. This targeted accumulation resulted in a significant efficacy when the dendrimer was conjugated to N-acetylcysteine [86]. In glioma, tumor associated microglia/macrophages (TAM) have been shown to participate in tumor growth, tumor invasion, angiogenesis and immune system evasion [47]. A variety of microglia/macrophage modulating molecules has been shown to decrease glioma progression and increase survival in preclinical studies [87], [88], [89, 90]. Therefore, nanoparticle targeting of TAM has been explored, through the use of different ligands [91], [92], [93, 94].

We investigated the use of PAMAM G4-OH dendrimer as a promising therapeutic vehicle for the treatment of malignant glioma. A recently developed fluorescence-based ‘quantification’ approach and high resolution confocal microscopy were combined to investigate the kinetics, biodistribution and clearance of these dendrimers in a 9L gliosarcoma intracranial tumor model. We also characterized the dendrimer’s intrinsic ability to selectively target TAM.

## 2.2. Materials and Methods

### *2.2.1. Materials and reagents*

The following agents were purchased: hydroxyl terminated ethylenediamino-core PAMAM dendrimer (referred to as dendrimer throughout, unless otherwise specified) (Dendritech, Midland, MI), Methanol (HPLC grade), DMF (HPLC grade), stainless steel beads (Fisher Scientific, Waltham, MA); and Cyanine 5 (Cy5) (GE Healthcare Life Science, Pittsburgh, PA). For confocal microscopy: nuclei counterstain, 4',6-diamidino-2-phenylindole, dihydrochloride (DAPI), Alexa Fluor® 594 Goat Anti-Rabbit IgG (H+L) Antibody (Molecular Probes, Eugene, Oregon); Fluorescent mounting media (Dako, Santa Clara, CA); Anti-Iba1, Rabbit (Wako, Osaka, Japan); Lectin from Bandeiraea simplicifolia (BSI-B4) (Sigma-Aldrich, St. Louis, MO); Anti-GFAP 488 (eBioscience, San Diego, CA); Fluorescein isothiocyanate–dextran (FITC-dextran), average molecular weight 70,000 Da (Sigma Aldrich, St. Louis, MO).

### *2.2.2. Synthesis of dendrimer Cy5 (D-Cy5) conjugates*

D-Cy5 was prepared through two steps following a previously published method [95]. Briefly, hydroxyl-terminated PAMAM dendrimer was surface-modified with amine groups to make a bifunctional dendrimer. We used 6-(Fmoc-amino)caproic acid to produce a Fmoc-protected bifunctional dendrimer intermediate that was eventually de-protected by re-dissolving in a mixture of piperidine/DMF. Cy5 dye with N-hydroxysuccinimide monoester was reacted with amine groups on the surface of bifunctional dendrimer. The ‘crude’ products were further extensively purified by dialysis. The final D-Cy5 conjugate was characterized using 1H NMR, high-performance liquid chromatography (HPLC) and gel permeation chromatography (GPC).

The conjugate was stored as a solid powder at -20 °C and reconstituted at 10 mg/mL with sterile 0.9% NaCl solution on the day of administration.

### *2.2.3. Tumor inoculation*

Female Fischer 344 rats, weighing 125-175 g each (Harlan Bioproducts, Indiana, IN), were housed in standard facilities and given free access to food and water. 9L gliosarcoma intracranial implantation was performed as previously described [96]. Briefly, the 9L gliosarcoma (obtained from the Brain Tumor Research Center, UCSF, San Francisco, CA) maintained in the flank of F344, was surgically excised sectioned into 1 mm3 pieces and placed in sterile 0.9% NaCl solution on ice for intracranial implantation. Rats were anesthetized and a midline scalp incision was made to identify the sagittal and coronal sutures. A burr hole was made 3 mm lateral to the sagittal suture and 5 mm posterior to the coronal suture. The dura was incised, and using a surgical microscope and gentle suction a small cortical area was resected. A tumor piece was placed in the resection cavity and the skin was closed using surgical staples. All animals were treated in accordance with the policies and guidelines of the Johns Hopkins University Animal Care and Use Committee.

### *2.2.4. D-Cy5 administration for quantification and immunofluorescence*

Animals were injected in tail vein with a 3 mg/300 μL dendrimer-Cy5 solution. For imaging of dendrimer and dextran distribution, 3 animals were co-injected with a 0.9% NaCl solution of 2 mg D-Cy5 and 2 mg dextran-FITC in 300 μL.

To study the dynamics of dendrimer accumulation in the tumor brain, D-Cy5 was injected into 27 tumor inoculated rats when the average tumor size was 6 mm in diameter and then animals were sacrificed at fixed time points (15 min, 1hr, 4 hr, 8 hr, 24 hr, and 48 hr). Magnetic

resonance imaging was used to measure intracranial tumor size. Blood was drawn through cardiac puncture and immediately centrifuged to collect plasma. Brains were harvested and flash frozen on dry ice for fluorescence spectroscopy based quantification or placed in 4% formalin solution for immunofluorescence.

To study the dendrimer cell uptake, D-Cy5 injection was performed in 3 tumor inoculated rats and 3 healthy rats, and animals were sacrificed 24 hr after the injection. Brains were harvested and placed in 4% formalin for immunofluorescence study.

To study the pharmacokinetics and biodistribution of dendrimer in plasma and systemic organs D-Cy5 was injected into 15 tumor-inoculated rats which were placed in metabolic cages for urine collection and animals were subsequently euthanized at fixed time points (15 min, 1hr, 4 hr, 8 hr, 24 hr, and 48 hr). Organs were harvested and flash frozen on dry ice for fluorescence spectroscopy-based quantification or placed in 4% formalin for immunofluorescence.

*2.2.5. Fluorescence spectroscopy*

Fluorescence-based quantification of D-Cy5 conjugates followed our previously published protocol [95]. Briefly, 100-150 mg of frozen tissue was homogenized in 1 mL of methanol using a homogenizer (TissueLyser LT, Giagen) in 2 mL DNA LoBind Eppendorf tubes and subsequently sonicated. Suspensions were diluted to 100 mg/mL and centrifuged at 15,000 rpm for 15 min at 4 °C. The resulting supernatants were subjected to fluorescence spectroscopy. Importantly, prior studies showed that D-Cy5 was stable in plasma, and could be recovered from the tissue intact, without appreciable release of the conjugated Cy5 [95].

For brain tissue, precise dissection of the tumor was performed and the peritumoral area was defined as up to 1 mm away from the tumor dissection plane. In the contralateral hemisphere 100 mg of the caudate/putamen with the surrounding white matter area was dissected and used

for analysis. For plasma and urine samples, a sample of 100 µL of plasma and urine was mixed with 900 µL of phosphate buffer (0.1 M) and analyzed by fluorescence spectroscopy.

Fluorescence spectra of D-Cy5 conjugates and that obtained from tissue extracts were recorded using a Shimadzu RF-5301 Spectrofluorophotometer (Kyoto, Japan). D-Cy5 calibration curves were constructed, following every experiment, under different slit widths using the maximum emission wavelength of 662 nm after recording spectra from 650 nm to 720 nm with excitation wavelength of 645 nm. The D-Cy5 concentration was measured in methanol or phosphate buffer (0.1 M) in solutions ranging from 1 ng/mL to 100 µg/mL. The slit width was chosen based on the observed fluorescence level of different sample sets. For biological samples with low levels of D-Cy5 (i.e. brain, lung, heart), the excitation and emission slit width was set at 10; for biological samples with high levels of D-Cy5, (i.e. urine and kidney) excitation and emission slit width was set at 3. For the remaining biological samples, excitation slit width of 5 and emission slit width of 10 were used. All calibration curves exhibited linearity with R2 ~ 0.99. Fluorescence registered from tissue of non D-Cy5 injected healthy and tumor inoculated rats was subtracted from the values observed from samples of D-Cy5 injected tissue in order to account for tissue autofluorescence.

Concentration of D-Cy5 conjugate in the brain was expressed in µg per g of tissue. The concentration of D-Cy5 conjugate in the other organs was expressed in percentage (%) of injected dose per gram of tissue or % of injected dose per organ. Concentrations of the D-Cy5 conjugate in urine and blood were expressed in % of injected dose per mL or % of injected dose in total amount of urine or plasma. Total plasma concentration was calculated based on the weight of the animal. The brain and plasma quantification data were analyzed to calculate the AUC and the brain to serum ratio.

Concentration of D-Cy5 conjugate in the brain was expressed in µg per g of tissue. The concentration of D-Cy5 conjugate in the other organs was expressed in percentage (%) of injected dose per gram of tissue or % of injected dose per organ. Concentrations of the D-Cy5 conjugate in urine and blood were expressed in % of injected dose per mL or % of injected dose in total amount of urine or plasma. Total plasma concentration was calculated based on the weight of the animal. The brain and plasma quantification data were analyzed to calculate the AUC and the brain to serum ratio.

*2.2.6. Immunofluorescence*

Freshly harvested tissues were fixed in 4% formalin for 24 hr, followed by a gradient of sucrose solutions before cryosection. Tissues were then sectioned transversely into 30 µm-thick slices using a Leica CM 1905 cryostat. Slices were stained with DAPI (nuclei), rabbit anti-Iba1 antibody for microglia/macrophages, and goat anti-rabbit 595 secondary antibody. Some slices were stained with isolectin for endothelial cell staining. Slices were then imaged using a confocal LSM 710 microscope (Carl Zeiss; Hertfordshire, UK) under 5X, 20X, 40X and 63X magnifications. For each slice of tumor-inoculated brains, images where acquired for the tumor, tumor border and contralateral hemisphere. For control (non-tumor) brains, 1-3 representative images were acquired. Settings were optimized to avoid background fluorescence based on non-injected control rat brains. Laser power, pinhole, gain, offset and digital gain were selected separately for each magnification and kept constant throughout the entire study.

*2.2.7. Software*

For image processing ZEN 2011 software was used, any adjustments in brightness and contrast were kept constant throughout the same magnification images. No adjustments were done on the Cy5 channel. Imaris software was used for cell counting, co-localization and

microglia surface to volume ratio measurements. Microsoft Excel 2010 and KaleidaGraph 4.0 were used for all calculations, curve fitting and figure plotting related to the pharmacokinetic study.

*2.2.8. Cell count and co-localization*

For microglia/macrophage cell count 20X 13×13 tile scan images were analyzed and 3-5 slices were analyzed per region. The function 'spots' was used to identify Iba1+ microglia/macrophages. A diameter threshold of 4.15 μm was set to eliminate the objects smaller than microglia cells and an intensity threshold of 26.801 based on 'Quality' analysis was set to eliminate the background signal [97].

To study co-localization 40X, 4×4 tile scan images were used and 3-5 slides were analyzed per region. The function 'spots' was used to identify DAPI+ nuclei, Iba1+ microglia/macrophages and D-Cy5+ cells. For cells with D-Cy5 uptake, the spots with D-Cy5 and DAPI co-localization were counted; for microglia cells with D-Cy5 uptake, the spots with DAPI, anti-Iba1 and D-Cy5 co-localization were counted. Estimated diameters were applied to eliminate the spots with size smaller than cells, and signal thresholds were applied based on 'Quality' analysis. The function co-localize spots was used by counting the spots where D-Cy5 signal and cell signal are within 10 μm next to each other [97].

For surface to volume ratio analysis of the microglia cells, 3D representation of microglia morphology was acquired in confocal microscope using 40X magnification, with 3×3 tile scan, extending 10 μm in the z direction in z-stack. The function 'surfaces' was used and the individual Iba1+ microglia/macrophages were analyzed for surface and volume of each cell. Tumor area, ipsilateral (non-tumor area), contralateral area, and non-tumor brains were analyzed;

approximately 150 cells were included for each region. The threshold settings were based on the diameter of cells [98].

### *2.2.9. Statistical analysis*

Statistical analysis of data was carried out by student's t-test and one-way ANOVA followed by Games-Howell tests using SPSS 18.0 (IBM, Inc.), as needed. Differences were considered statistically significant at $p < 0.05$.

## 2.3. Results

### *2.3.1. Statistical analysis*

Based on fluorescence confocal microscopy, dendrimer-Cy5 conjugates (D-Cy5) rapidly accumulated throughout a 6 mm tumor, as early as 15 minutes after systemic administration. In the 'healthy' contralateral hemisphere, dendrimers outlined the blood vessels, and were not observed in the parenchyma (Figure 2.1A). Fifteen minutes after systemic administration, the dendrimers were dispersed throughout the entire intracranial tumor parenchyma. This distribution was not influenced by the heterogeneity in the tumor parenchyma (Figure 2.1B). There was no appreciable cellular uptake at this time point. At 4 hr post systemic dendrimer administration, the extracellular distribution in the tumor region had decreased, which was accompanied by an increased uptake by Iba1+ inflammatory cells (Figure 2.1C). The contralateral hemisphere showed relatively minimal D-Cy5 fluorescence at all-time points (Figure 2.1D,E).

In order to assess the kinetics of dendrimer accumulation in the brain, we used a recently developed fluorescence-based quantification method for D-Cy5. The use of the near IR Cy5

wavelength overcomes the tissue autofluorescence challenges [95]. The high sensitivity of this method (0.1 ng/g of tissue) allowed us to detect dendrimer accumulation at specific anatomic locations. In accordance with our confocal microscopy results, dendrimers rapidly accumulated in the tumor and peritumoral area within 15 min, with a peak concentration occurring at 8 hr (Figure 2.2A). Dendrimers gradually cleared from the tumor at a rate of ~0.01 μg/g/hr, and from the peritumoral area at a rate of ~0.007 μg/g/hr, reaching a concentration of 0.2 μg/g of tissue 48 hr after initial systemic injection (Figure 2.2A). In the contralateral hemisphere, the dendrimer accumulation also peaked at 8 hr, at a concentration ~ 8-fold lower than that found in the tumor area. At 24 hr, traces of dendrimer (0.03 μg/g) could be detected in the contralateral hemisphere and a ~14-fold higher accumulation in the tumor was observed (Figure 2.2A). At 48 hr the area under the curve (AUC) was 10 times higher in the tumor area in comparison to the contralateral hemisphere, indicating significantly higher ($p<0.05$) overall exposure of the dendrimer to the tumor (Figure 3.2B). The high and selective retention of dendrimer in the tumor and peritumoral area was visualized in a low magnification image of the tumor stained for astrocytes 24 hr following the administration of dendrimer (Figure 2.2C).

*2.3.2. Time dependent distribution of D-Cy5 in the brain tumor*

To study the dendrimer distribution in the tumor and peritumoral area, we co-injected D-Cy5 with linear dextran-FITC (70 kDa, ~6.5 nm radius) which has approximately twice the size of dendrimer. The tumor was clearly identified based on the increased density of DAPI-positive nuclei (Figure 2.3A). At each time point, the dendrimer distributed homogeneously throughout the whole tumor region (Figure 2.3B). In comparison, signal from dextran-FITC was only observed around the tumor border and not in the tumor core, even though the laser power and gain settings were maximized to detect the background signal in the FITC channel (Figure 2.3C).

Higher magnification images showed that D-Cy5 rapidly distributed and delineated the ECM leading to a reticular pattern of distribution and gradual accumulation in the cells (Figure 2.3D). On the contrary, dextran showed limited distribution throughout the ECM but high signal could be seen within the blood vessel lumen fifteen minutes after injection. At later time points, limited amounts of dextran were retained in the tissue presumably due to low cellular uptake (Figure 2.3E).

*2.3.3. Characterization of tumor associated microglia/macrophages and cellular uptake of dendrimer*

Gliomas produce chemo-attractants and growth factors that promote recruitment and proliferation of microglia/macrophages [99, 100]. In human glioblastoma up to 30% of cells can be tumor associated macrophages [101]. We characterized the microglial distribution in different anatomic locations of the 9L tumor model, which suggested that the concentration of TAM in this tumor model is similar to that observed in human glioblastoma. The microglia population per mm2 was 9-fold higher within the tumor as compared to the contralateral hemisphere and 2.5-fold higher in healthy brain tissue of the ipsilateral hemisphere as compared to the contralateral hemisphere (Figure 2.4A).

TAM are reprogrammed in the tumor microenvironment leading to an alternate immunosuppressive M2 phenotype [99]. However, a number of studies have suggested sustained phagocytic activity of TAM in glioma. The phagocytic activity of TAM has been suggested to play a key role in nanoparticle uptake [93, 94]. When microglia/macrophages change from a resting to an activated form, their morphology is modified from ramified to amoeboid indicative of their increased phagocytic activity [102]. In order to assess the morphology of TAM in the 9L tumor model we characterized the surface to volume ratio of the immune cell population (Iba1+)

in different anatomical locations [31]. The surface to volume ratio (StoV ratio) is considered a 'measure' of microglial activation [98]. Our results suggest that, indeed, the microglia/macrophages within the tumor and surrounding the tumor had a significantly ($p<0.001$) lower StoV ratio in comparison to the immune cells in the contralateral hemisphere, and in a healthy brain. The mean StoV ratio for tumor associated microglia was lower than 1, indicative of their amoeboid state and phagocytic activity (Figure 2.4B).

We then quantified the localization of D-Cy5 in the Iba1+ microglia/macrophages cells. At 24 hr post systemic administration dendrimers localized in the Iba1+. In fact, TAM Iba1+ microglia/macrophages were calculated to comprise 38% of the total tumor cell population (Figure 2.5A). Co-localization indicated that approximately half of the TAM population took up dendrimers and that the total population of dendrimer-positive cells did not differ quantitatively from the population of dendrimer-positive Iba1+ microglia/macrophages. Therefore, dendrimers were taken up almost exclusively by tumor associated macrophages within the tumor tissue (Figure 2.5A), while other cells within the tumor region didn't have measurable dendrimer uptake. Representative images of cellular uptake of dendrimer in the tumor are demonstrated in Figure 2.5B and 2.5C. Interestingly, in the tumor border (indicated as 1mm from the tumor edge based on DAPI stain) the dendrimer-positive microglia/macrophages were substantially reduced, reflecting the difference in the biological processes between the tumor core and the tumor border. Dendrimer was not observed in the ipsilateral non-tumor region or in the contralateral hemisphere (Figure 2.5D-F).

## 2.4. Discussion

In this study, we investigated hydroxyl-terminated, generation-4 PAMAM dendrimers as potential drug delivery vehicles for the delivery of therapeutics to brain tumors. The systemically delivered dendrimers accumulated and were selectively retained in intracranial tumor tissue. Moreover, they rapidly and 'homogeneously' distributed throughout the entire 6 mm solid tumor and peritumoral area, followed by a gradual accumulation in TAM. This suggests that these dendrimers may enable selective therapeutic delivery to the brain tumor.

Small molecule therapeutics may pass the impaired BBTB, but are rapidly cleared from the tumor tissue and also distribute in other organs, resulting in limited effect on the tumor cells and side effects [103], [104, 105]. Various nanoparticle systems have demonstrated relatively selective and sustained accumulation in extracranial tumors and allowed for controlled release of chemotherapeutics [75], [77, 106, 107]. However, the size limitation of the BBTB capillary fenestrations and the hindered nanoparticle motion in the heterogeneous brain tumor parenchyma does not allow for high accumulation and homogeneous distribution in brain tumors [79], [17, 108]. We show that dendrimers accumulate selectively and rapidly in an intracranial tumor and are retained in the tumor for at least 48 hr. Of note, at 4 hr post injection, dendrimer accumulation is approximately 10 fold higher in the tumor region compare with the small molecule drug doxorubicin [109]. Also, for dendrimers, the AUC(0-24h) in the tumor is 8.5 fold higher than that in the contralateral hemisphere, demonstrating improved 'intrinsic' targeting in comparison to other non-targeted nanoparticle systems and is comparable to actively targeted magnetic nanoparticles [110]. Moreover, high concentrations of dendrimer were observed in the peritumoral area. The high frequency of glioblastoma recurrence is attributed to high tumor infiltration as well as individual cells surviving the initial aggressive treatment. Therefore,

achieving high retention in the peritumoral area is important in the design of an effective therapeutic vehicle [111].

Recent studies have maintained that efficient distribution of nanoparticles throughout the solid tumor tissue is nearly mandatory for efficacy [112], [113, 114, 115]. The highly heterogeneous vasculature of glioblastoma requires the particles to escape the perivascular spaces and move a distance of at least 80 nm in order to cover the intervascular spaces [112, 116]. Perrault et al. have demonstrated that in a subcutaneous tumor model, PEGylated gold nanoparticles larger than 20 nm get entrapped in the perivascular spaces [113]. We demonstrate that after dendrimers pass through the BBTB, they rapidly distribute through the ECM within 15 min and cover the entire tumor. This observation can most likely be attributed to the small size and near neutral surface charge of the dendrimers that allow them to escape the perivascular spaces and penetrate the tumor tissue.

Our lab has previously reported that non-targeted dendrimers localized in activated microglia in the periventricular area of rabbit neonates with neuroinflammation following intravenous administration [86]. This selective cellular uptake allowed for therapeutic effect, with significant motor function improvement, following delivery of dendrimer-N-acetylcysteine conjugates [86]. Of note, this was achieved in spite of only 0.06% of injected dose accumulating in the brain, thus, underlining the importance of cell-specific targeting, rather than overall accumulation, for improved therapeutic outcome. In the present study we found that 24 hr after administration, dendrimers almost completely localized in TAM and that approximately 50% of the TAM population had taken up dendrimers. The dendrimers were not seen in ‘non-activated’/quiescent microglia/macrophages. The high concentration of phagocytic cells in this tumor in combination with the remarkably high accumulation of dendrimers in TAM may

contribute to their retention in glioblastoma. The mechanism of nanoparticle accumulation in TAM has previously been investigated using cyclodextrin-based particles and carbon nanotubes. It is possible that both invading macrophage/monocytes take up nanoparticles in the circulation but also that TAM within glioma take up nanoparticles after they distribute in the tumor parenchyma [93]. However, the rapid distribution of dendrimer in the tumor, the rapid elimination from the circulation and the low accumulation in the reticuloendothelial system, suggest that the dendrimers localize more through the latter mechanism. To clarify, the TAM uptake shown by dendrimers is specific to activated cells in the tumor, different from the typical systemic macrophage uptake/clearance of larger nanoparticles. Neuroinflammation and TAM have important growth promoting and pro-invasive effects in brain tumors. TAM is subjected to reprogramming in the tumor microenvironment, leading to an alternate immunosuppressive tumorigenic M2 phenotype [99]. Topically administered immunomodulatory which block the M2-related phenotype of TAM are being investigated for the treatment of glioblastoma [87, 88]. Dendrimer-specific accumulation in TAM with low retention in the reticuloendothelial system and rapid clearance from the circulation, suggest that these systematically delivered dendrimers are promising candidates for the delivery of anti-glioma therapies targeting TAM.

## 2.5. Conclusion

Systemically delivered hydroxyl, generation-4 PAMAM dendrimers rapidly accumulate (~ fifteen minutes) and are selectively retained in an *in vivo* intracranial brain tumor model. The dendrimers homogeneously distribute throughout the entire 6 mm solid tumor and peritumoral area and gradually accumulate in TAM. This homogeneous distribution is retained for at least 48 hr indicating that the dendrimers used in this study may be effective vehicles for delivery of

chemotherapeutics. Also, the intrinsic targeting of neuroinflammatory cells which play a critical role in the aggressive nature of glioblastoma may allow for enhanced delivery of immunomodulatory molecules to TAM. This study of the pharmacokinetics and biodistribution of dendrimers in an intracranial brain tumor model provides insights for the design and engineering of systemically-delivered dendrimer-drug conjugates for improved efficacy, and reduced side effects for brain tumors.

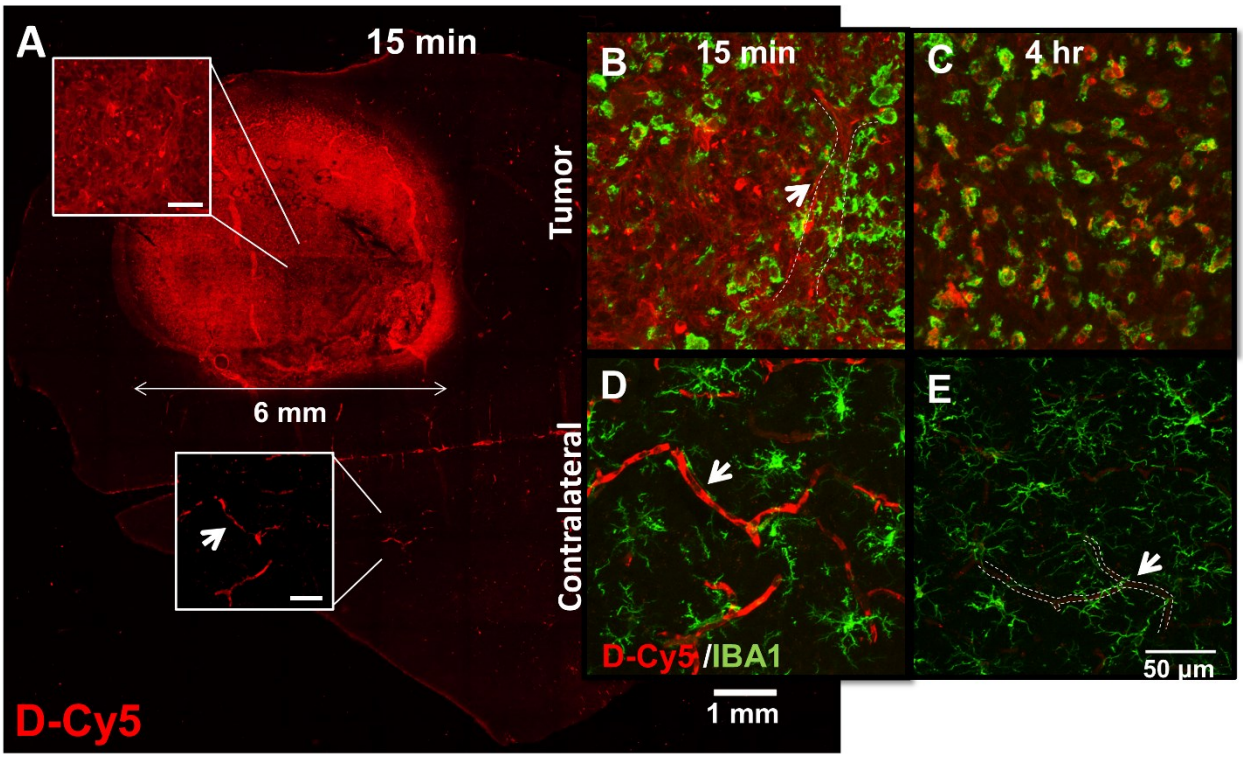


**Figure 2.51 Confocal microscopy images of tumor-inoculated rodent brain following systemic administration of D-Cy5.**

(A) Low magnification image of tumor inoculated brain, 15 min following systemic administration of D-Cy5. Scale bar: 1 mm. Inset images indicate the homogeneous distribution of D-Cy5 in the tumor and the restriction of dendrimer in the blood vessel lumen of the contralateral hemisphere. Scale bar: 50 µm (B) High magnification images of the tumor and contralateral hemisphere 15 min and 4 hr post I.V. administration. Red: D-Cy5; Green: Iba1+ microglia/macrophages. Scale bar: 50 µm. Arrow and dashed line delineate blood vessels.

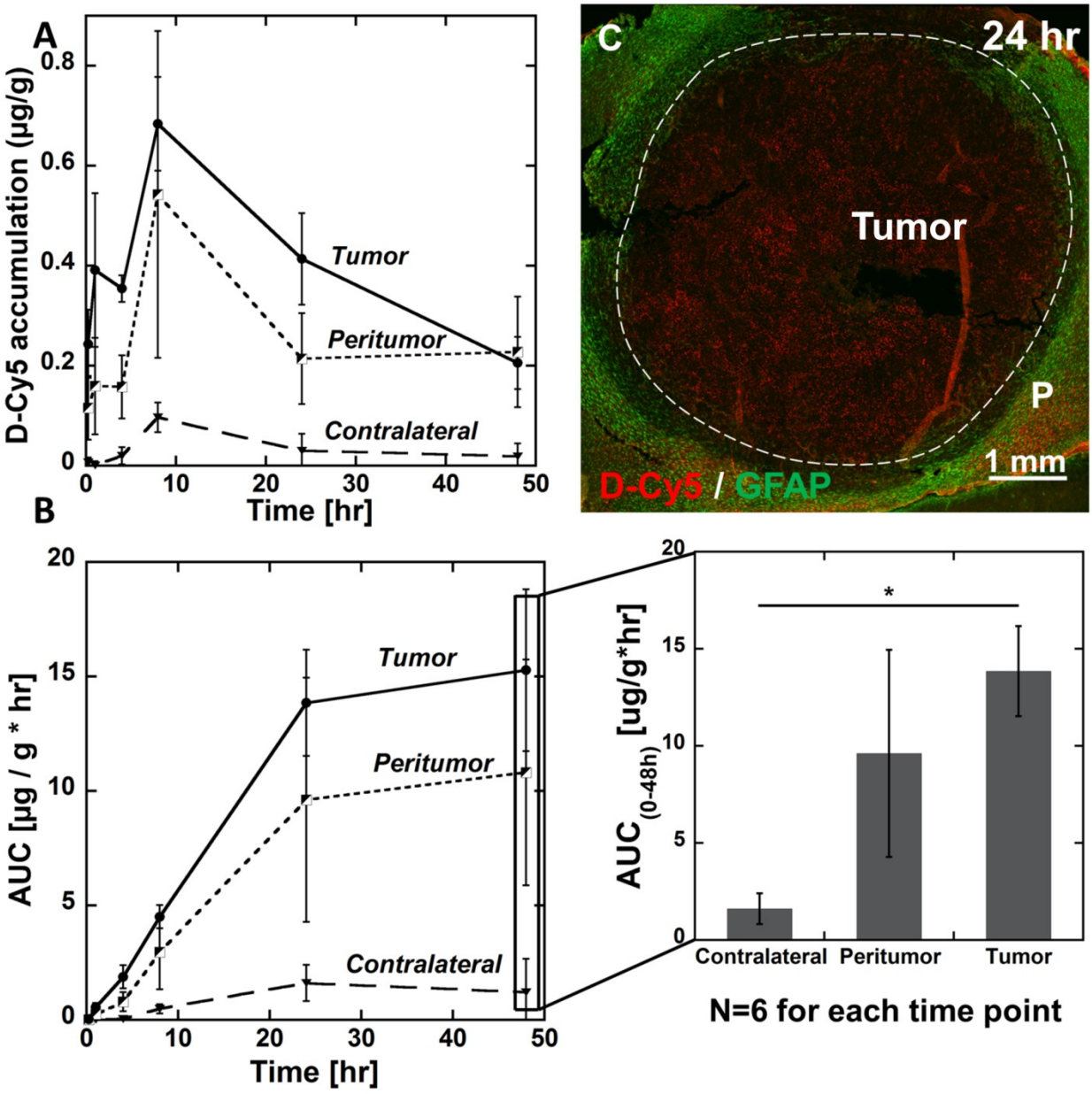


**Figure 2.52 D-Cy5 pharmacokinetics in the brain (tumor, peritumor and contralateral hemisphere) of a rodent 9L gliosarcoma model.**

(A) D-Cy5 concentration in brain areas 15 min, 1 hr, 4 hr, 8 hr, 24 hr and 48hr following systemic administration. The accumulation is expressed as µg of D-Cy5 per g of tissue. Data represents mean ± standard error of the mean (SEM) (B) Exposure of respective brain areas to D-Cy5 following systemic administration as expressed by the AUC of D-Cy5 concentration at

different time points. The AUC at 48 hr demonstrates the statistically significant difference in dendrimer accumulation between the tumor and the contralateral hemisphere ($p<0.05$). (C) Fluorescence-microscopy image demonstrating vascular density and D-Cy5 accumulation in brain tumor 24 hr post I.V. administration. Red: D-Cy5; Green: GFAP (physiologic astrocytes). T: Tumor P: Peritumoral area C: Contralateral area; Scale bar: 1 mm.

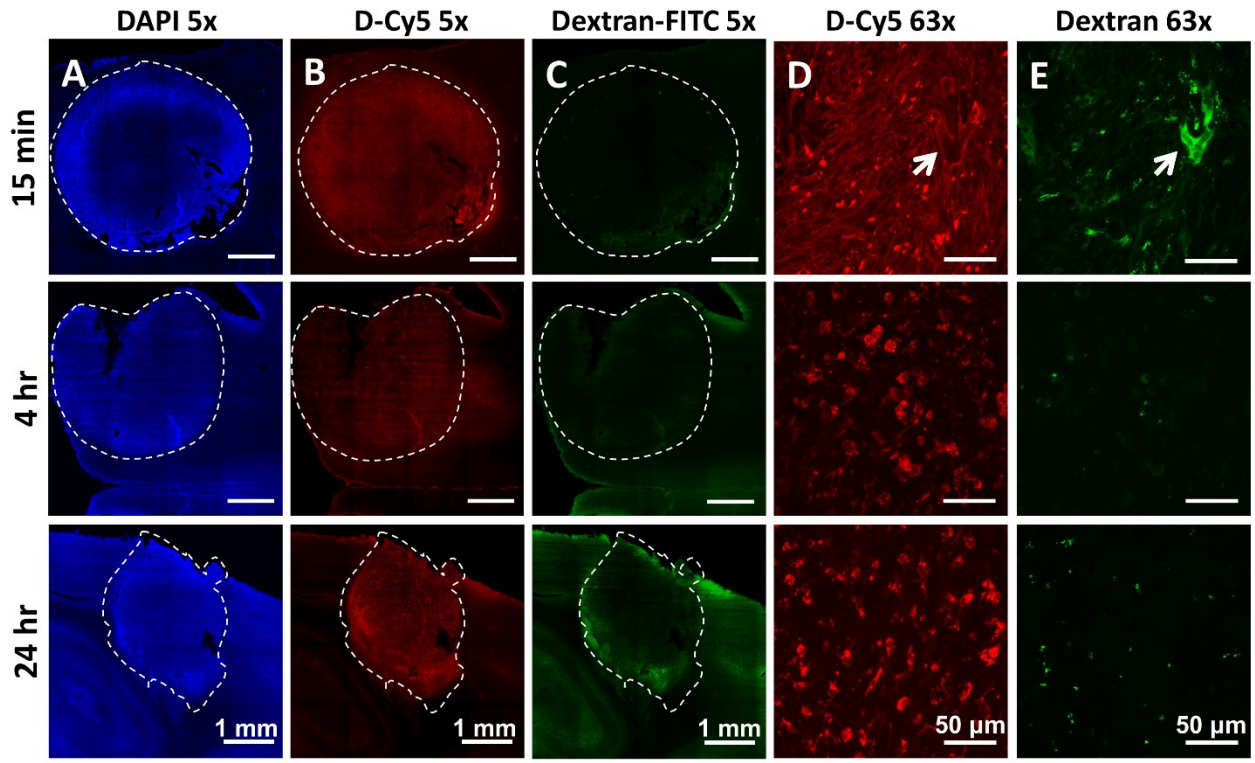


**Figure 2.53. Confocal microscopy imaging of 9L gliosarcoma rodent brains following systemic co-administration of D-Cy5 and 70 kDa Dextran-FITC.**

(A-C) Low magnification and (D, E) high magnification images of D-Cy5 and Dextran-FITC distribution in the tumor area. Blue: DAPI staining of nuclei indicative of the tumor region; Red: D-Cy5; Green: Dextran-FITC. Scale bar: 1 mm (Column A-C) and 50 µm (Column D and E). White arrow indicates a blood vessel based on DAPI staining (not shown).

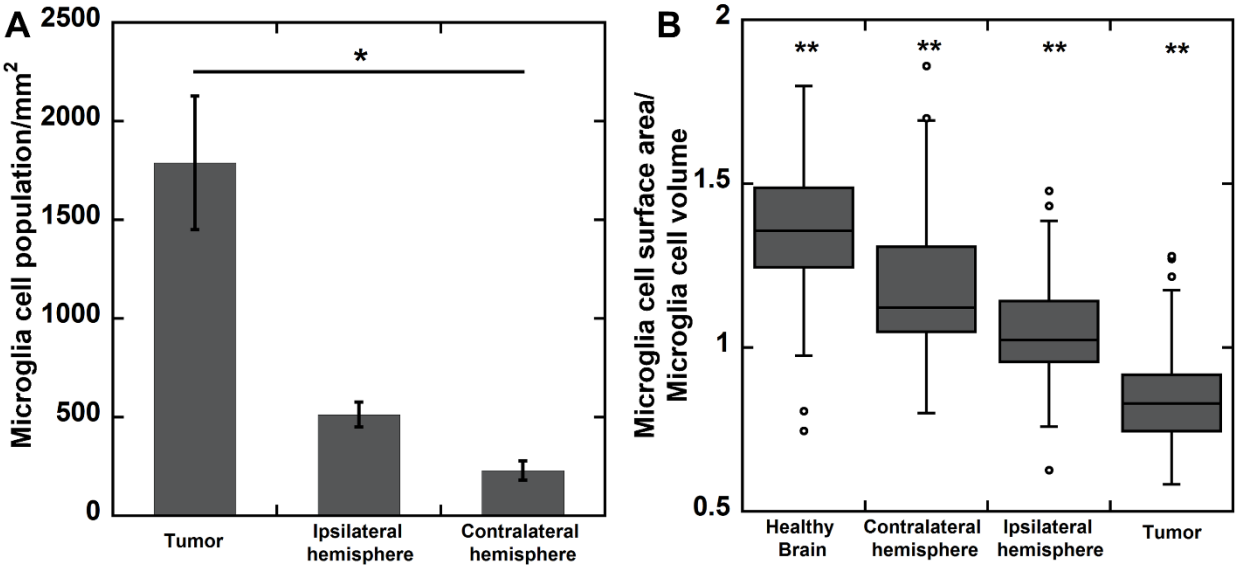


**Figure 2.54. Characterization of microglia cells (population and activation status) in a 9L gliosarcoma inoculated rodent brain using Imaris software.**

(A) Image-based cell count of the Iba1+ microglia/macrophages population per mm2 area in the tumor, ipsilateral hemisphere and contralateral hemisphere; *p<0.05 (B) Image-based measurement of microglia cell surface to volume ratio as an indication of activation status and phagocytic activity of microglia/macrophages in healthy brain, contralateral hemisphere and ipsilateral hemisphere of a tumor inoculated brain and tumor tissue. **p<0.01; Statistical analysis is based on 3-5 different slices.

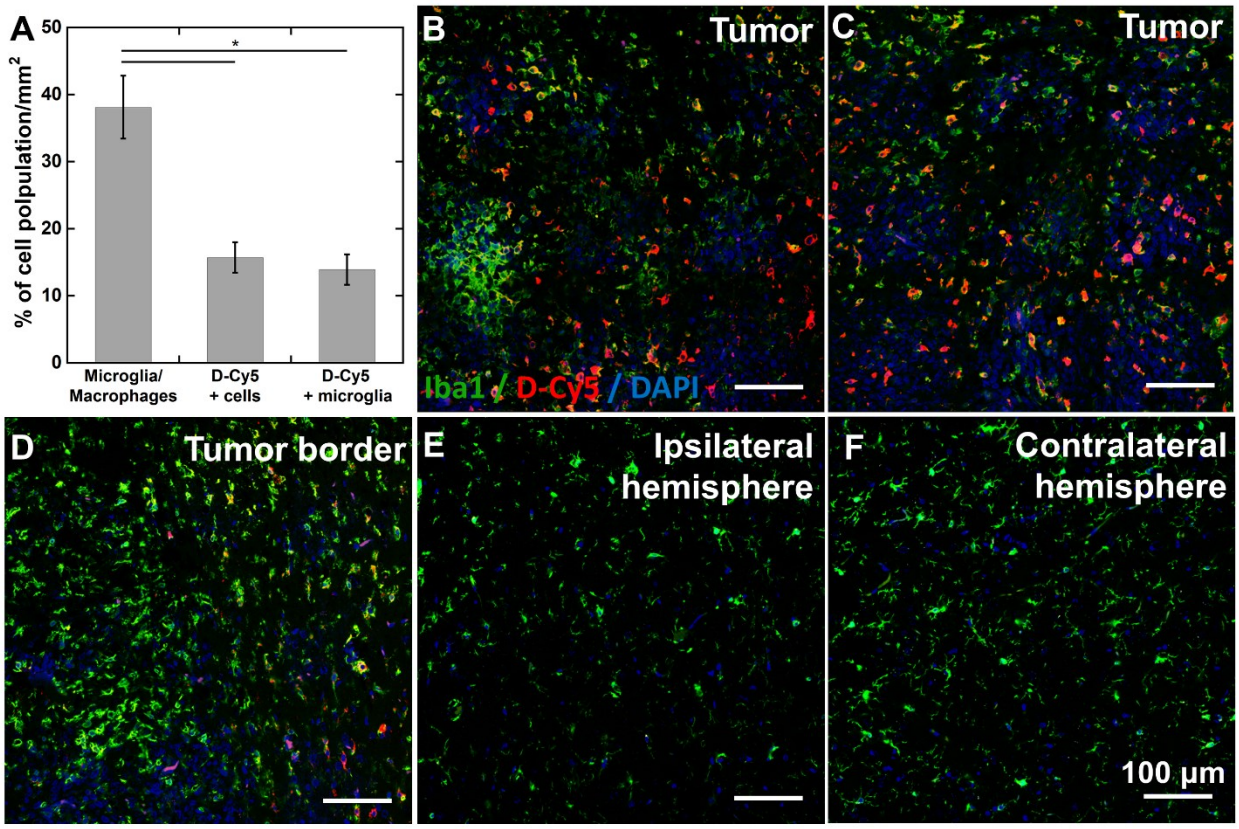


**Figure 2.55. D-Cy5 cellular uptake analysis 24 hr following systemic administration.**

(A) Image based measurement of Iba-1+ cells, D-Cy5 co-localization with Iba1+ TAM, and D-Cy5 co-localization with DAPI+ cells. Results are expressed as percent of the total DAPI+ cell population. *$p<0.05$; There is no statistical significance between microglia uptake and cell uptake. (B-F) High magnification (40X) fluorescence confocal imaging of different anatomic locations of a 9L gliosarcoma inoculated brain. Green: Iba1+ microglia/macrophages, Red: D-Cy5, Blue: DAPI. Scale bar: 100 µm. Statistical analysis is based on 3-5 different slices.

# 3. DENDRIMER TARGET NEUROINFLAMMATION IN FETUS UPON INTRA-AMNIOTIC ADMINISTRATION

## 3.1. Introduction

Cerebral Palsy (CP) is a chronic childhood disorder caused by injury to the developing brain that occurs either in utero, during birth or soon after birth [117]. As a result, patients usually develop permanent motor, sensory and cognitive deficits [118]. According to the United States Centers for Disease Control and Prevention (CDC), the prevalence of CP is 1.5-4 per 1,000 live births [119]. In infants born prematurely, 5-10% develop motor disability, and 40-50% develop some form of cognitive and/or behavioral disability [120]. Although CP has multiple etiologies [121], a major pathological substrate is neuroinflammation mediated by activated microglia/astrocytes, leading to periventricular leukomalacia (PVL) [122]. Pro-inflammatory activation of microglial cells can result in persistent neuroinflammation, including release of free radicals, excitotoxic metabolites, and pro-inflammatory cytokines, leading to diffuse white and grey matter injury at foci where conventional therapeutics cannot reach and achieve cellular-targeting [123]. Therefore, an effective therapeutic agent should cross the blood-brain barrier (BBB), achieve rapid transport to reach the cells associated with inflammation and injury, attenuate both inflammatory and oxidative stress, and have minimal systemic side effects and should avoid uptake into healthy regions of the brain and healthy cells [124]. Our previous studies have shown that neutral, hydroxyl-terminated polyamidoamine (PAMAM) dendrimers, delivered in the postnatal period either though intravenous (i.v.) or subarachnoid administration, can localize in activated microglial cells in animals with neuorinflammation [125, 126]. When N-acetyl-L-cysteine (NAC), an antioxidant and anti-inflammatory agent, is covalently conjugated to the dendrimer, these dendrimer-NAC (D-NAC) conjugates can efficiently

attenuate neuroinflammation and improve motor function in a rabbit model of CP [126]. This work suggests that there is a window of opportunity in the perinatal period when treatment of neuroinflammation may lead to an improvement in motor function and survival in CP. Treatment of the mother in the prenatal period is one such opportunity.

Advances in early diagnosis of prenatal inflammation and chorioamnionitis that are risk factors for CP have opened the possibility for prenatal therapies [127]. However, lack of studies on drug efficacies, kinetics of prenatal therapy and relative distribution between the maternal and fetal compartments have limited the use of fetal therapies in the perinatal period. To achieve prenatal delivery of therapeutics to the fetus, intra-amniotic delivery is one possible administration route. Although delivery thorough amniotic fluid is a novel delivery strategy, it amounts to oral delivery, since the fetus swallows the dendrimers along with amniotic fluid.

Recent *in vivo* studies on oral delivery have shown dendrimers as promising intestinal penetration enhancers, drug solubilizers and drug carriers [128]. We also demonstrated in a mouse model of intrauterine inflammation and preterm birth that intra-amniotically administrated D-OH can be orally taken up by the fetus within a few hours post administration [129]. Carboxyl-terminated anionic generation 3.5 PAMAM dendrimers (D-COOH) have been reported to achieve better oral bioavailability than their hydroxyl terminated neutral counterparts (D-OH) [128, 130, 131], while maintaining a similar biosafety profile to D-OH [132]. In present study, both D-OH and D-COOH biodistribution and uptake were investigated via intra-amniotic administration in the prenatal period to provide opportunity for dendrimers to be ‘orally’ taken up by fetus, in a clinically-relevant rabbit model of CP. The fetal uptake, cellular localization in the brain, and the bi-directional transport across the maternal-fetal compartment were investigated.

## 3.2. Materials and Methods

### *3.2.1. Materials and reagents*

D-OH and D-COOH (Dendritech). Methanol (HPLC grade, Sigma-Aldrich), Cy5-NHS ester (GE Healthcare Life Science), stainless steel beads (Fisher Scientific), Fmoc-1,5-diaminopentane hydrobromide (Sigma), TSK gel ODS-80 Ts (250 4.6mm, i.d., 5µm) column (Tosoh Bioscience LLC, Japan), 4',6-diamidino-2-phenylindole (Molecular Probes), Goat anti-Iba1 (Abcam), Alexa Fluor® 594 Goat Anti-Rabbit IgG (Molecular Probes), Anti-CD31 (Abcam), Anti-Cytokeratin 13 (Abcam) were purchased.

### *3.2.2. Animals*

The experimental procedure is described in Figure 3.1. Laparotomy was conducted on pregnant rabbits at gestational day 28 (G28, term pregnancy 31 days) under general anesthesia (2-3% isoflurane by mask). Saline containing 6000EU of E. coli endotoxin (Escherichia coli serotype O127:B8, Sigma Aldrich) (Endotoxin) or equivalent volume of saline alone (Control) was distributed equally (100µL per injection site) and injected along the length of the uterus as previously described by us. Immediately after this, 50µL of Cy5 labeled D-OH or Cy5 labeled D-COOH (concentration of 12mg/mL) were injected intra-amniotically into each gestational sac along the right uterine horn using a 30G needle (IA-Dendrimer). This would result in an individual fetal dose of ~20mg/kg assuming a fetal weight of about 30g. This dose was based on our previous study of intravenous injection of D-NAC in newborn rabbits, where dendrimer was administrated at dose ranging from 5.5mg/kg to 55mg/kg [15]. taking into account that intra-amniotic injection is somewhat similar to oral administration, since the fetus swallows the amniotic fluid. The gestational sacs along the left uterine horn were injected with saline alone

and served as internal controls (IA-Saline). As a result, 4 different groups were created in the study (as demonstrated in Figure 3.1), namely (1) fetuses with endotoxin treatment and intra-amniotic (IA) dendrimer injection (Endotoxin, IA-Dendrimer); (2) fetuses with endotoxin treatment and intra-amniotic saline injection (Endotoxin, IA-Saline); (3) fetuses with control saline (Sham) treatment and intra-amniotic dendrimer injection (Sham, IA-Dendrimer); (4) fetuses with control saline treatment and with intra-amniotic saline exposure (Sham, IA-Saline). Dendrimer used in these 4 groups were either D-OH-Cy5 or D-COOH-Cy5. Routine closure was performed and the dams were recovered in individual cages. Cy5 labeled dendrimer solution diffused quickly in the amniotic fluid within 1 to 3sec. No indications of leakage were seen during or post injection. Procedures for animal sacrifice were previously described [15].

*3.2.3. Dendrimer extraction procedures*

The method for extraction and quantification of Cy5 labeled dendrimers is described elsewhere [16]. Briefly, all tissue samples were defrosted before further processing. Liquid samples (serum, urine, amniotic fluid) were diluted 10-fold in PBS and filtered through 0.2μm membrane before the measurements. For all tissue samples, 100mg of tissue were carefully dissected from each organ. For the intestinal tract, only the small intestine was dissected for quantification; for maternal organs, at least three samples per organ were dissected from each region to have an accurate representation of dendrimer accumulation. To obtain blood free and clear supernatants, samples were centrifuged for 15min at 15000rpm and 4oC using 5424R, Eppendorf centrifuge. Supernatants were then analyzed by fluorescence spectroscopy.

### *3.2.4. Fluorescence spectroscopy*

Fluorescence spectra of Cy5 labeled dendrimer extracts were recorded using a Shimadzu RF-5301 Spectrofluorometer. Calibration curves for Cy5-labeled dendrimers were constructed by recording the fluorescence intensity of Cy5 labeled dendrimers at emission wavelength of 662nm or 665nm, under the maximum of excitation at 645nm. To maximize the intensity of emission, different sets of excitation and emission slit widths were applied for different dendrimer concentrations.

Spectra for each extract were recorded using different sets of excitation and emission slit widths, the one with the highest emission intensity was selected for quantification of dendrimer, applying a calibration curve obtained at the same conditions. To compensate for autofluorescence originating from the tissue matrix, intensities registered for control samples obtained from each specimen of non-treated animals were subtracted from the values observed for samples acquired from animals injected with Cy5 labeled dendrimers. All calculations were performed using Excel. Statistical analysis was performed using a student's T test.

### *3.2.5. Immunohistochemistry study of dendrimer accumulation and distribution*

Fetal brains, fetal small intestine and placenta were fixed with 4% PFA once they were harvested, followed by processing with gradient sucrose solutions (10%, 20%, 30%). Processed tissues were then cryosectioned with a Leica CM1850 cryostat (Leica Biosystems, USA). For all samples, DAPI was used to stain the nucleus. For fetal brain samples, goat anti- ionized calcium-binding adapter molecule 1 (Anti-Iba1, primary antibody) and donkey anti goat 594 (secondary antibody) was then used to stain the microglia/macrophages. Anti-CD31 antibody (primary antibody) followed with Donkey anti-mouse 488 (secondary antibody) was used to stain the blood vessels. For placenta samples, the placental villous structure was identified based on the

staining of syncytiotrophoblast layer using anti-cytokeratin13 antibody (primary antibody) and donkey anti-mouse 488 (secondary antibody, Abcam). Images were obtained using Zeiss LSM 710 Meta Confocal Microscope (Carl Zeiss, USA).

## 3.3. Results

### *3.3.1. Preparation and characterization of Cy5 labeled D-OH and D-COOH dendrimers*

In brief, to prepare Cy5-labeled D-OH and D-COOH, both dendrimers were partially functionalized with amines using suitable linker and then reacted with Cy5-NHS ester to form D-OH-Cy5 and D-COOH-Cy5. To prepare D-OH-Cy5, 6-(Fmoc-amino)caproic acid was conjugated to the D-OH using PyBOP as coupling reagent with DIEA in DMF. Fmoc groups was then deprotected using piperidine/DMF mixture (2:8) to get ~3-4 free primary amine groups on the surface of the dendrimer, followed with labeling using Cy5-NHS in bicarbonate buffer (pH=9.1): DMSO (1:1) to get D-OH-Cy5 conjugate. The final conjugates were purified by dialyzing against 1 kDa membrane and size exclusion chromatograph (SEC) using Sephadex G-25 gel. The final products were characterized by proton NMR, HPLC/GPC, and fluorescence spectroscopy D-OH-Cy5 conjugate was previously demonstrated to be structurally and fluorescently stable in human plasma under 37°C. To prepare D-COOH-Cy5, salt free form of carboxylate dendrimer was reacted with N-Fmoc-1,5-diaminopentane hydrobromide using PyBOP as coupling reagent to yield the Fmoc-functionalized intermediate. The Fmoc deprotection, Cy5-labeling of amine functionalized D-COOH, and the purification of final product D-COOH-Cy5 were carried out by following similar procedures as described in D-OH-Cy5 preparation. The final conjugates were characterized by HPLC and fluorescence spectroscopy.

To confirm the preservation of neutral and negative surface charge of D-OH and D-COOH after partially functionalizing with amines, the size and ζ-potential of D-OH, amine functionalized D-OH, D-COOH, and amine functionalized D-COOH were measured using dynamic light scattering (DLS) and zeta-seizer, as shown in Table 1. After partially functionalizing with surface amines, the physical properties of D-OH and D-COOH were maintained, with a slightly increase in size (D-OH: from 4.4 ± 0.2 nm to 4.7 ± 0.3 nm; D-COOH: from 3.2 ± 0.4 nm to 3.8 ± 0.2 nm) and surface charge (D-OH: from 4.5 ± 0.6 mV to 6.6 ± 0.2 mV; D-COOH from -28.6 ± 0.7 to -21.8 ± 0.6).

*3.3.2. D-OH and D-COOH partitioned into fetal systemic circulation and were transported into maternal side.*

When compared to intravenous administration, intra-amniotic administration of dendrimers provides an opportunity for dendrimers to be exposed to the fetal gastrointestinal track (GI track) during the circulation of amniotic fluid within the amniotic sac. Hence, amniotic delivery would primarily represent 'oral delivery' of dendrimers. Based on this, we began assessing whether D-OH and D-COOH can pass through the intestinal wall and partition into the fetal systemic circulation. As expected, we observed that both D-OH and D-COOH transported across the epithelial layer of the intestinal villi and were detected along the inner wall of the intestinal villi at 24hours (G29) post administration (Figure 3.2), indicating the partition of both dendrimers into the fetal systemic circulation. Surprisingly, the transport of dendrimers from amniotic fluid to fetal systemic circulation was rapid. In the biodistribution study performed at G29, the presence of dendrimers in major fetal and maternal organs was evaluated and expressed as % injected dose per gram of tissue or per milliliter of liquid (%ID/g or mL). Most of the dendrimer injected had already transported out of the amniotic fluid, leaving only a limited amount of

dendrimer (for D-OH, less than 3%/mL, for D-COOH, less than 0.5%/mL) present in the amniotic fluid (Figure 3.3, top row). For dendrimer transported out of the amniotic fluid, it was either retained in fetal/maternal tissue or cleared out from maternal systemic circulation. We determined that ~20-30% D-OH and ~10% D-COOH were retained in the fetal side (Table 2), with most of the dendrimers accumulating in the fetal GI tract, lung and placenta (Figure 3.3, bottom row). The high accumulation in the placenta was correlated with the finding that significant amount of dendrimer was transported out from the fetal side and accumulated either in the maternal side (D-OH, 50-60%, Table 2) or excreted out from the urine (D-COOH, 70-80%, Table 2). The redistribution of majority of dendrimer from amniotic fluid to both maternal and fetal compartments observed at G29, and excretion of the dendrimer in the maternal urine indicates that dendrimer transport occurs relatively fast.

*3.3.3. D-OH crossed BBB of endotoxin treated fetus at G29, and showed co-localization in microglia, while D-COOH was restricted to the blood vessels in the brain.*

Since amniotic-administrated D-OH and D-COOH can both be orally absorbed by the fetus and enter into fetal systemic circulation, we seek to understand whether these dendrimers can reach the fetal brain parenchyma and target inflammatory cells. To identify whether these dendrimers can accumulate in the brain of an endotoxin-treated, injured fetus, we quantified the amount of brain accumulation of D-OH and D-COOH at G29 (24hours post dendrimer administration). Both dendrimers had similar extent of total brain accumulation in the endotoxin treated fetus at G29, with a slightly higher uptake for D-OH (0.28μg/g of dry tissue) compared to D-COOH (0.22μg/g of dry tissue) (Figure 3.4A). However, further investigations using confocal microscopy revealed that the brain accumulation in the endotoxin treated fetus showed two distinctive distribution patterns between the two dendrimer platforms, attributable to the different

surface charges of D-OH and D-COOH. As shown in Figure 3.4B, at G29 (24hours after dendrimer administration), has less presence in the blood vessels, the relatively high background in the brain parenchyma around blood vessels and less co-localization with anti-CD31 (endothelial stain) indicated D-OH has already diffused across the BBB, and distributed in the brain parenchyma around the periventricular region (PVR). On the contrary, D-COOH was only observed to be associated with blood vessels, with limited signal in the brain parenchyma. These findings suggest D-OH could cross the impaired BBB in the endotoxin treated fetus and distribute within the brain parenchyma to reach target disease-associated cells.

*3.3.4. D-OH and D-COOH did not accumulate in the brain parenchyma of sham fetus.*

There are several studies investigating the integrity of the BBB in the developing rodent brain in healthy rabbits, the fetal BBB is thought to be intact prior to birth [133, 134], and is more representative of the human BBB. We next sought to evaluate the distribution of both dendrimers in a sham fetus ('healthy' surgical control) to ensure that the BBB at this age is not leaky to dendrimer in 'healthy' fetuses. Given that sham fetuses were not exposed to endotoxin during their gestation period, their BBB should be intact relative to an endotoxin-treated fetus. As a result, although there was D-OH accumulation in the brain of sham fetus (Figure 3.5A), D-OH was mainly associated with the blood vessels, and was not present in the brain parenchyma (Figure 3.5B). In contrast, D-COOH were neither associated with blood vessels nor presented in the brain parenchyma.

*3.3.5. D-OH selectively localized in 'activated' microglia in different stages of activation.*

We have previously shown that D-OH accumulates in microglia in PND1 kits with CP, following systemic administration on PND1 [125, 126]. To determine if similar microglial uptake was present at PND1 with intra-amniotic administration of D-OH, we investigated the

uptake and presence of D-OH in microglia on PND1 following D-OH amniotic administration on G28. We found PND1 (G31) kits with CP had pronounced microglial uptake of D-OH. In this rabbit model of CP, a progressive increase in activation of microglial cells has been demonstrated after the treatment with endotoxin [135]. Interestingly, the D-OH microglial uptake also showed an increasing trend with time from G29 to PND1 (Figure 3.6). At G29, traces of D-OH signal were observed within microglial cells around the lateral ventricle, while at G31/PND1, the D-OH signal in microglial cells in the same region intensified significantly. Our results suggest that the observed increasing D-OH uptake is strongly associated with the progressive activation and proliferation of microglial cells in this model. Moreover, a longer exposure of the fetus to the dendrimer because of recirculation may increase the amount of dendrimer available for uptake by the microglial cells. This data also demonstrates that D-OH administered intra-amniotically pre-term remains in microglial cells in the postnatal period.

### 3.4. Discussion

We have previously reported significant motor function improvement upon systemic dendrimer-NAC therapy, administered after birth in the rabbit model of CP [126]. However, since inflammation in the CNS often develops in utero, the possibility of prenatal therapy could potentially prevent the injury at a much earlier stage. In this study, we demonstrate that dendrimers, when delivered by intra-amniotic administration in the prenatal period, can be absorbed by the fetus, cross the BBB in the fetal brain, and target microglial cells in the presence of inflammation. Our studies suggest that (1) dendrimers in the intra-amniotic fluid could be absorbed by the fetus and transported across the placental barrier into maternal systemic circulation; (2) the surface functionality of dendrimers influences its distribution and

accumulation in the brain, and the more neutral D-OH was more effective in localizing in activated microglia in the brain when compared to the negatively charged D-COOH dendrimers.

D-OH, which achieved significant efficacy in our previous postnatal therapy study [126], and D-COOH, which have better oral bioavailability [136] were selected for this biodistribution study. The surface functionality of dendrimer had an effect on brain accumulation and distribution. PAMAM dendrimers with amine surface functionality were not used in this study, due to the previously known inability to diffuse in brain tissue [67, 137] and the potential higher cellular and systemic toxicity [64, 66, 130] compared to those with neutral (OH) and negative (COOH) surface functionalities. In our study, D-OH was more efficient in crossing the BBB and localizing in microglial cells following intra-amniotic administration in the endotoxin fetuses. This occurs due to a combination of the physiochemical properties of the dendrimer and the host characteristics including the presence of neuroinflammation. The damage of the BBB provided a chance for dendrimers to extravasate, while the small size (~4.3nm) and neutral surface charge enabled D-OH to diffuse within the excellular matrix of the brain parenchyma and reach the microglial cells. However, D-COOH was temporarily restricted to the blood vessels at the G29, presumably due to the negative charge on the BBB surface [138]. The differences of brain accumulation and distribution of D-OH and D-COOH stem from the different zeta-potential of these two types of dendrimers, which provided a guideline for the design of intra-amniotic delivered dendrimer therapies. A more neutral zeta-potential is recommended when design a dendrimer-based conjugates for targeting inflammatory CNS disorders. The amount of dendrimers brain accumulation is a direct indication of therapeutic potential of dendrimer-based therapy, we therefore compared the brain (endotoxin fetus) accumulation of intra-amniotically administrated D-OH (administrated at G28) with that of systemic administrated D-OH

(administrated at PDN1) at both 24 hours post administration. We found the amount of D-OH accumulation through both administration routes are in the same order (~0.3 μg/g for prenatal intra-amniotic administration of 20 mg/kg D-OH, ~0.75 μg/g for postnatal systemic administration of 55 mg/kg D-OH). This implied that intra-amniotic route has the potential to deliver effective dose of therapeutics to the injured brain of CP kits. The D-OH uptake in the endotoxin treated fetus was also associated with the activation of microglial cells. In our previous mouse study, we did not observe significant microglial uptake of D-OH within 24 hours post injection even D-OH was able to present in the brain parenchyma, likely due to the lack of microglial activation during the period of dendrimer exposure [129]. In present study, we saw an increase dendrimer uptake with the progression of microglial activation. Specifically, microglial uptake at G29 was less than that seen at G31 (PND1), likely because the microglia activation and proliferation were ongoing and peak activation has previously been shown to be around G31 (around 72hours after endotoxin exposure) [139]. With the progression of inflammation in the fetal brain, the released cytokines (TNF-α, IL-1β, IL-6) polarize microglial cells into a pro-inflammatory phenotype [140]. This is associated with overwhelming microglial uptake at G31, which proves the positive correlation between dendrimer uptake and microglial activation in this model [135].

### 3.5. Conclusion

In this work, we have determined the mechanism for intra-amniotically administrated dendrimers to target neuroinflammation in the fetal brain. Our studies suggest both hydroxyl-terminated (D-OH) and carboxyl-terminated (D-COOH) generation-4 polyamidoamine (PAMAM) dendrimers were absorbed by fetuses. D-OH was more effective in crossing the fetal blood-brain barrier, localizing in activated microglia. This study demonstrates intra-amniotically

administered D-OH could be an effective drug delivery vehicle for targeting fetal inflammation and preventing subsequent neurologic injury associated with chorioamnionitis.

**Table 3.1. Size, ζ- Potential of dendrimers**

| Dendrimer | Size ± SEM (nm) | ζ-potential ± SEM (mV) |
|---|---|---|
| G4-OH | 4.3 ± 0.2 | +4.5 ± 0.1 |
| G4-OH-$(NH_2)_4$ | 4.7 ± 0.3 | +6.6 ± 0.2 |
| G3.5-COOH | 3.2 ± 0.4 | -28.6 ± 0.7 |
| G3.5-COOH-$(NH_2)_4$ | 3.8 ± 0.2 | -21.8 ± 0.6 |

**Table 3.2. Estimation of uptake and clearance of dendrimers at 24 hours post administration.**

| Dendrimer | Fetal uptake | Maternal uptake | Maternal Urine |
|---|---|---|---|
| | % of total injected dose | | |
| D-OH | 20-30% | 50-60% | 10-30% |
| D-COOH | 10% | 2% | 70-80% |

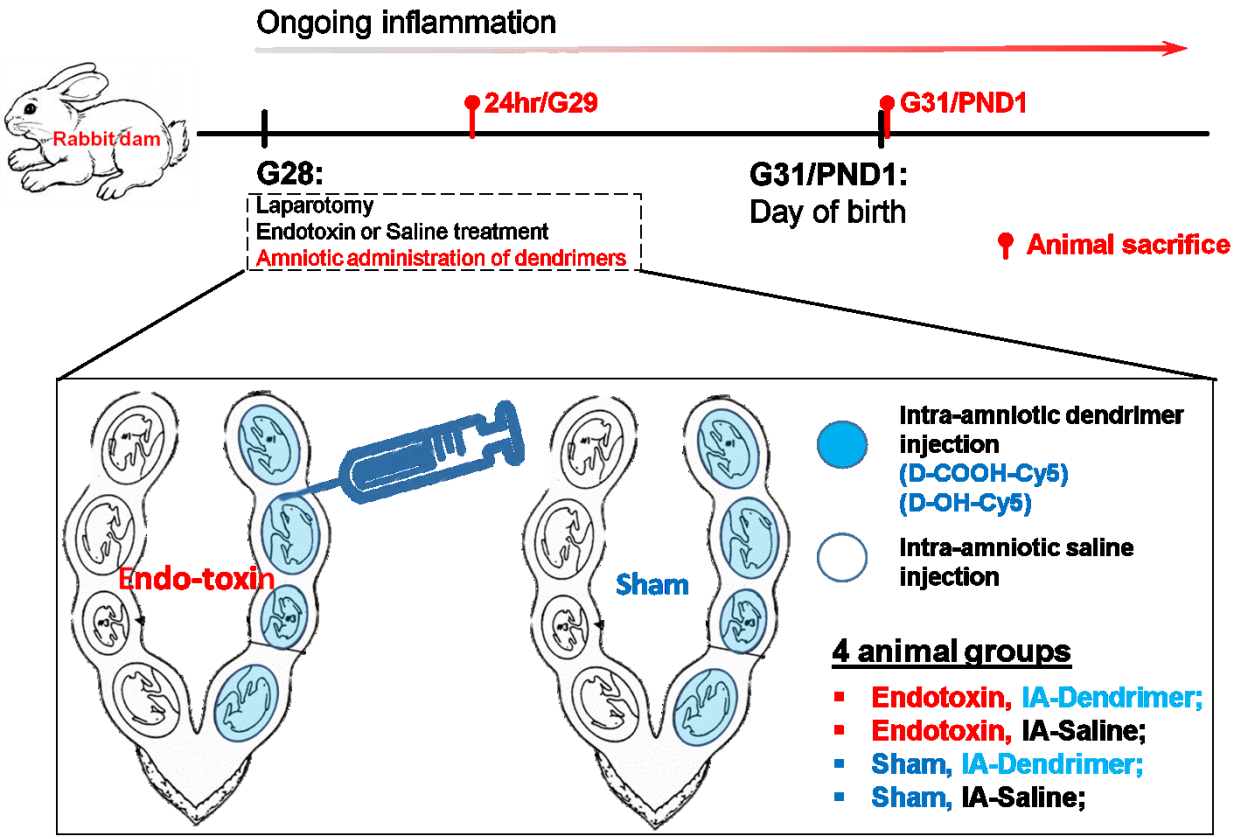


**Figure 3.51. Flow chart demonstrating surgery procedures designed in the experiment.**

Endotoxin or saline was administrated at G28 during the laparotomy, followed with intra-amniotic administration of dendrimer (Cy5-labeled D-OH or D-COOH) or saline. Animals were sacrificed at selected time points (i.e. G29 and G31/PND1 post dendrimer administration). BOX: Graphic explanation of 4 groups designed in this study.

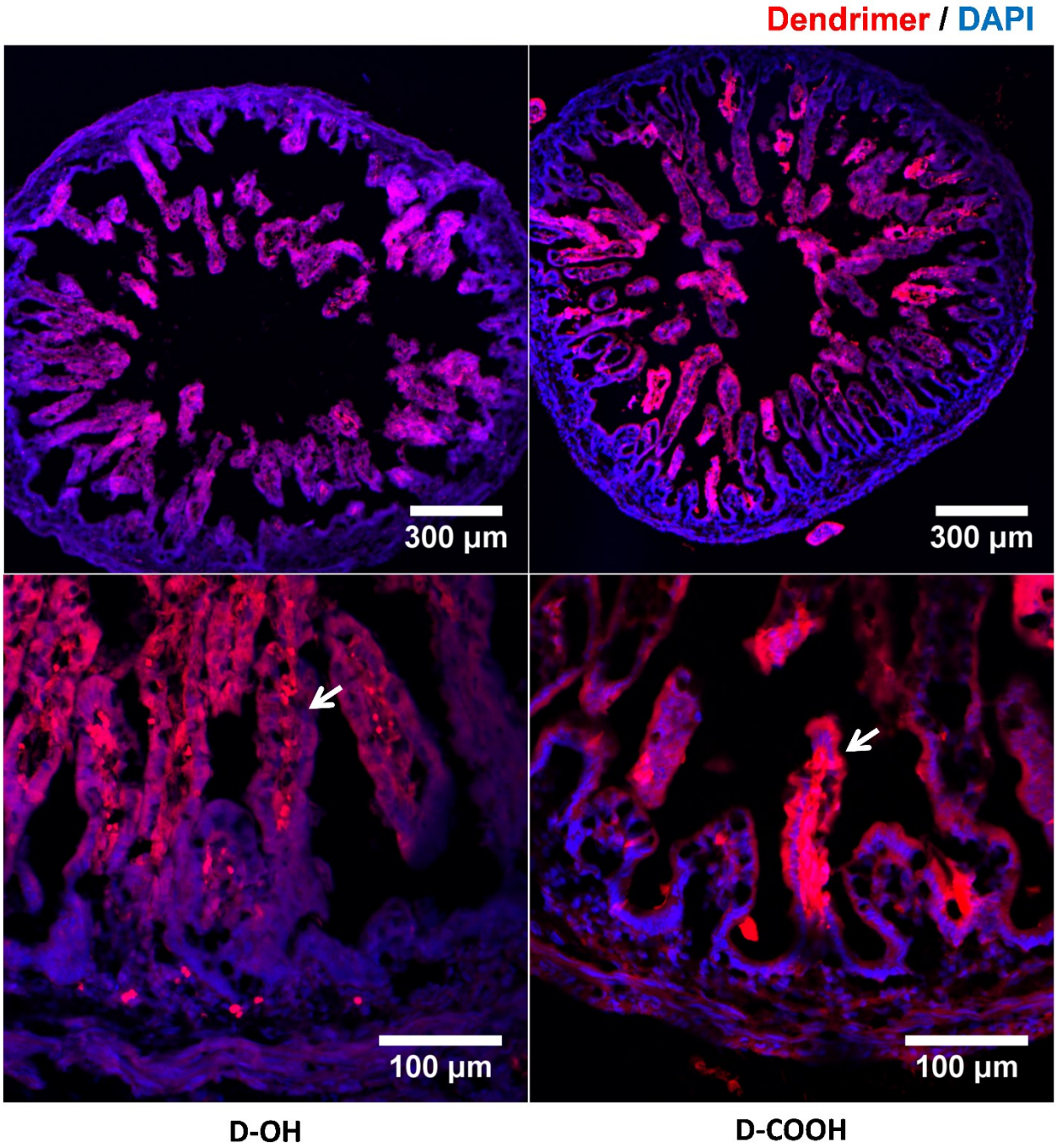


**Figure 3.52. Immunofluorescence images demonstrate D-OH and D-COOH distribute in the small intestine.**

As shown in both lower magnification (top) and higher magnification images (bottom), at 24 hours (G29) post administration, dendrimers (D-OH and D-COOH) transported across epithelium layer of intestinal villi and presented at the inner side of intestinal villi.

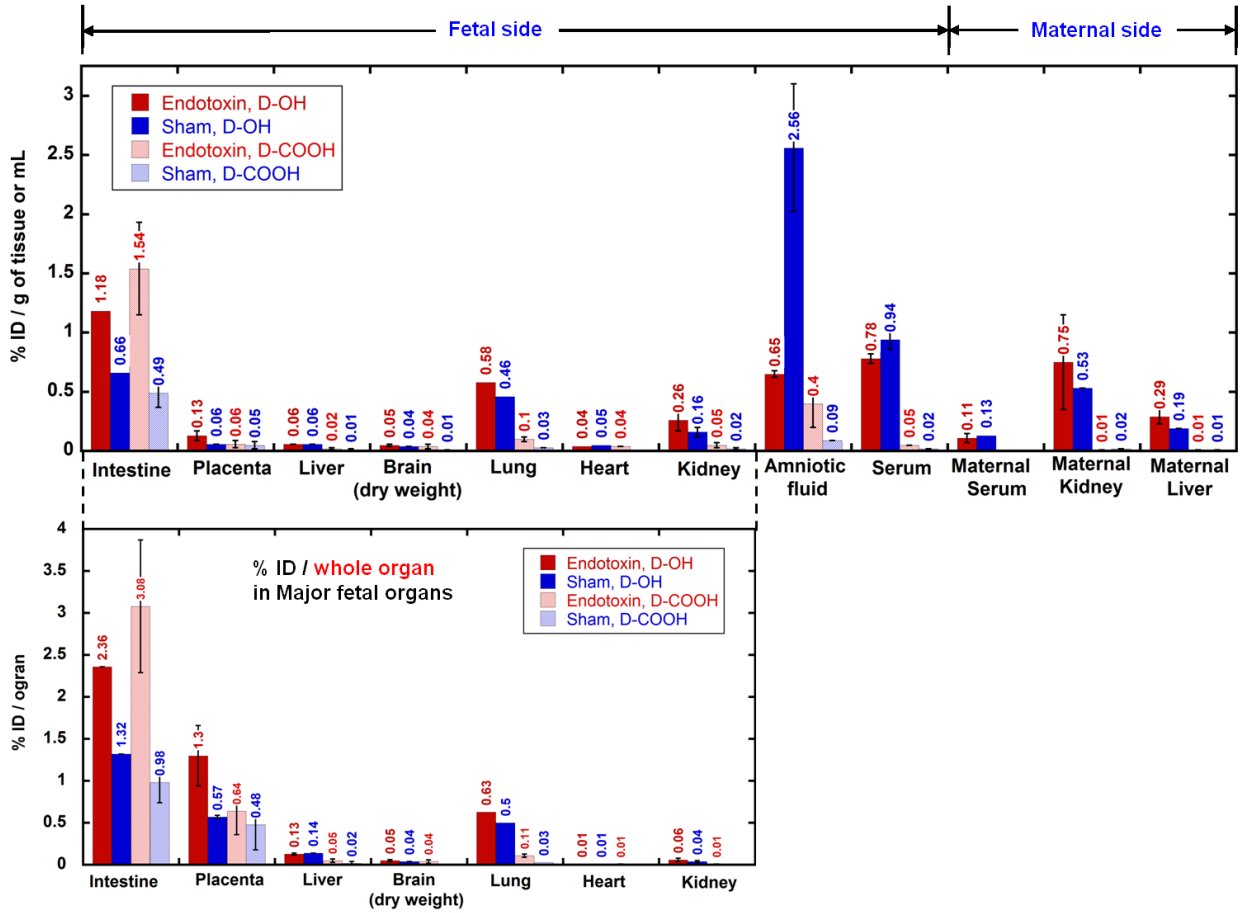


**Figure 3.53. Biodistribution of dendrimers at 24 hours post intra-amniotic administration.** D-OH, indicated by solid columns and D-COOH, indicated by shaded columns, endotoxin group (red columns) and sham groups (blue columns). Biodistribution is expressed as % injected dose per gram of tissue or milliliter of fluid [%ID/g of tissue or mL] (top) and % injected dose per whole organ in major fetal organs [%ID/organ] (bottom).

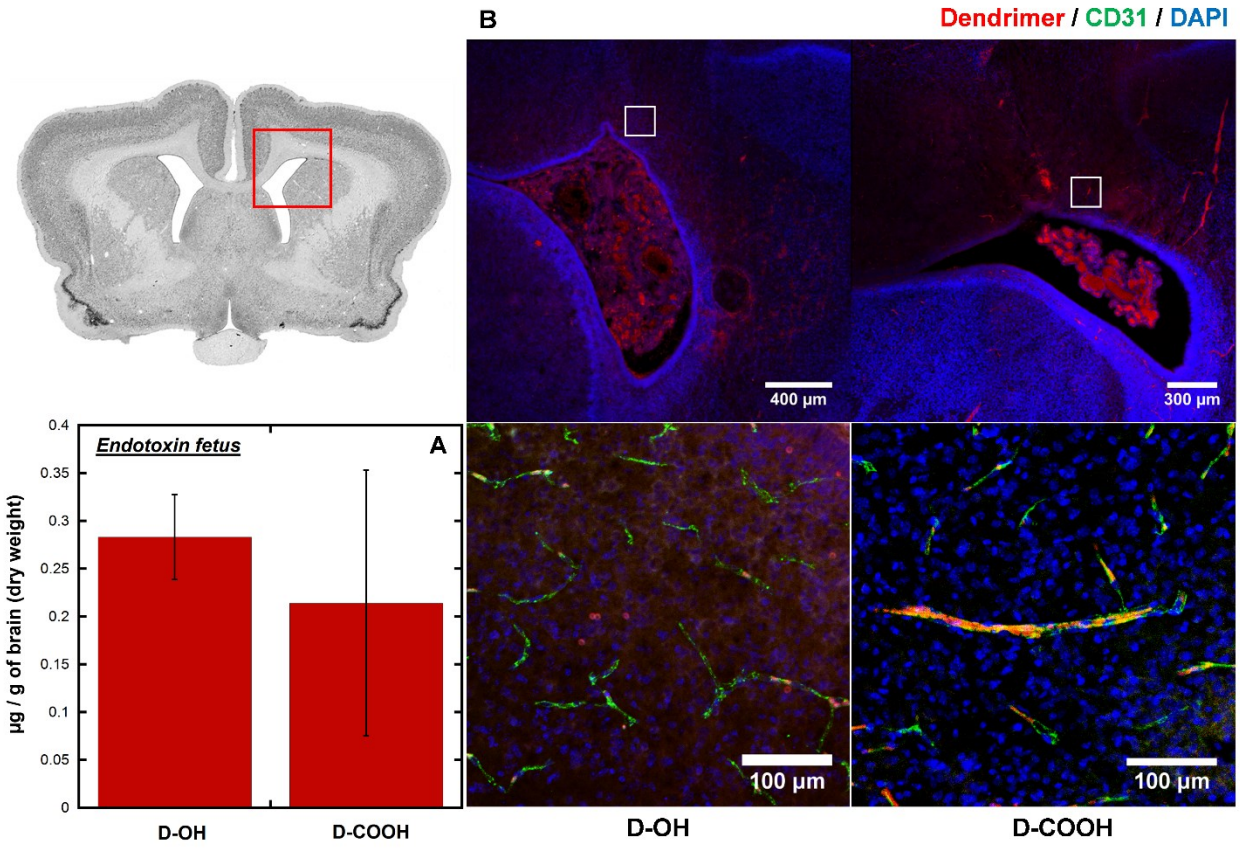


**Figure 3.54. Dendrimers accumulation and distribution in the brain of endotoxin exposed fetuses at 24 hours post intra-amniotic dendrimers administration.**

(A) Whole brain quantification shows both D-OH and D-COOH has similar accumulation in the brain of endotoxin exposed fetus. (B) Immunofluorescence study shows completely different distribution of D-OH and D-COOH in the brain of endotoxin exposed fetuses. D-OH escapes the impaired BBB, distributes in the brain parenchyma around the periventricular region; D-COOH is only observed to be restricted to the blood vessels. Red: D-OH or D-COOH; Green: Anti-CD31 labeled endothelial cells on BBB; Blue: DAPI.

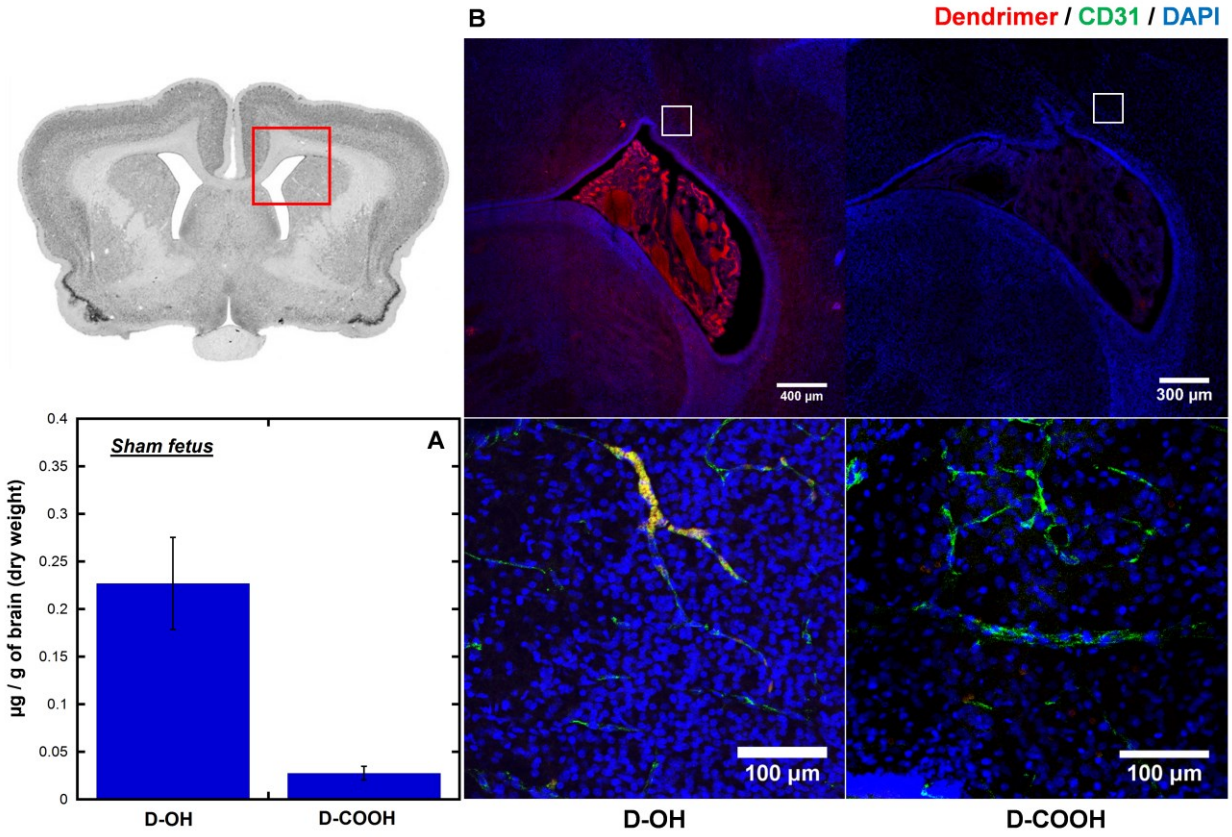


**Figure 3.5.5. Dendrimers accumulation and distribution in the brain of sham fetuses at 24 hours post intra-amniotic dendrimers administration.**

(A) Whole brain quantification shows D-OH accumulates higher than D-COOH in the brain of sham fetuses. (B) Immunofluorescence study shows different distribution of D-OH and D-COOH in the brain of sham fetuses. D-OH is mainly restricted to the blood vessels, and is not presented in the brain parenchyma, while D-COOH is barely seen. Red: D-OH or D-COOH; Green: Anti-CD31 labeled endothelial cells on BBB; Blue: DAPI.

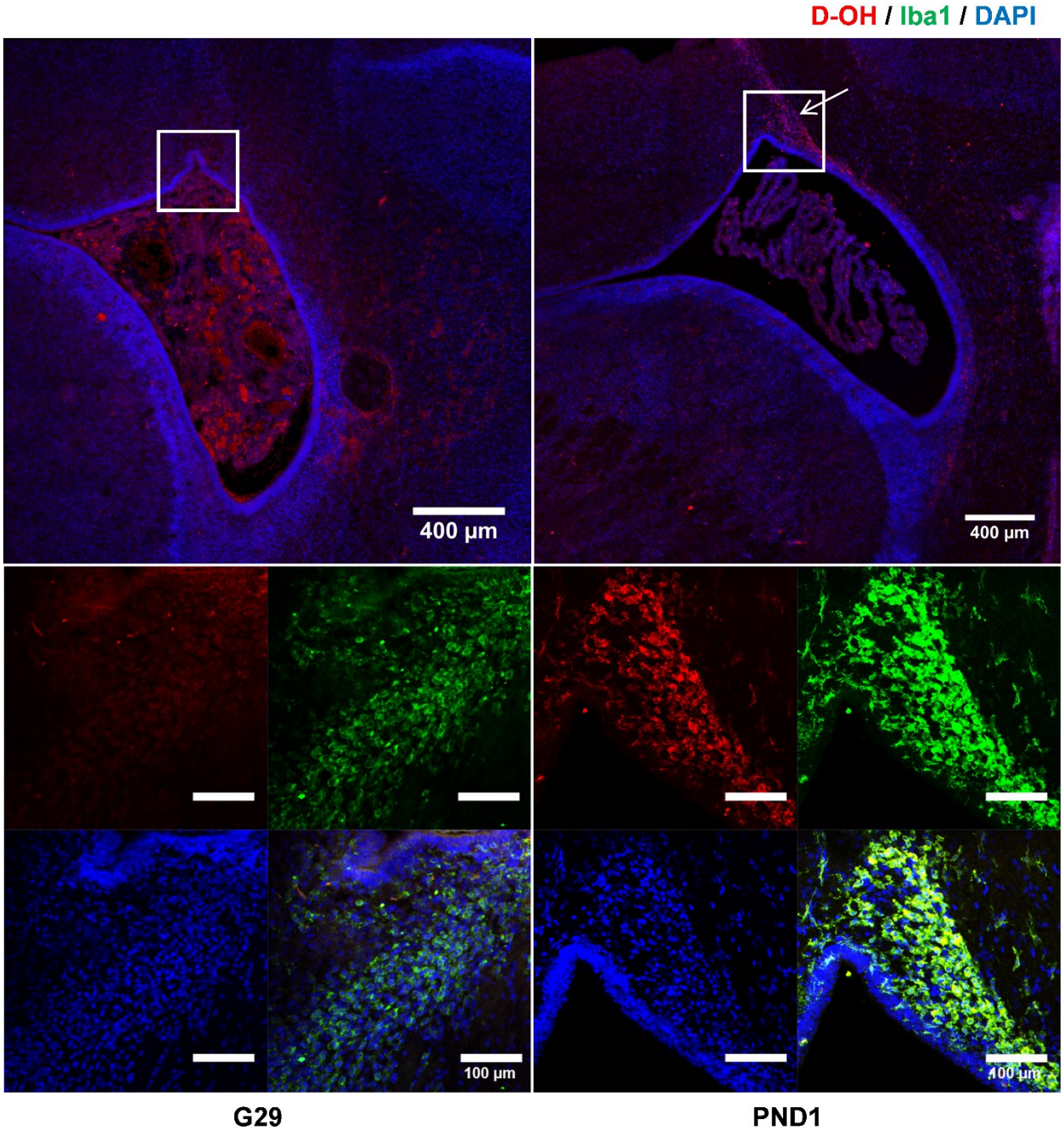


**Figure 3.56. D-OH microglia localization was accompanied with microglial activation.**

Low magnification image (top) showed that at G29, most D-OH distributed around the ventricle region, while at PND1, D-OH specifically accumulated at the ventricle horn (pointed out by the arrow). Magnification of the ventricle horn (bottom) showed that at G29, hint of microglial

localization was observed, while at PND1, D-OH was selectively localized within the activated microglial cells. Red: D-OH; Green: Anti-Iba1 labeled microglial cells; Blue: DAPI.

# 4. NEUROINFLAMMATION AFFECTS MICROGLIA MIGRATION AND INTERACTION WITH DENDRIMERS

## 4.1. Introduction

Microglial cells are the primary resident immune cells in the central nervous system (CNS). Their migration dynamics are associated with their functions in the CNS [141, 142, 143]. Under physiological conditions, microglia are ramified cells, with highly motile processes to help survey and maintain the brain microenvironment around them [144]. In response to any acute brain injury or damage, these surveying microglial cells can rapidly transform into an activated state and migrate to the injury site [145, 146, 147, 148]. However, in neurodevelopmental disorders such as cerebral palsy (CP), where activated microglial cells have been implicated, the migration dynamics of microglial cells are not well-understood [149]. Previous studies using primary microglial cell cultures have demonstrated that lipopolysaccharide (LPS) suppresses microglial migration and process extension, while IL4 and TGF-β promote microglial migration and branching [149, 150, 151]. However, microglial migration dynamics in a more representative biological environment, such as the brain parenchyma, especially in the presence of pathology, have not been adequately explored.

Microglial cells have the ability to phagocytose stressed or dying neurons and express phagocytic receptors on their surface [12]. In neuroinflammatory and neurodegenerative disorders, pro-inflammatory microglia become neurotoxic by secreting reactive oxygen species and cytokines as a response to various environmental stimuli, causing injury to neurons [152, 153, 154, 155]. We have previously demonstrated that systemic administration of a poly(amidoamine) (PAMAM) dendrimer (~4 nm) results in its selective accumulation in activated microglia in the brain of newborn rabbits with CP, but not in healthy, age matched

control rabbits. We have also shown that newborn kits with CP had evidence of ongoing inflammation and oxidative injury in the brain even on day 5 of life (8 days after the insult). When N-acetyl cysteine (NAC), a broad anti-oxidant and anti-inflammatory agent with poor brain penetration, was conjugated to dendrimers and administered systemically on day 1 of life (3 days after the insult) to rabbit kits with CP, a dramatic improvement in motor function and attenuation of neuroinflammation was noted by day 5, and was significantly more effective than free drug at a 10 time higher dose[86]. However, since the dendrimers do not cross the intact blood brain barrier (BBB) in healthy rabbits, it is unclear what role the 'activated' nature of pro-inflammatory microglial cells play in the dendrimer uptake, as the BBB impairment in this rabbit model of CP would allow a greater amount of dendrimer exposure within the brain parenchyma to the pro-inflammatory microglial cells.

To address these questions, and further understand the dynamic functions of microglial cells in this *in vivo* rabbit model of CP, we created an *ex vivo* organotypic whole hemisphere-brain slice culture model, with preservation of the microglia pathology in an *in vivo* condition. Using this platform, we evaluated microglial migration and interactions with dendrimers in brain slices obtained from newborn rabbits with CP, and compared to that of healthy control newborn rabbits. We found that inflammation led to impairment in the surveillance function of microglial cells, as demonstrated by hindered migration of microglial cells in the brain of newborn kits with CP compared to healthy control kits. Inflammation also influenced the mechanism of microglia-dendrimer interactions, with enhanced and more rapid dendrimer uptake by the microglial cells in brain slices from kits with CP. A better understanding of the dynamics of microglial migration in the presence of inflammation and their interactions with dendrimer nano-devices will provide

valuable information for evaluating and designing targeted drug delivery systems that can be used to modulate microglial function and interactions.

## 4.2. Materials and Methods

### *4.2.1. Materials and reagents*

Cyanine5 NHS ester-labeled hydroxyl terminated Generation 4.0 Poly(amidoamine) (PAMAM) dendrimer (D-Cy5, or referred to as dendrimer in this paper) was synthesized using a previously established protocol [95]; Tomato lectin- DyLight 594 (Vector Lab, USA); Goat anti-Iba1 (Abcam, USA); Donkey anti-goat-Alexa flour 488 (Invitrogen, USA); and 4',6-diamidino-2-phenylindole (DAPI) (Invitrogen, USA) were purchased and used for the studies;

### *4.2.2. Animals*

All animal procedures were in accordance with the Animal Care and Use Committee guidelines at Johns Hopkins University and the United States Department of Agriculture, as described previously [135, 156]. Timed pregnant New Zealand white rabbits were obtained from Robinson Services Inc. (Winston-Salem, NC). Briefly, pregnant rabbits in the endotoxin group underwent laparotomy at gestational day 28 (term pregnancy is 31 days) and were injected with 1 mL of saline containing Escherichia coli endotoxin (~6000EU) (serotype O127: B8, Sigma Aldrich) along the length of the uterus. At this dose, the newborn kits have been shown to have uniform pro-inflammatory microglial activation in the periventricular region (PVR), along with increased expression of TNF-α and display a phenotype of CP with predominantly hindlimb hypertonia [86, 156]. The healthy control group included pregnant rabbits that had no surgery or intervention. All pregnant dams were induced on the evening of gestational day 30 (G30) to

control timing of delivery and kits were used for the experiments on postnatal day 1, corresponding to G31.

*4.2.3. Organotypic whole hemisphere-brain slice preparation*

Organotypic whole hemisphere brain slices were prepared based on modifications to previously published protocols [145, 157, 158]. Rabbit brain slices (350 μm thick) were prepared from neonatal rabbits with CP or from age matched healthy controls. To prepare the brain slices, neonatal rabbits were decapitated under aseptic conditions after euthanasia. The brain was removed, dissected into two hemispheres, and sectioned immediately into 350 μm thick whole hemisphere brain slices using a Mcllwain tissue chopper (TED PELLA, Inc., USA). For each hemisphere, 6 consecutive slices at the level of the bregma were carefully separated in the dissection medium (3.2g Glucose/ 500ml HBSS, 1% of penicillin), while maintaining the structures of whole hemisphere-brain slices intact. The lateral ventricle was clearly visualized in all the slices. The separated brain slices were transferred onto 30 mm diameter, sterile, porous (0.4 um) transparent and low-protein-binding membrane inserts (Millicell-CM, Millipore) in 6-well tissue culture plates. Each well was prefilled with 1 mL of culture medium, prepared from 200 mL MEM, 100 mL HBSS RED, 100 mL Horse Serum, 4 mL Glutamax and 1% penicillin. The slices were maintained overnight at 37 °C in a humidified atmosphere with 5% CO2 before confocal imaging. For the slice viability studies, new culture medium was replaced every two days.

*4.2.4. Evaluation of the viability of brain slices under culture*

The whole hemisphere-brain slice viability was evaluated using LDH assay (Cayman, USA), which measures the lactate dehydrogenase (LDH) released into the culture medium from degenerating cells in brain slices [159]. Culture supernatants from 3 different CP slices were

collected at various time points up to 10 days of incubation and replaced with fresh medium at each time point (time points evaluated were 6 h, 19 h, 27 h, day 2, day 3, day 5, day 6, day7, day10) and frozen at -80 °C. The dilution of LDH in the supernatant was taken into account in the calculation. The percentage of LDH released in each whole hemisphere-brain slice was quantified by measuring the fluorescence intensity, subtracting the background in negative control (culture medium at 0 h of slice culture) and normalized by the intensity of positive control (culture medium collected from brain slices treated with Triton-X 100 for 10 days).

*4.2.5. Time-lapse imaging of microglial migration*

Time-lapse imaging of microglial cell migration in brain slices was carried out using a LSM 710 inverted fluorescence confocal microscope (Zeiss, USA). In preparation for imaging, whole hemisphere-brain slices from neonatal rabbits with CP and their age matched controls were carefully removed from the insert after overnight incubation and simultaneously transferred to a lysine coated glass-bottom culture dish (MakTek Corp, USA). Control and CP brain slices were stained and imaged in pairs simultaneously to maintain the same conditions between groups. To stain the microglial cells, brain slices were incubated with 10 µL of Tomato Lectin 594 added to 1 mL of culture medium for 45 min, and then washed three times with the medium to remove unreacted tomato lectin. To fix the slice onto the glass-bottom culture dish, 30-40 µL of matrigel were applied around the brain slices and then incubated at 37 °C for 15 min to allow curing. Culture medium without phenol red was then added into the glass bottom culture dish such that it just covered the brain slices. Time-lapse imaging was carried out in the environmental chamber under 37°C and 5% CO2 to allow the brain slices to maintain its normal physiology. Prior to imaging, the environmental chamber was pre-equilibrated for 30 min. To decrease the possibility of any laser induced injury to the cells and photobleaching to the fluorescence labeled

dendrimers, a low laser power index of 0.5 was used. Image quality was maintained by using a comparatively larger pinhole size and higher gain number to compensate for the decrease of laser power. A 20X tilescan with a Z stack of 2-5 μm interval in the vertical direction was used to image a tissue dimension of 1 mm × 1 mm in area and 50-80 μm in thickness, and 50 μm in depth at the periventricular region. An average of 40-50 microglial cells were imaged per slice. The movie was recorded at a temporal resolution of 15 min for 5.5 - 6 h. Maximum intensity projection was applied for the final image process.

*4.2.6. Evaluation of dendrimer uptake by microglial cells*

To evaluate the dendrimer uptake by microglial cells, freshly prepared whole hemisphere-brain slices from rabbits with CP and age matched healthy controls were incubated with dendrimer tagged with Cy5 (D-Cy5) (5 ng in 10 μL of sterile DPBS solution) 4 hours after slices were sectioned. The D-Cy5 solution was topically pipetted on the tissue along the medial border of the lateral ventricle. This region is typically where microglia are seen in high density in newborn rabbits [135, 160]. The slices were then incubated at 37 °C in the presence of 5% CO2 to allow dendrimer to diffuse though the brain tissue and interact with microglia. Slices were collected after 1 h, 4 h and 12 h of treatment. At the end of the treatment, the slices were washed with cold DPBS solution (4 °C) to inhibit active mechanisms of cell uptake and to remove excess dendrimer that is not taken up intracellularly. Brain slices were then carefully transferred to 4% formalin solution and 20% sucrose solution for fixation. Slices were incubated overnight with Goat Anti-Iba1 for microglia, followed by donkey anti-goat Alexa flour 488 as secondary and DAPI for nuclear staining. The stained brain slices were imaged with a20X lens with 3×3 tilescan, Z-stack with a thickness of 100 μm. The parameters for Cy5 channel were kept consistent throughout all images to make them comparable.

*4.2.7. MATLAB Analysis of microglia movement*

The recorded cell migration was analyzed using MATLAB software. For each group (CP vs. Healthy), 3 slices each obtained from different animals were analyzed. Microglia movement rates were obtained by transforming the coordinates of microglia centroids into time-averaged mean square displacement (<MSD>), calculated as $<MSD(\tau)> = [x(t + \tau) - x(t)]2 + [y(t + \tau) - y(t)]2$ , where x and y represent the cell coordinates at a given time and $\tau$ is the time scale or time lag. The acquired <MSD> was analyzed using the diffusion function in a 2D scale $<MSD (\tau)>=4D\tau\alpha$, where D is the diffusion coefficient, which in our case, is related to the microglial cell migration. $\tau$ is the time lag and $\alpha$ is the dynamic exponent. When $\alpha=1$, the diffusion or cell movement tends to be Brownian motion. When $0<\alpha<1$, the diffusion or cell movement is considered to be hindered. When $\alpha>1$, the diffusion or cell movement is considered to be active transport which is governed by other factors, such as chemokine or cytokine sensing.

*4.2.8. Analysis of microglial migration velocity and persistent distance*

The analysis of microglial migration velocity and persistent distance was based on the time-lapse videos recorded by LSM710 confocal microscopy. The speed of microglial migration was determined by tracking microglial cell migration path using image analysis software in Metamorph. Information such as coordinates and distance at each time point, was recorded. Based on this information, the migration speed and persistent distance were calculated by averaging the migration velocity at each migration step. The persistent distance is defined as the distance ($\geq$ 10μm) traveled by a microglial cell before it makes a significant change in direction (absolute angle between previous direction and new direction <70°) [161].

*4.2.9. Imaris analysis of microglial cell surface to volume ratio (S/V) and dendrimer co-localization*

To evaluate the change in morphology of the microglia in brain slices from CP kits when compared to those from age matched healthy control newborns, 3D representations of Anti-Iba1 stained microglia in fixed whole-hemisphere brain slices were acquired using confocal microscopy with 40X magnification, with 3×3 tile scans, extending 10 μm in the Z direction with 1 μm Z-stacks. To analyze the image, Imaris software was applied and microglial surface to volume (S/V) ratio was measured. The function 'surfaces' was used, and the microglia from different slices (n=3 slices/group from 3 different kits each, for the CP and control groups) were analyzed for S/V ratio at the beginning of incubation and 24 h post incubation [150].

To study the dendrimer uptake by microglial cells, we used the 'spot' function to detect microglial cells and dendrimer accumulation. For the detection of dendrimer accumulation, a threshold was set, where only dendrimers with signal beyond this threshold were considered detectable. The 'co-localization' function was used to determine whether cell uptake was present. In detail, the estimated diameter chosen was 7 μm, 10 μm, and 10 μm, respectively, and the threshold was automatically set for 'Quality' analysis to 5000, 4000, and 7000, respectively. The function 'co-localize spots' was used and a 10 μm distance threshold was chosen.

*4.2.10. Statistical Analysis*

Statistical analysis of data was carried out by using student's t-test. Differences were considered statistically significant at $p < 0.05$.

## 4.3. Results

### *4.3.1. Whole hemisphere brain slice viability and microglial pathology is maintained throughout the observation window*

Assessment of LDH activity from the medium has been widely used to quantify cell death in primary cell cultures. Similarly, in tissue slice culture, the measurement of LDH efflux into the culture medium has been found to be highly correlated with the results of cell death from cell counting [162]. To determine the cellular viability of the slices, the LDH levels in the supernatant were measured. All microglial studies were conducted and completed within the first 27 h, during which time there was no increase in LDH levels (Figure 4.1), indicating that there was no increase in cell death over time during the observation period. This implies that the tissue stability was maintained during this period. We found that the brain slices maintained good viability during the time frame when these experiments were conducted, without an increase in LDH release.

To validate whether the acute study (observation window within 24 h) allowed the preservation of *in vivo* pathology of microglial cells, we evaluated the differences in microglial morphology between CP and healthy control kits over time in brain slices by quantifying microglial surface area to volume (S/V) ratio (Figure 4.2). Microglial cells in the brain slices from healthy control kits demonstrated several extended processes with small cell bodies, while microglial cells in the brain slices from CP kits had enlarged cell bodies with several short, thickened processes (identified with arrow in Figure 4.2). These morphological variations lead to differences in the microglial cell S/V ratio, with S/V close to 1.5 μm-1 in the healthy controls and S/V ratio less than 1 μm-1 in the CP kits. At 24 h, the end of our observation window, a statistically significant difference in S/V ratio between microglia in the healthy brain slices and

CP brain slices can still be observed. This difference was noted despite a generalized decrease in the S/V ratio of microglia in both healthy and CP brain slices over time. This decrease over time from baseline is probably related to a normal response of the microglia to the shear force generated during tissue section. In our *in vivo* model of CP, we observed a similar difference in morphology with decreased branches and larger cell bodies in the microglia in kits with CP compared to healthy control kits [86].

Specifically, the viability of neonatal brain slice culture platform was evaluated by measuring the LDH released in the supernatant during 10 days of incubation time (Figure 4.1). In general, cells in the brain slices showed increasing degeneration rate with longer incubation time, with ~10% of total LDH released at the beginning of incubation and ~50% at the end of incubation (10 days). Although there was ~10-20% LDH release caused by shear force induced cell damage during the slicing of the brain prior to incubation, cells in the brain slices quickly equilibrated with the *ex vivo* media culture environment, as indicated by the stable level of LDH for the first 24 h of incubation. LDH levels remained stable for 3-5 days of incubation time after slicing, indicating no increase in cell death and maintenance of tissue viability during this time period which provides an observation window long enough for the studies of cell mobility and dendrimer uptake.

*4.3.2. Microglial migration is different in brain slices from CP animals compared to brain slices from healthy control animals*

To investigate the influence of inflammation on microglial migration, we used the mean square displacement (<MSD>) of individual microglia to quantify the migration in the brain slices. We found a higher fraction of 'active migration' for microglial cells in the brain slices

from healthy control animal slices, and a higher fraction of ‘restrictive migration’ for microglial cells in CP, indicating impaired migration of microglia in the CP rabbit brain.

Throughout the imaging time span of 5.5 h, the average <MSD> for the microglia was greater in the control brain slices compared to CP slices. The increased migration was reflected in the ‘diffusion coefficient’, which is the intercept of the log plot of the <MSD> vs. time graph (Figure 4.3A). The microglial trajectories were individually plotted and migration distance from the starting point was measured. Microglia in the control brain slices had a much greater migration distance compared to those in the slices from CP rabbit kits (Figure 4.3B). To quantify this difference, we classified all microglial migration trajectories as 'active transport' or 'restrictive transport'. Specifically, the microglial migration trajectories in both groups of slices were re-plotted by aligning the starting point of each trajectory at the same origin, and by defining the cell migration with displacement greater than 20 μm as active transport while displacements less than or equal to 20 μm were considered as restrictive transport (Figure 4.4A). Over one-half the microglia in the healthy slices (52%) had an active migration pattern with a migration distance more than 20 μm from their starting point; while only 17% of microglial cells in the CP brain slices demonstrated active migration, 83% of microglial cells in the CP brain slices demonstrating restrictive migration (Figure 4.4B).

To investigate the difference in microglial migration between the healthy and CP slices, we used migration velocity and persistent distance to evaluate migration patterns (Figure 4.5). In general, microglial cells had a wide distribution of migration velocities. Microglial cells from healthy brain slices had migration velocities ranging from ~0.1 μm/min to 1.5 μm/min. This range was wider, and the velocities were higher than those of microglial cells from CP brain slices, which had migration velocities ranging from ~0.05 μm/min to ~0.3 μm/min. This resulted

in a higher average microglial migration velocity in healthy brain slices (~0.33±0.31 μm/min; mean ± SEM) than in CP brain slices (~0.19 ± 0.08 μm/min). Persistent distance is a parameter used to measure the interactions of the cell with its matrix regulated by adhesion proteins [161]. We adopted this parameter and used it as an indication of impediments encountered by microglia during migration. The lower persistent distance demonstrated by the microglial cells from CP brain slices compared to healthy slices (population median: 15.22 vs. 30.3 μm) may suggest there was a greater hindrance for impaired microglia to migrate.

*4.3.3. Dendrimer uptake is affected by microglial pathology*

We have previously reported that intravenous administration of dendrimers resulted in increased accumulation in activated microglia in newborn rabbits with CP, but not in healthy controls [86, 95]. A similar differential uptake was found between the microglia in healthy control brain slices and in CP brain slices.

In the brain slices from healthy animals, only 20% of microglial cells had detectable dendrimer uptake after 1 h of dendrimer treatment (Figure 4.6A). The uptake remained at the same level, without obvious increase in uptake even after 12 h of dendrimer treatment, indicating limited interactions between dendrimer and microglial cells in the healthy brain slices. This can be observed in Figure 4.6B, where the dendrimer signal barely observed. In brain slices from CP kits, dendrimer uptake by microglial cells occurred more rapidly and to a greater extent, with 50% of microglial cells containing dendrimer after 1 h treatment. Microglial uptake of D-Cy5 increased 1.6-fold after 4 h of dendrimer treatment, in the brain slices from CP kits, with ~80% of total microglial cells containing dendrimer (Figure 4.6A). No obvious increase in the number of microglial cells containing dendrimer was observed beyond this time point, suggesting that dendrimer uptake by microglial cells peaks around 4 h without substantial increase in uptake

beyond. This is also depicted in Figure 4.6B, where substantial co-localization of D-Cy5 in microglia can be seen by 4 h of treatment in the brain slices from CP kits with relatively less cellular co-localization observed in the healthy brain slices even at 12 h (Figure 4.6B).

## 4.4. Discussion

In this study, we show that maternal intrauterine endotoxin exposure results in a morphological change of the microglia with retraction of the processes, restrictive microglial migration, and a more rapid and enhanced dendrimer uptake in the newborn rabbit brain with CP when compared to age matched healthy controls. These observations provide insights to why the dendrimer-drug conjugates are therapeutically effective, since the dendrimers diffuse more rapidly in the brain (and are able to 'find' the less mobile activated microglia), while taking advantage of their increased ability to engulf/uptake dendrimers.

*In vitro* and *in vivo* models are commonly used to study the morphology, behaviors, and functions of microglia. *In vitro* platforms, including primary cell cultures, allow the extraction of high purity microglial cells [163]; however, *in vitro* methods involve destruction of the primary architecture and biological environment of the CNS. The physiology or pathology is well maintained in *in vivo* platforms, but it is experimentally difficult to visualize and monitor the biological process in specified anatomical locations, especially for regions deep within the brain [164]. On the other hand, the *ex vivo* organotypic whole hemisphere-brain slice platform maintains many aspects of *in vivo* characteristics, such as the 3D structure of the CNS, making it possible for microglial cells to interact with the biological environment around them [145, 165, 166]. Using organotypic whole hemisphere-brain slices as a platform in this study also allows us to access and precisely monitor the cells at a specific anatomical location, i.e. the PVR which is

the primary area involved in CP. Since the goal of this study was to evaluate the interactions of the dendrimer with microglial cells, while avoiding the biological barriers such as the BBB and clearance by other organs, the organotypic whole hemisphere-brain slices were an appropriate *ex vivo* platform. Here, we transferred an *in vivo* animal model of CP into an *ex vivo* brain slice model of CP. Our results suggest that these differences in microglial morphology between the two groups, as observed in our *in vivo* model, were also maintained in our organotypic slices [156].

The study of microglial migration is associated with the understanding of microglial function in the brain, and how they might be affected differently under acute injury and inflammation. In the healthy brain, microglia serve a house keeping function by continually surveilling the brain microenvironment, pruning neurons, and clearing accumulated metabolic products or deteriorated tissue components in parenchyma [144, 167]. *In vivo* studies in the adult mouse brain have revealed that, to perform these functions, microglial cells are highly dynamic, where their processes continuously undergo cycles of de novo formation and withdrawal (on a time scale of a few minutes) without obvious movement of their cell somata [144]. However, under conditions of acute insult, such as laser-induced neuronal injury or blade induced lesion, microglial cells quickly react to these insults and transform into a motile form with increased migration [144, 168, 169, 170]. This finding was demonstrated in *ex vivo* studies in neonatal rats/mice organotypic brain slices [145, 171]. The shear force generated during the slicing process induces mechanical stimulation. Microglia under normal physiologic condition react to this stimuli by quickly transitioning into a motile mode within a time period of a few hours, and translocating their cell somata, enabling direct physical contact with many cells within a short

period of time, and supporting a tissue surveillance function [145]. This was also demonstrated by microglial cells in the brain slices from healthy control animals in our study.

However, in the presence of inflammation, microglial cells behave differently. Inflammation induced by LPS can polarize microglial cells into a pro-inflammatory phenotype [172, 173]. Studies in primary microglial cell cultures have found that exposure to LPS led to decreased microglial migration. Although the mechanisms are not fully understood, LPS has been shown to impair microglial migration by down regulation of the P2Y(12) receptor, which promotes microglial migration in response to ATP/ADP release [150, 151]. Similarly, in our slices obtained from newborn rabbits with CP, microglial migration decreased, as shown by lower <MSD> and reduced migration speed, with a higher population of microglia characterized by restrictive migration when compared to the microglia in the healthy brain. This restricted and decreased migration would indicate the impairment in the normal surveillance function of the microglia. It is possible that this impairment in surveillance function of pro-inflammatory microglia may play a role in mediating ongoing, chronic inflammation in neuroinflammatory/neurodegenerative disorders [153, 174]. Persistence of cell migration, a measure to evaluate the ability to migrate in the same direction without turning, has been used in studying cell migration, including for cancer cells [175]. The persistent distance of the cell migration trajectory may be regulated by multiple mechanisms, including microtubules, adhesion proteins, and chemotactic signals [161, 176, 177, 178]. In this study, it was found that microglia demonstrate reduced persistent distance in the presence of inflammation. This may be explained in part by increased microglial adhesion to the ECM component laminin, due to the up-regulation of the membrane protein integrin on microglia when exposed to pro-inflammatory

cytokines [179, 180]. Integrin expression is known to regulate the adhesion and migration of cells in the CNS [179].

In our maternal inflammation-induced rabbit model of CP, we have previously reported an increase in the uptake of systemically-administered hydroxyl terminated PAMAM dendrimer (dendrimer) by 'activated' microglia in the newborn brain of kits with CP, but not in the healthy neonatal rabbit brain [86]. In the *in vivo* model, the impairment of the BBB in the CP animals may lead to greater exposure of the microglia to the dendrimer in the brain in these animals. However, in the *ex vivo* model, microglia in the healthy brain slices and the CP animal derived brain slices, are exposed to the dendrimer to the same extent, due to direct contact of the dendrimer to the slice. The substantially greater and more rapid uptake of dendrimers by microglia in the CP rabbits when compared to healthy controls may indicate up-regulation of the cellular uptake mechanisms by the microglia in CP kits. This is in spite of some levels of 'activation' in both groups due to the shear forces induced by slicing the brain tissue. Microglial cells possess full range of endocytic mechanisms, including receptor-mediated endocytosis, macropinocytosis and phagocytosis [181]. Upregulation of any or all of these processes in pro-inflammatory microglial cells in the CP brain [152] could be responsible for the enhanced dendrimer uptake and intrinsic targeting of the dendrimers that can be exploited for targeting therapeutics specifically to activated microglia [86, 182, 183, 184, 185].

### 4.5. Conclusions

We used an *ex vivo* brain slice platform that maintained the physiology of surveying microglial cells and pathology of pro-inflammatory microglial cells from an *in vivo* model. Our results suggested there is a significant decrease in the normal migration and surveillance functions of microglia in the presence of neuroinflammation in newborn rabbits with CP.

However, these microglia were able to uptake dendrimer more rapidly and to a greater extent than normal healthy control microglia. Further studies to define the endocytotic processes that are up-regulated in activated pro-inflammatory microglia will help to better understand the mechanisms by which the dendrimer is taken up by activated microglia. This will also help in designing better nanoparticle platforms to target activated microglia.

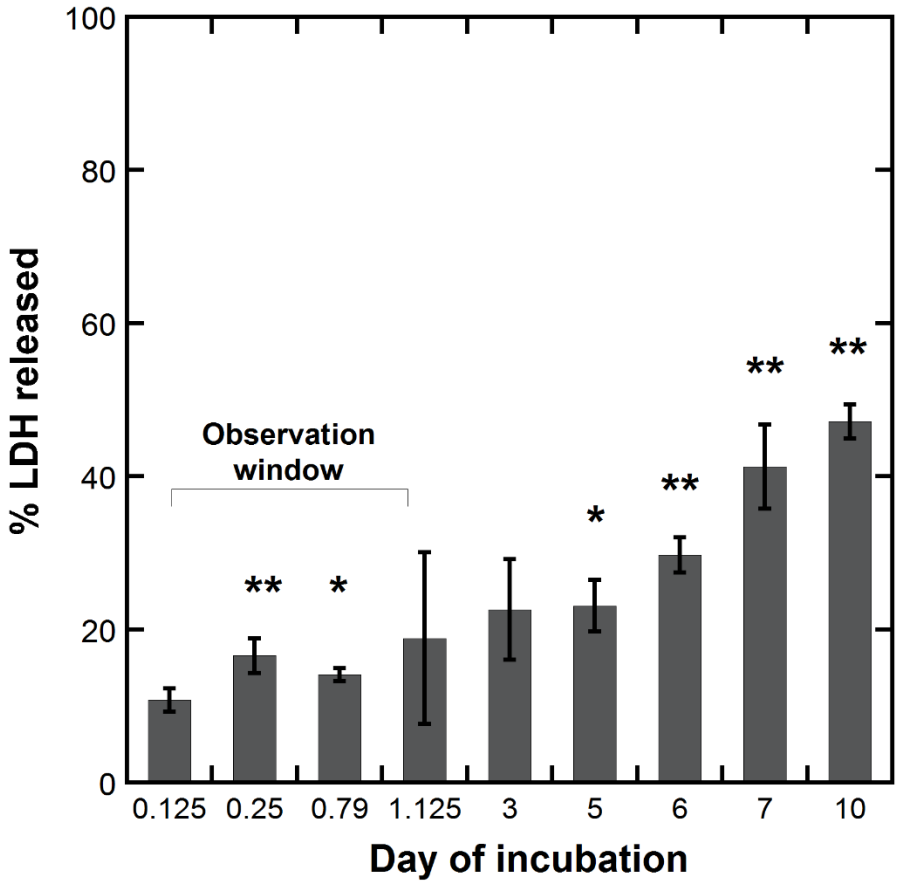


**Figure 4.5.1. LDH release by neonatal rabbit brain slices as an indicator of tissue viability during incubation.**

% LDH released in neonatal rabbit brain slices during 10 days of incubation period. The released LDH concentration is an indicator of the extent of cell death in the whole brain slices. All confocal based experiments were conducted within the observation window. For each time points, 3 brain slices from CP kits were used. For statistical analysis, the % of LDH released at 0.125 h was chose to be the reference. *$p<0.05$, **$p<0.01$.

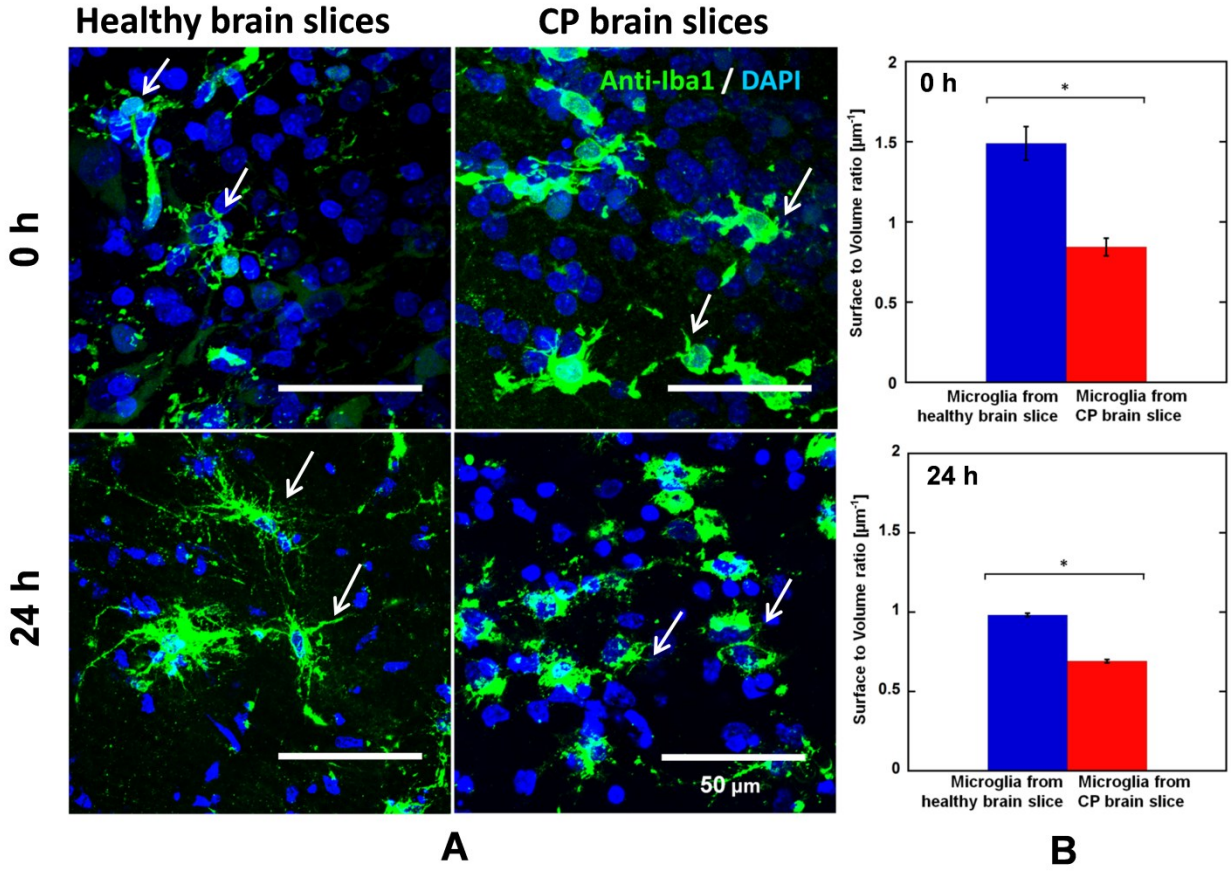


**Figure 4.52. Microglial cells morphology is different in CP brain slices and healthy brain slices within the observation window.**

(A) Representative morphology of microglia cells from cerebral palsy (CP) brain slices and healthy brain slices at 0h and 24 h after incubation; (B) Quantitative study of microglia cell morphology from CP brain slices and healthy brain slices 0 h and 24 h after incubation, the morphology was characterized by cell surface area to cell volume ratio. *$p<0.05$ (Data shown as Mean ±SEM). Scale bar in the figure: 50 µm. For each group, images were acquired from at least 3 different brain slices.

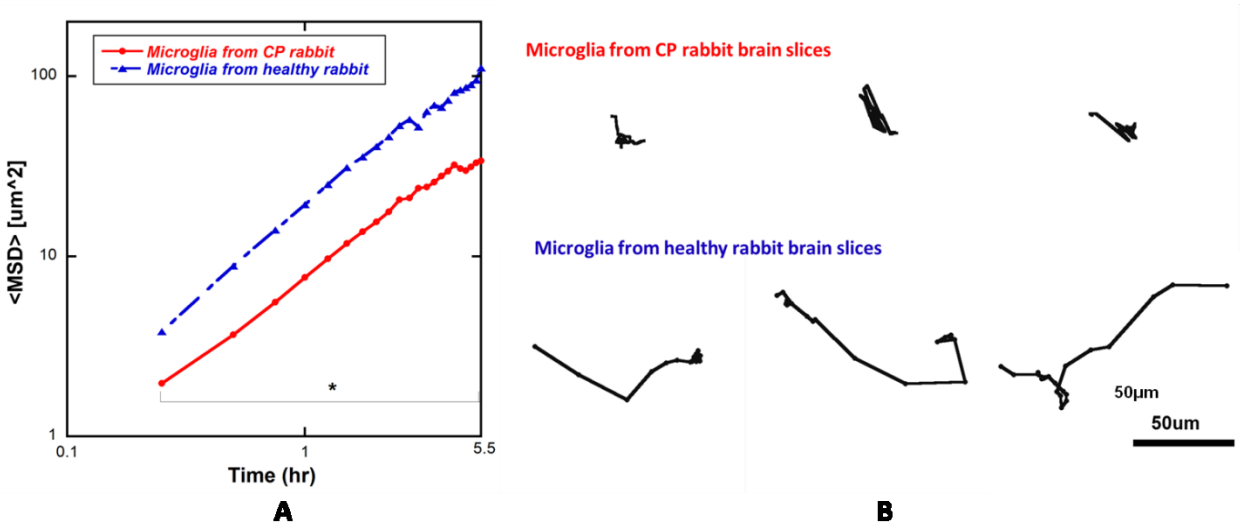


**Figure 4.53. Microglial migration is impaired in brain slices from CP animals vs. healthy animals.**

(A) Microglial cells from cerebral palsy rabbit brain slices (red) had lower <MSD> compared to microglial cells from healthy rabbit brain slices (blue). The <MSD> was plotted in a log scale as a function of time. (B) Representative trajectories of microglia from cerebral palsy rabbit brain slices and healthy rabbit brain slices are shown, *p<0.05.

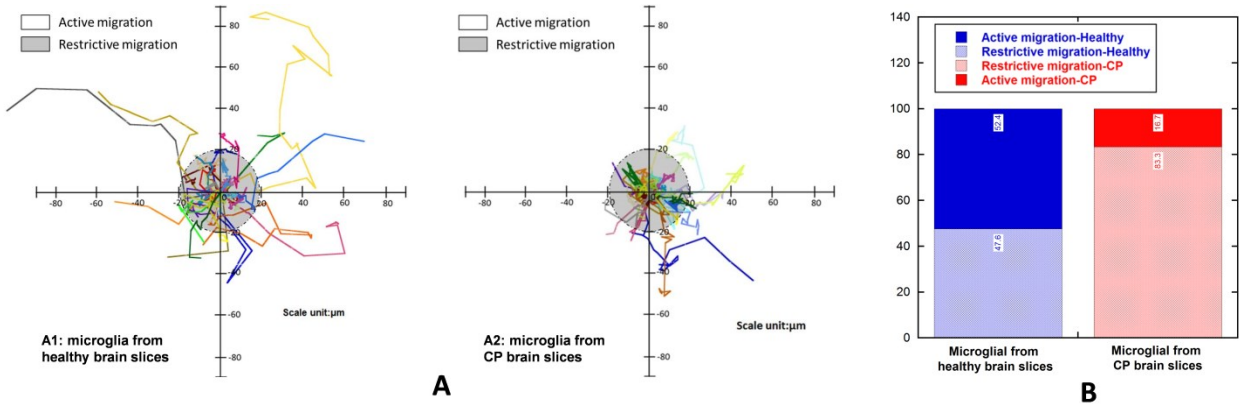


**Figure 4.54. Microglia trajectories showed higher percentage of active migrating microglial cells in healthy brain slices.**

(A) Overlay of individual microglial cells trajectories, plotted after aligning their starting positions. Cells were tracked over a 6h period. Units are in µm. Restrictive migration was defined as microglial cells migrating within 20 µm from their starting point (shaded area); Active migration was defined as migration of more than 20 µm from their starting point. A1: 42 microglial cells from healthy brain slices; A2: 48 microglial from CP brain slices. (B) The quantitative study demonstrated higher 'active migrating' microglia population in healthy rabbit brain slices. In the brain slices from healthy rabbits, more than half the microglia cells (52.4%) showed active migration pattern, while 83.3% of microglia from CP rabbit brain slices showed restrictive migration pattern.

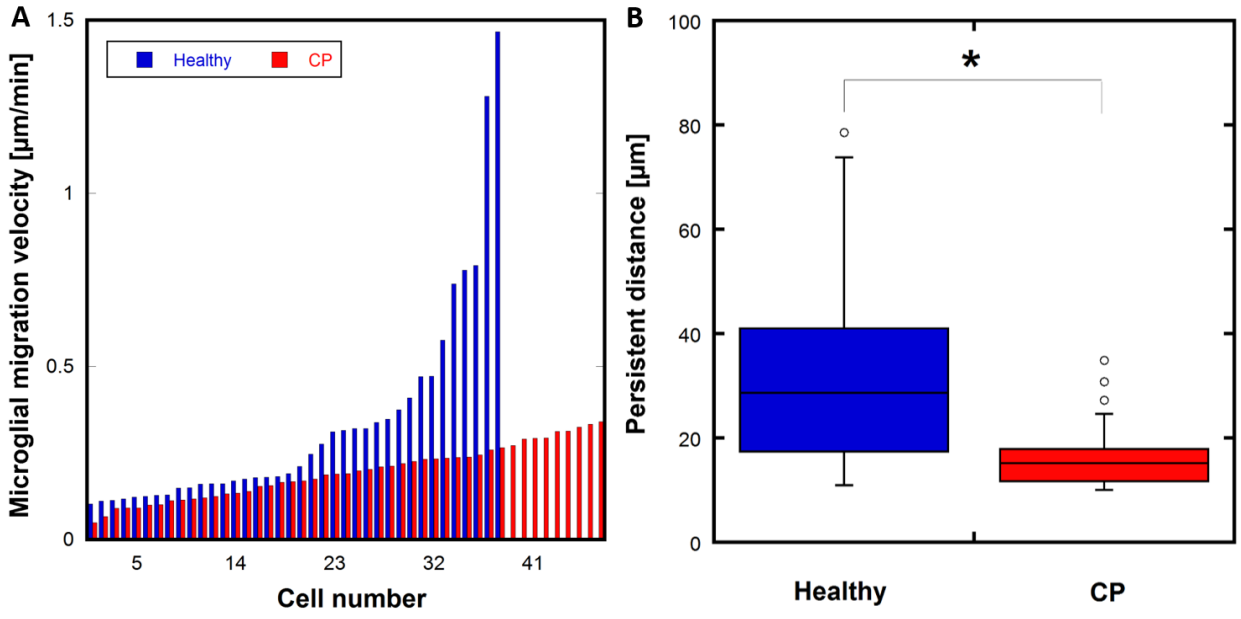


**Figure 4.55. Microglial cells from CP brains showed lower migration velocity and less persistent distance.**

(A) Microglial migration velocity distribution for healthy and CP brain slices. Microglia from healthy brain slices showed higher average migration velocity during the observation period, especially at high migration velocity range, than the microglia from CP brain slices. (B) Persistent distance of microglial migration trajectory is greater in the healthy rabbit brain slices. Persistent migration was defined as the length (>10μm) traveled by a microglial cell before it makes a significant change in direction (absolute angle between previous direction and new direction <70°) *p<0.05 For microglia from healthy brain slice: population median 30.3 μm, 20% percentile:16.6 μm, 80% percentile: 44.4 μm; For microglia from CP brain slice: population median 15.22 μm, 20% percentile:11.6 μm, 80% percentile: 17.9 μm.

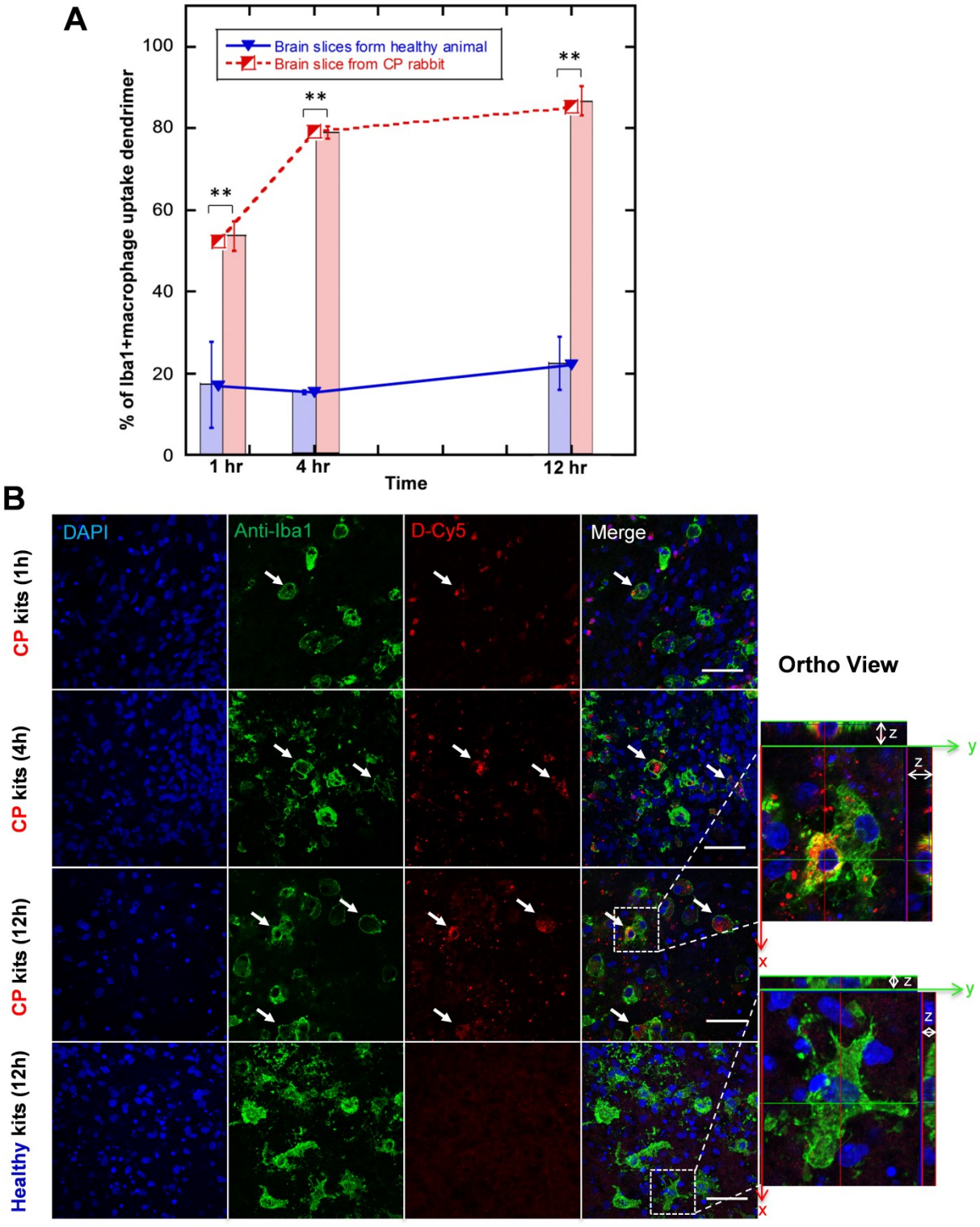


**Figure 4.5.6. Quantitative study of microglial-dendrimer interactions in CP and healthy brain slices.**

(A) Dendrimer uptake by microglial cells, expressed as percent of Iba1+ cells that co-localize with D-Cy5 as a function of time (Mean ± SEM). Red: D-Cy5 uptake in microglia from CP brain slices; Blue: D-Cy5 uptake in microglia from healthy brain slices. N=3 slices/group. **$p<0.01$. (B) Confocal image of dendrimer treated brain slices (CP, taken under 40X magnification) at 3 different time points after D-Cy5 treatment (1h, 4h, 12h), and healthy brain slices after 12 h of D-Cy5 treatment. Microglial cells in CP brain slices had greater dendrimer uptake (indicated by white arrow) than in healthy slices. The orthographic projection clearly indicated the dendrimer uptake by activated microglial cells in the brain slice from CP kit, while the dendrimer was barely seen to localize in microglial cells in the brain slice from healthy kit. Blue: DAPI, Green: Anti-Iba1 (antibody labelling microglia), Red: D-Cy5. Scale bar: 50 μm.

# 5. SIZE AND SURFACE FUNCTIONALITIES AFFECT DENDRIMERS ABILITY TO TARGET CNS DISEASES SYSTEMICALLY

## 5.1. Introduction

Drugs that treat central nervous system (CNS) diseases take more than a year longer to develop and are less than half as likely to obtain marketing approval than other drugs (Tufts CSDD Impact Report, Nov, 2014). The difficulty in achieving improved outcome for CNS diseases stems from the inability to deliver therapeutically relevant doses of the therapeutic to diseased cells or regions [186]. The BBB and the brain parenchyma are two major biological barriers during this process. The BBB continuously regulate the transport of molecules between the CNS and outside. More than 98% percent small molecules and all larger molecules (>500 Da) are excluded from the CNS by BBB [187]. Under many pathological conditions such as neuroinflammation and brain cancer, the integrity of BBB is disrupted, offering opportunities for drug molecules to passively diffuse into the CNS. The disruption of BBB varies greatly depends on the pathological conditions. Even in the same pathological condition, such as the brain tumor, the leakage of BBB is not uniform [188]. In addition to BBB, the brain parenchyma as a biological barrier in hindering the drug molecules from reach targeted anatomical location has also drawn many attentions recently [157]. The brain extracellular space (ECS) is a conduit, where many biomolecules forms network, with upper limit of the pore size to be 64 nm, thus, hindering the movement of many molecules [189]. Nanomedicine offers high versatility in their sizes, with nanoparticles sizes ranging from one nm to hundreds nm, and therefore, can potentially address these two barriers if engineered carefully. Investigating the relationship between nanoparticle size and their ability to target CNS disease can help better select and design nanomedicine for the treatment of CNS diseases.

The movement of nanoparticles in the brain parenchyma is also greatly affected by their surface functionalities. Heavily PEGylated nanoparticles with a neutral surface charge tend to have better movement in the brain ECS compared with non-PEGylated charged nanoparticles, mainly due to neutral surface charge minimized adhesive interactions between nanoparticles brain ECS [157]. However, for systemically administrated nanoparticles, the ability to cross the blood-brain barrier also plays a major role in determine their ability to target CNS disease. Therefore, a better understanding of the influence of nanoparticles surface charge on their brain uptake is also needed.

PAMAM dendrimers possess various sizes that can be precisely controlled by tuning their generation, and dense surface functionalities that can be modified or engineered. Therefore, PAMAM dendrimers have been used as drug delivery vehicles for the treatment of many CNS diseases such CP, brain tumor and ischemia [86, 183, 190]. Previous studies on dendrimers size and functionality has been greatly focused on their influence on toxicities. In this study, we used a rat model of GBM, and investigated the influence of dendrimer size on their pharmacokinetics and ability to target brain tumor. We then used a rabbit model of CP to determine how surface functionality of dendrimer affecting their target to neuroinflammation.

## 5.2. Materials and Methods

### *5.2.1. Tumor inoculation*

Female Fischer 344 rats, weighing 125-175 g each (Harlan Bioproducts, Indiana, IN), were housed in standard facilities and given free access to food and water. 9L gliosarcoma intracranial implantation was performed as previously described [25]. Briefly, the 9L gliosarcoma (obtained from the Brain Tumor Research Center, UCSF, San Francisco, CA) maintained in the flank of F344, was surgically excised sectioned into 1 mm3 pieces and placed in sterile 0.9% NaCl

solution on ice for intracranial implantation. Rats were anesthetized and a midline scalp incision was made to identify the sagittal and coronal sutures. A burr hole was made 3 mm lateral to the sagittal suture and 5 mm posterior to the coronal suture. The dura was incised, and using a surgical microscope and gentle suction a small cortical area was resected. A tumor piece was placed in the resection cavity and the skin was closed using surgical staples. All animals were treated in accordance with the policies and guidelines of the Johns Hopkins University Animal Care and Use Committee.

*5.2.2. Rabbit model of maternal inflammation induced cerebral palsy*

All animal procedures were approved by the Institutional Animal Care and Use Committee of Johns Hopkins University, and are as described previously [160, 191, 192]. Briefly, pregnant rabbits in the endotoxin group (n = 10 dams) underwent laparotomy at gestational day 28 (term pregnancy 31 days) and were injected with 1 mL of saline containing Escherichia coli endotoxin (6200 endotoxin units per site) (serotype O127: B8, Sigma Aldrich) along the length of the uterus [160, 192]. At this dose, the newborn kits have been shown to have uniform microglial activation in the PVR and display a phenotype of CP with predominantly hindlimb hypertonia [160, 191, 192]. The healthy control group (n = 6 dams) included pregnant rabbits that had no surgery or intervention. After undergoing laparotomy on G28, dams were given maintenance fluids of 60cc normal saline subcutaneous every 12 hours. On the evening of G30, dams were induced using 10 mEq/kg oxytocin to control timing of delivery, and the newborn rabbits kits were immediately removed and placed in an incubator. All kits were given 1cc normal saline subcutaneous, weighed, and hand-fed fresh frozen rabbit milk every 6-8 hours until time of euthanasia. Kits were then injected with dendrimer on postnatal day 1 of life (corresponding to G31), and kept in an incubator until time of euthanasia.

*5.2.3. Dendrimer administration for quantification and immunofluorescence*

For rat model of GBM, animals were injected in tail vein with a 3 mg/300 μL dendrimer-Cy5 solution. To study the dynamics of dendrimer accumulation in the tumor brain, Cy5-labeled dendrimers were injected into tumor inoculated rats when the average tumor size was 6 mm in diameter and then animals were sacrificed at fixed time points (15 min, 8 h, 24 h, and 48 h). Magnetic resonance imaging was used to measure intracranial tumor size. Blood was drawn through cardiac puncture and immediately centrifuged to collect plasma. Brains were harvested and flash frozen on dry ice for fluorescence spectroscopy based quantification or placed in 4% formalin solution for immunofluorescence.

For rabbit model of CP, animals were systemically injected with 55mg/kg Cy5-labeled dendrimers at Postnatal Day 1 (PND1). Animals were sacrificed at fixed time points (1 h, 4 h, 24 h).

*5.2.4. Fluorescence spectroscopy*

Fluorescence-based quantification of Cy5-labeled dendrimers followed our previously published protocol [95]. Briefly, 100-150 mg of frozen tissue (for rat model of GBM) or ~400 mg of frozen tissue (for rabbit model of CP) were homogenized in 1 mL of methanol using a homogenizer (TissueLyser LT, Giagen) in 2 mL DNA LoBind Eppendorf tubes and subsequently sonicated. Suspensions were diluted to 100 mg/mL and centrifuged at 15,000 rpm for 15 min at 4 °C. The resulting supernatants were subjected to fluorescence spectroscopy. Importantly, prior studies showed that Cy5-labeled dendrimers was stable in plasma, and could be recovered from the tissue intact, without appreciable release of the conjugated Cy5 [95].

For brain tissue, precise dissection of the tumor was performed and the peritumoral area was defined as up to 1 mm away from the tumor dissection plane. In the contralateral hemisphere 100

mg of the caudate/putamen with the surrounding white matter area was dissected and used for analysis. For plasma samples, a sample of 100 µL of plasma and urine was mixed with 900 µL of phosphate buffer (0.1 M) and analyzed by fluorescence spectroscopy.

Fluorescence spectra of D-Cy5 conjugates and that obtained from tissue extracts were recorded using a Shimadzu RF-5301 Spectrofluorophotometer (Kyoto, Japan). Cy5-labeled dendrimers calibration curves were constructed, following every experiment, under different slit widths using the maximum emission wavelength of 662 nm after recording spectra from 650 nm to 720 nm with excitation wavelength of 645 nm. The Cy5-labeled dendrimers concentration was measured in methanol or phosphate buffer (0.1 M) in solutions ranging from 1 ng/mL to 100 µg/mL. The slit width was chosen based on the observed fluorescence level of different sample sets. For biological samples with low levels of Cy5-labeled dendrimers (i.e. brain, lung, heart), the excitation and emission slit width was set at 10; for biological samples with high levels of Cy5-labeled dendrimers, (i.e. urine and kidney) excitation and emission slit width was set at 3. For the remaining biological samples, excitation slit width of 5 and emission slit width of 10 were used. All calibration curves exhibited linearity with $R2 \sim 0.99$. Fluorescence registered from tissue of non Cy5-labeled dendrimers injected healthy and tumor inoculated rats was subtracted from the values observed from samples of Cy5-labeled dendrimers injected tissue in order to account for tissue autofluorescence.

Concentration of Cy5-labeled dendrimers in the brain was expressed in µg per g of tissue. The concentration of Cy5-labeled dendrimers in the other organs was expressed in percentage (%) of injected dose per gram of tissue or % of injected dose per organ. Concentrations of the Cy5-labeled dendrimers conjugate in urine and blood were expressed in % of injected dose per mL or % of injected dose in total amount of urine or plasma. Total plasma concentration was

calculated based on the weight of the animal. The brain and plasma quantification data were analyzed to calculate the AUC and the brain to serum ratio.

*5.2.5. Immunofluorescence*

Freshly harvested tissues were fixed in 4% formalin for 24 hr, followed by a gradient of sucrose solutions before cryosection. Tissues were then sectioned transversely into 30 μm-thick slices using a Leica CM 1905 cryostat. Slices were stained with DAPI (nuclei), rabbit anti-Iba1 antibody for microglia/macrophages, and goat anti-rabbit 595 secondary antibody. Some slices were stained with isolectin for endothelial cell staining. Slices were then imaged using a confocal LSM 710 microscope (Carl Zeiss; Hertfordshire, UK). For each slice of tumor-inoculated brains, images where acquired for the tumor, tumor border and contralateral hemisphere. For control (non-tumor) brains, 1-3 representative images were acquired. Settings were optimized to avoid background fluorescence based on non-injected control rat brains. Laser power, pinhole, gain, offset and digital gain were selected separately for each magnification and kept constant throughout the entire study.

## 5.3. Results

*5.3.1. Increasing the dendrimer size dramatically increased the brain uptake of dendrimers in rat model of GBM.*

To determine the influence of dendrimer sizes on their brain uptake, we used generation 6 PAMAM dendrimer (hydroxyl terminated) and compared their brain pharmacokinetics under three different pathological conditions (brain tumor, neuroinflammation, excitotoxicity) with those of generation 4 PAMAM dendrimer (hydroxyl terminated). In the rat model of GBM, the accumulation of G4 dendrimers follows the order of tumor>peritumor>contralateral hemisphere.

The concentration of G4 dendrimers in the tumor/peritumor peaked at around 8 h post injection, and gradually decreased, at 48 h post injection, the concentration and AUC of G4 dendrimers in the tumor were around 0.7 μg/g, and 36.3 μg/g/h (Figure 5.1A and B). Similar to G4 dendrimer, the accumulation of G6 dendrimers in the tumor bearing brain also demonstrated the order of tumor>peritumor>contralateral hemisphere. Nevertheless, the accumulation of G6 dendrimers in tumor and peritumor displayed an ascending trend during the assessment period, without reaching its accumulation peak. At 48 h, G6 dendrimers concentration in the tumor reached 23.1 μg/g (Figure 5.1A), and the AUC reached 490.8 μg/g/h, which was more than 100 fold higher than G4 dendrimers AUC in the tumor (Figure 5.1B). Moreover, G6 dendrimers showed higher tumor targeting ability than G4 dendrimers at all time points, as indicated by the brain to serum ratio (Figure 5.1C). To study the dynamics of dendrimer accumulation in the tumor brain, dendrimers were injected into tumor inoculated rats when the average tumor size was 6mm in diameter and then animals were sacrificed at different time points.

*5.3.2. Increasing the size of dendrimers elongate their systemic circulation and reduce renal clearance.*

To investigate the mechanism for increased brain uptake for G6 dendrimers, we then compared the biodistribution of G6 dendrimers and G4 dendrimers in serum, major organs such as kidney, liver and spleen. We found G6 dendrimers showed higher serum concentration and prolonged serum half-life than G4 dendrimers. At 48 h post injection, the serum concentration of G6 dendrimer (~22% ID/mL) is 17-fold higher than G4 dendrimer (~1.3% ID/mL) (Figure 5.2A). Further study of dendrimers distribution in kidney, liver, and spleen revealed that the prolonged systemic circulation for G6 dendrimer wer associated with the reduced renal clearance for G6 dendrimer (Figure 5.2B). For G4 dendrimer, the dendrimer accumulation in kidney

increased overtime, reaching ~30 %ID/g at 48 h post injection. However, the accumulation of G6 dendrimers started to decrease after 24 h, and the accumulation was significantly lower than G4 dendrimers (~40-fold less at 48 h post injection). The liver accumulation of G6 dendrimers was similar to G4 dendrimers at different time points (varied between 0.2% ID/g - 0.5% ID/g), while G6 dendrimers showed similar spleen and liver accumulation, however, this accumulation was 3 - 5 fold higher than G4 dendrimer accumulation in spleen, possibly due to the increased uptake by macrophages in the spleen.

*5.3.3. Increasing the size of dendrimers elongate their systemic circulation and reduce renal clearance.*

Next, we sought to determine whether G6 dendrimers preserved the homogeneous distribution and targeting to the TAMs in the tumor as G4 dendrimers. In the zoomed out confocal images (Figure 5.3A), we found G6 dendrimers had slower excretion rate than G6 dendrimers. For G4 dendrimer, excretion from the blood vessel to tumor tissue started immediately (~15min) after i.v. injection, followed with homogeneously distribution in the whole tumor and peritumor region. At 24 hours post injection, G4 dendrimers were cleared out from the tumor extracellular space, and only retained in the TAMs (Figure 5.3B). For G6 dendrimers, the presence of dendrimers in the tumor tissue was not observed immediately after administration. The concentration of G6 dendrimers gradually increased in the whole observation period, while also maintained the homogeneous distribution throughout the whole tumor and peritumor region. At 48 hours post administration, G6 dendrimers showed highest concentration in the tumor and peritumor area, which is inconsistent with the earlier quantitative study (Figure 5.3A).

Dendrimers ability to target TAMs was also preserved, given the size increase. For G4 dendrimers, the TAMs uptake happened immediately (~15min) after i.v. injection, while G6 dendrimers were not presented at this time point, probably due to their slower excretion rate. At 8 hours, G4 dendrimers not only presented in TAMs but also scattered within the tumor parenchyma, which gradually cleared out at 24 hours. G6 dendrimers were mostly taken up by TAMs at 8 hours, but the accumulation in the tumor parenchyma also kept on increasing till 24 hours. At 48 hours post injection, both G4 and G6 dendrimers were mostly retained in the cells.

*5.3.4. Dendrimers uptake as a function of surface functionality*

In addition to the sizes, we also investigated the dendrimers uptake as a function of dendrimers surface functionality. Specifically, we studied the brain uptake of G4-OH (neutral), G4-COOH (anionic), and G4-$NH_2$ (cationic) in the rabbit model of CP (Figure 5.4). These three dendrimers have approximately the same size and molecular weight, but different surface functionalities and zeta potentials at physiological pH (Table 2). We measured total amount of dendrimer in the brain (μg) over the total amount of brain tissue analyzed (g tissue). In general, all dendrimers demonstrated higher uptake in the brain of CP kits than those of healthy control kits (>10-fold overall uptake in the brain of CP kits). We showed the peak accumulation for all dendrimers appeared at 4 hours post injection, following with a decrease in total amount in the brain by 24h. G4-NH2 demonstrated the highest brain uptake of all dendrimer kinds, and had a 3-fold higher concentration than other dendrimers. G4-OH and G4-COOH had similar amounts in the brain at all time-points.

## 5.4. Discussion

The tumor uptake of nanoparticles is governed by the nanoparticles ability to circulation in the blood and their ability to extravasate from the leaky blood vessels and to diffuse in the tumor

parenchyma [193]. Many inflammatory diseases share the similar requirements [194]. The size of nanoparticles plays a pivotal role in determining these abilities. Nanoparticles need to be large enough to achieve enough circulation time to provide exposure to the foci, but also need to be small enough so that it can cross the leaky blood vessel, diffuse in in the tissue and eventually target the pathology. Due to the existence of BBB, CNS diseases usually have higher requirements on the size of nanoparticles. Passive diffusion through the leaky BBTB fenestrations has only been demonstrated with molecules smaller than 20 nm [79, 80, 81, 82] and unhindered diffusion through the BBTB has been achieved with molecules of 7 nm. In this study, the small increase of diameter (from 4.3 nm to 6.7 nm, Table 1) lightly delayed the extravasation time of dendrimer into the brain tumor, but did not sacrifice the ability of dendrimers to homogenously distribute throughout the whole tumor, and target TAMs. Previous study predicted the cutoff size of renal clearance for hydroxyl terminated PAMAM dendrimers to be 6 nm [195], slightly smaller than the hydrodynamic diameter of G6 dendrimer. Therefore, we observed a significant reduction (40-fold) on the kidney accumulation when using G6 dendrimers. However, the reticuloendothelial system was not activated by this small increase in size. Therefore, we did not see a dramatic increase in liver and spleen uptake. As a result, we observed prolonged systemic circulation in G6 dendrimers.

In addition to the rat model of GBM, we also observed the increased uptake at the pathological region in the brain among rabbit model of CP and canine model of hypothermic circulatory arrest (HCA) (data not shown).

We also observed the surface functionality can greatly affect the brain uptake of dendrimers. Cationic dendrimers G4-$NH_2$ showed highest brain uptake and accumulation. However, following studies on the brain distribution of G4-$NH_2$ showed most of them were attached to the

BBB, and were not presented in the brain parenchyma or pathological cells (data not shown). In addition, cationic PAMAM dendrimers was also found to be toxic to the CNS in many studies. A single intranasal dose of G4-$NH_2$ (3 or 15 μg/mouse) can cause alterations of genes expression related to the normal brain [196]. *In vitro* study also showed microgram level of G5-$NH_2$ can induce autophagy due to increased intracellular reactive oxygen species generation [197].

## 5.5. Conclusion

In this study, we used rat model of GBM and rabbit model of CP to study the influence of size and surface functionality on dendrimers ability to target CNS diseases. We have demonstrated (1) slightly increase the dendrimer generation from G4 to G6 (~2.4 nm increase in hydrodynamic diameter) significantly increased the brain uptake of dendrimer in the tumor bearing brain, and changed their biodistribution (longer systemic circulation, lower kidney uptake), yet this pharmacokinetic improvement did not sacrifice dendrimers ability of homogenously distribute in the brain tumor, or target TAMs. (2) Surface functionality influence the dendrimer uptake in the brain of CP kits, with G4-NH2 showed ~3-fold higher uptake in the brain than G4-OH and G4-COOH.

**Table 5.51. Characterization of molecular weight, terminal functional groups, size and ζ-potential of G4 and G6 PAMAM dendrimers.**

| Generation | Mw | Terminal function groups | Hydrodynamic Diameter (number average) | ζ-potential |
|---|---|---|---|---|
| **G4** | 14279 Da | 64 | 4.3 ± 0.2 nm | 4.5 ± 0.1 mV |
| **G6** | 58304 Da | 256 | 6.7 ± 0.6 nm | 0.25 ± 0.4 mV |

**Table 5.52. Physical properties of G4 PAMAM dendrimer with different surface functionality.**

| Platform | Physiological pH | MW (kDa) | Size ± SEM (nm) | Zetapotential ± SEM (mV) |
|---|---|---|---|---|
| G4-OH | Neutral | 14.1 | 4.3 ± 0.2 | +4.5 ± 0.1 |
| G4-$NH_2$ | Cationic | 14.1 | 3.9 ± 0.3 | +19.5 ± 0.1 |
| G4-COOH | Anionic | 11.1 | 3.2 ± 0.4 | -12.2 ± 0.2 |

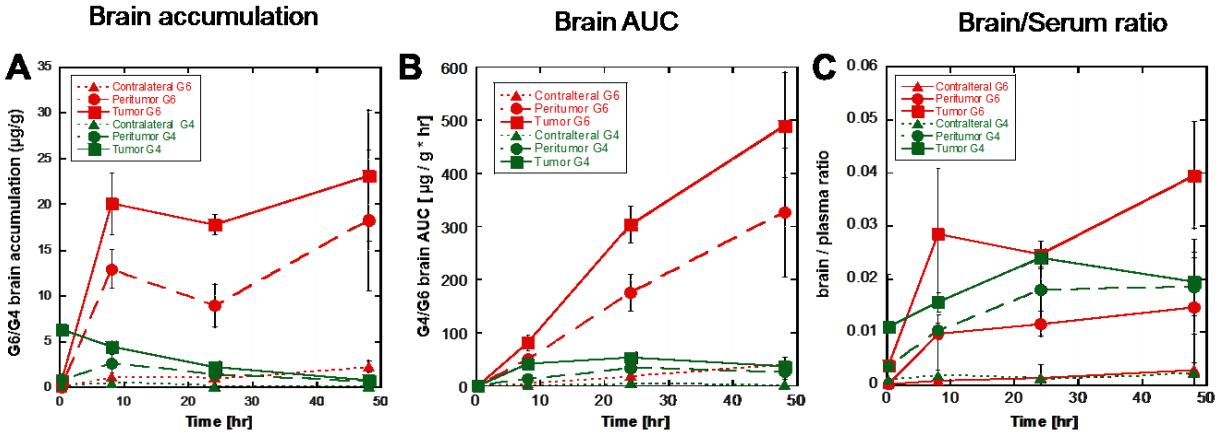


**Figure 5.51. Pharmacokinetics of G6 and G4 dendrimers in the tumor bearing brain.**

(A) The compare of accumulation (μg of dendrimer / g of brain tissue) between G6 and G4 dendrimers in a tumor bearing brain as a function of time. The accumulation of G4 dendrimers in the tumor/peritumor peaked around 8 hours post injection, and gradually decreased, while G6 dendrimers concentration in tumor/peritumor continuously increased. (B) The area under curve (AUC) plot also demonstrated G6 dendrimers had around 100-fold higher brain tumor exposure than G6 dendrimers within 48 hours; (C) G6 dendrimers showed higher brain to serum ratio, indicating better tumor-targeting ability than G4 dendrimers.

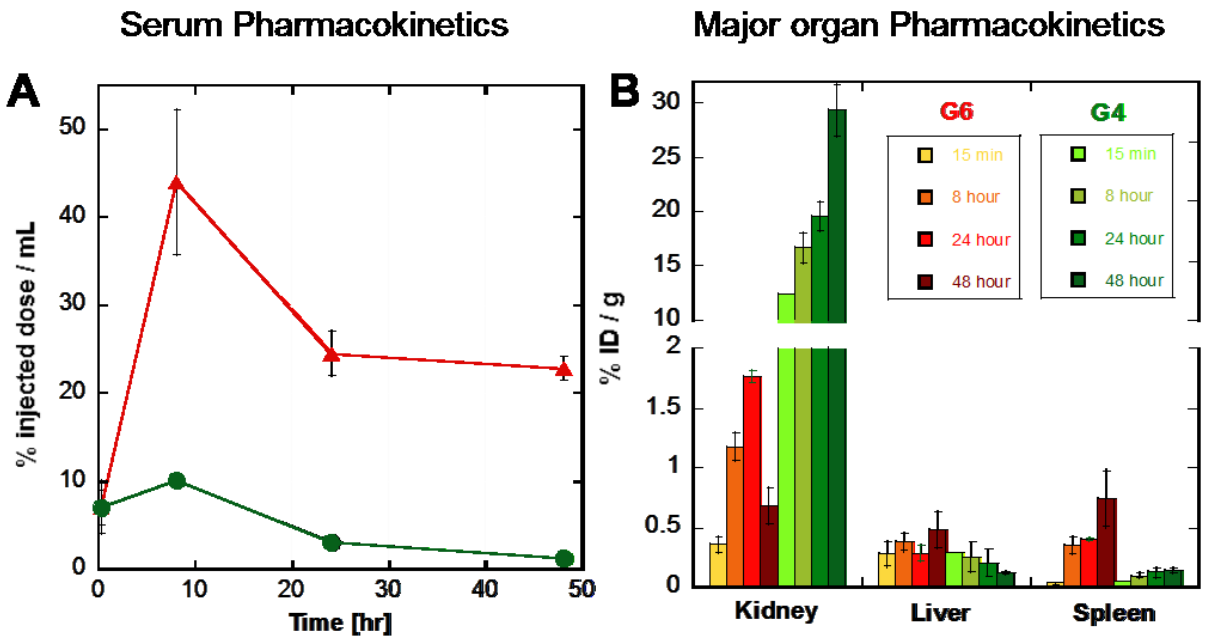


**Figure 5.52. The G4 (green) and G6 (red) dendrimers concentration in serum and major organs: kidney, liver, spleen as a function of time.**

(A) G6 dendrimers showed higher serum concentration and prolonged serum half-life than G4 dendrimers, which contributed to the higher tumor accumulation and targeting of G6 dendrimers. The dendrimer concentration was demonstrated as percentage of total injected dose per milliliter of serum; (B) For G4 dendrimers, kidney had most dendrimer accumulation (20%-30%), significantly higher than dendrimer accumulation in liver and spleen (~0.3%) at different time points. For G6 dendrimers, the increase of size greatly decreased the renal filtration (as seen in (A)) and kidney accumulation. The kidney concentration of G6 dendrimers was much less than G4 dendrimers, and started to showed the evidence of clearance from kidney starting from 48 hours. The liver accumulation of G6 dendrimers was similar to G4 dendrimers, while spleen showed ~5-fold higher accumulation, possibly due to the increased uptake by macrophages.

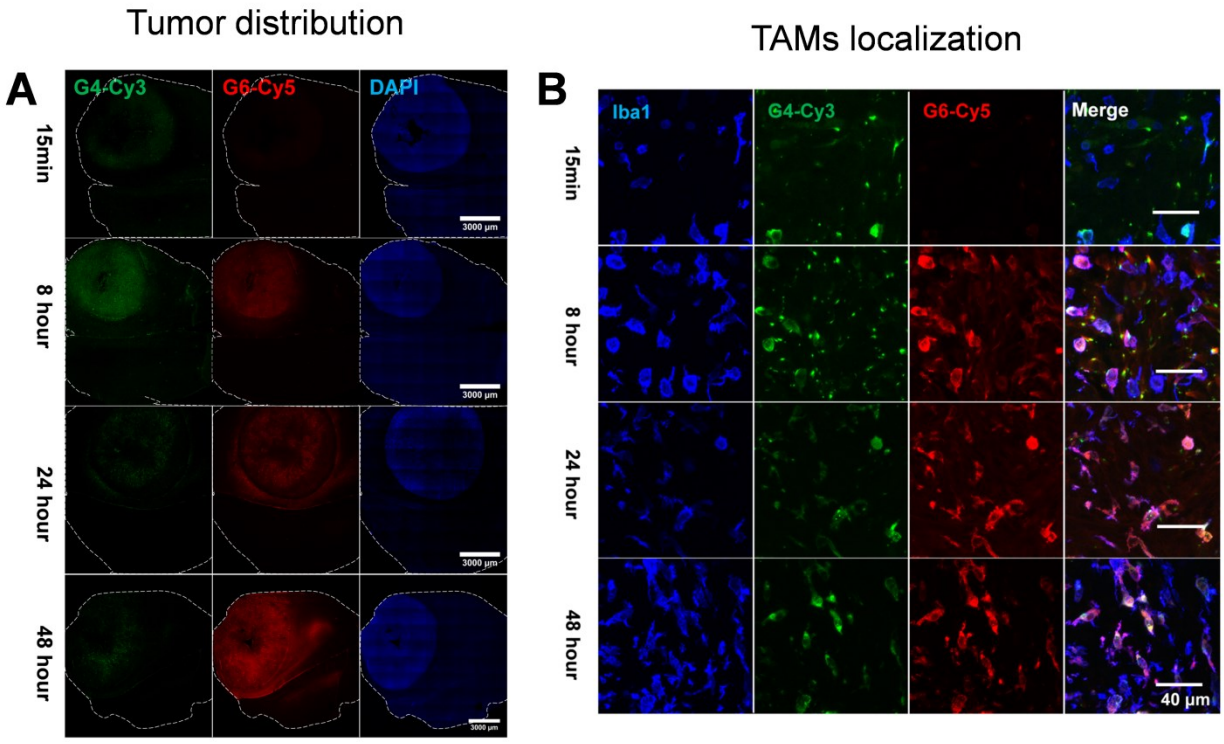


**Figure 5.53. The distribution of G4 and G6 dendrimers in the tumor bearing brain as a function of time.**

G4 dendrimers had a faster excretion rate than G6 dendrimers. For G4 dendrimer, excretion from the blood vessel to tumor tissue started immediately (~15 min) after i.v. injection, followed with clearance from tumor after 8 hours. After 24 h post injection, G4 dendrimers were retained in the cells. For G6 dendrimers, the presence of dendrimers in the tumor tissue was not observed immediately after administration. The concentration of G6 dendrimers gradually increased in the whole observation period. At 48 hours post administration, G6 dendrimers showed highest concentration in the tumor and peritumor area. Nuclei was stained by 4',6-diamidino-2-phenylindole (DAPI) (Blue in nuclei panel). Scale bar 3000 μm. The dash line stands for the outline of axial sectioned brain.

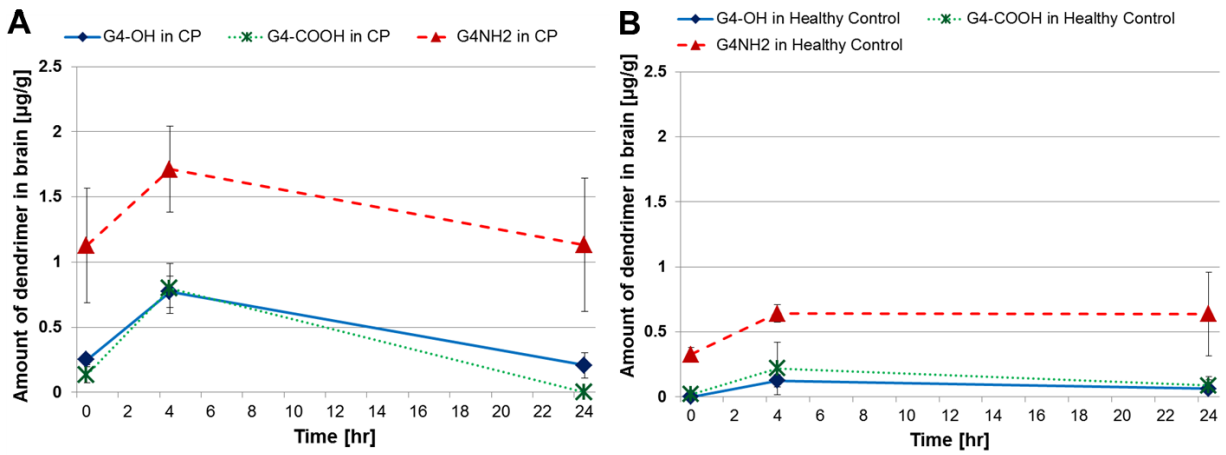


**Figure 5.5.4. The accumulation of dendrimers in the brain of CP rabbit as a function of surface functionality.**

All dendrimers demonstrated higher uptake in the brain of CP kits than those of healthy control kits (>10-fold overall uptake in the brain of CP kits). We showed the peak accumulation for all dendrimers appeared at 4 hours post injection, following with a decrease in total amount in the brain by 24h. G4-NH2 demonstrated the highest brain uptake of all dendrimer kinds, and had a 3-fold higher concentration than other dendrimers. G4-OH and G4-COOH had similar amounts in the brain at all time-points.

# 6. DENDRIMER DELIVERY IMPROVE THE EFFICACY OF GCPII INHIBITOR AGAINST EXCITOTOXICITY AND ATTENUATE NEUROINFLAMMATION

## 6.1. Introduction

Excitotoxicity and neuroinflammation are usually considered as the common hall marks of many neurodegeneration disorders [198]. Recent studies have shown mechanistic evidences that excitotoxicity and neuroinflammation could be linked to each other through the alterations in the glial function in many neuroglial disorders [198]. In neuroinflammation, the activated glial cells release inflammatory mediators, and increase oxidative and nitrosative stress, which could compromise neuronal survival, and may lead to neuronal dysfunction and degeneration [199]. Glutamate excitotoxicity (usually refers to the injury and death of neurons arising from prolonged exposure to extracellular glutamate), has been gaining acceptance as a pivotal player in neurodegenerative disease [200]. Growing evidences also showed the mechanism between the disruption of glutamate regulation and glial activation [201]. Moreover, effects of neuroinflammation such as generation of free radicals, mitochondrial dysfunction can directly lead to secondary excitotoxicity [198, 200], indicating the central role of excitotoxicity in neurodegeneration disorders.

Human glutamate carboxypeptidase II (GCPII) (EC 3.4.17.21) is implicated in diverse pathologies. GCPII cleave N-acetylaspartylglutamate (NAAG) into N-acetylaspartate (NAA) and glutamate. NAAG is an abundant peptide in the brain and functions as a selective agonist at metabotropic glutamate receptor subtype 3 (mGluR3), which is located on both neurons and astrocytes. NAAG could play a significant role in modulating glutamate excitotoxicity. The

inhibition of GCPII will decrease the cleavage of NAAG into NAA and glutamate, which diminish the secondary source of synaptic glutamate. The increased NAAG can reduce excessive glutamate release by activation of presynaptic mGluR3 autoreceptors. The activation of mGluR3 on astrocytes increases the expression of glutamate transporters, which facilitate the clearance of excess glutamate from the synapse. Moreover, decreased NAA can reduce NAA-Na+ co-transport and subsequent astrocyte Na+ overload and astrocyte pathology. Thus, inhibition of GCPII represents a novel strategy for reducing glutamate excitotoxicity.

The pharmacological inhibition of GCPII activity has exhibited beneficial effects in various neurological disorders including stroke, amyotrophic lateral sclerosis, inflammatory and neuropathic pain, and traumatic brain injury [202, 203, 204]. Small-molecule ligands targeting GCPII are used in diagnostic and treatment in prostate cancer (PCa) and various neurological disorders [205, 206]. 2-(3-mercaptopropyl) pentanedioic acid (2-MPPA) is the first GCPII inhibitor subjected to clinical patient trials. However, no additional studies were carried out because of the relatively low potency of 2-MPPA (estimated human therapeutic dose of ~750 mgs) together with concerns over potential immune reactivity common to thiol containing drugs [205]. Therefore, the development of novel GCPII-specific ligands attracts more attention from both academia and industry.

Nanotechnology is emerging as a promising approach for the treatment of glutamate mediated excitotoxicity. Fullerenol (water-soluble derivatives of fullerenes) by itself served as ROS scavenger [207, 208] and glutamate receptor antagonist [209], therefore, exerted neuroprotective effects against glutamate mediated excitotoxicity. When loaded with estradiol, poly(lactic-co-glycolic acid) (PLGA) nanoparticles was found to be more effective than free estradiol in reducing glutamate-induced excitotoxic neuronal death [210].

Recently, polyamidoamine (PAMAM) dendrimers-based therapies have been applied in the treatment of diseases involving excitotoxicity and neuroinflammation [84, 156, 190]. The small sizes, high density of surface functional groups, and flexible architecture made PAMAM dendrimers extremely useful for delivering drugs to the CNS [59, 211, 212]. More importantly, the intrinsic property of targeting to the pathological cells under different pathological condition made PAMAM dendrimers more desirable tools for CNS drug delivery. In a canine model of hypothermic circulatory arrest (HCA), G4-OH was found to selectively localize in the injured neurons. When conjugated with valproic acid (VPA) and n-acetylcysteine (NAC), this combination therapy successfully addressed the CNS excitotoxicity and improved the neurological deficit score improvements [84] at a 10-fold (compared with VPA) and 30-fold (compared with NAC) lower dose. In a mice model of ischemia, dendrimer predominately localized in the astrocytes at the initial stage of ischemia induced injury, and subsequently shifted to the microglia when the injury progressed to later stage [190].

In the same cerebral palsy model, we have previously shown D-NAC therapy reduce neuronal death and neurodegeneration through attenuating neuroinflammation, specifically by targeting activated microglia and astrocytes, and reducing the oxidative stress in the CNS [86]. Since reducing glutamate mediated excitotoxicity provided a more direct pathway in mitigating neurodegeneration and neuronal death, we hypnotize that using GCPII inhibitor to address excitotoxicity in the rabbit model of CP can benefit the disease outcome. In this study, we conjugated a GCPII inhibitor to PAMAM dendrimer, and evaluated the conjugates ability to inhibit glutamate excitotoxicity and to attenuate neuroinflammation.

## 6.2. Materials and Methods

### *6.2.1. Materials and reagents*

G4-OH was purchased from Dendritech (MI, USA); Sephadex G25, Cy5 NHS ester were purchased from GE Healthcare (Little Chalfont, United Kingdom); PyBOP, DIEA, Fmoc-glycine, 2MPPA, DMF, Piperidine, SPDP, TEA, Cyanine 5 (Cy5) NHS Ester, glutathione (GSH) were purchased from Sigma-Aldrich (MO, USA); dialysis membrane (2 kDa) was purchased from Spectrum Labs (CA, USA).

### *6.2.2. Synthesis of Bifunctional PAMAM G4-OH dendrimer having Fmoc-protected amine (Intermediate 1)*

The Fmoc-Gly-OH (142.0mg, 0.42mmole) was dissolved into DMF (5mL), PyBOP (327.0mg, 0.63mmole) in DMF (5mL) and DIEA (81.4mg, 0.63mmole) in DMF (5mL) were added under N2 atmosphere. The reaction mixture was stirred for 45min under room temperature. Then, PAMAM G4-OH (200mg, 0.014mmole) was dissolved in DMF (5mL) and added. The reaction mixture was stirred for 24hrs under room temperature. Additional PyBOP (115.0mg, 0.315mmole) and DIEA (42.0mg, 0.315mmole) in DMF (5mL) were added and this reaction mixture was kept on stirring for another 12hrs. The crude product was collected and dialyzed against DMF for 24hrs (membrane MW cutoff 1000 Da). Then mixture was evaporated in reduced pressure and subjected to high vacuum overnight to get the white floppy semi-solid. The semi-solid was then reconstituted with water and lyophilized for 24hrs to get white powder form products.

*6.2.3. Deprotection of Fmoc group (Intermediate 2a)*

The intermediate 1 (250 mg, 0.0149 mmol) was dissolved in anhydrous DMF (10 mL), and piperidine/DMF mix solution was added under nitrogen atmosphere to make a mixture of piperidine/DMF of 2:8. The reaction mixture was stirred for 30min at room temperature, and all piperidine/DMF mixture was evaporated under reduced pressure at 30oC. The crude product was dissolved in 15mL DMF and subjected to dialysis with DMF (membrane MW cutoff 1000 Da) for 8hrs. The solvent was evaporated under reduced pressure and subjected to high vacuum overnight, resulting in a white floppy material 2 (205mg, 91% yield). According to NMR, intermediate 2 has 13 free amine group.

*6.2.4. Synthesis of Cyanine5 (Cy5) NHS ester labeled bifunctional dendrimer (Intermediate 2b)*

The intermediate 2a (200mg, 0.013504mmole) was dissolved in bicarbonate buffer (pH=9.1) under ice bath and stirred for 10min to allow temperature to decrease, Cy5 NHS (12.7mg, 0.016035mmole) was dissolved in DMSO (1mL) and added dropwise into bifunctional dendrimer solution to allow Cy5 NHS ester to react with the surface amine on bifunctional dendrimer for overnight. The reaction mixture was dialyzed against deionized water for overnight and was further purified by Sephadex G25 column to remove unreacted Cy5 NHS ester, resulting in intermediate 2b.

*6.2.5. Synthesis of SPDP modified bifunctional dendrimer (Intermediate 3)*

The intermediate 2a or 2b (200mg, 0.013504mmole) was reacted with the heterobifunctional cross-linker N-succinimidyl-3-(2-pyridyldithio)-propionate (SPDP) (84.375mg, 0.27009) under nitrogen atmosphere protection in 20mL DMF and 47μL TEA for overnight. Extensive dialysis was conducted to remove the excess SPDP and byproducts to yield intermediate 3.

### *6.2.6. Synthesis of G4-OH PAMAM dendrimer-2MPPA conjugates (D-MPPA)*

To synthesis D-MPPA, intermediate 3 (200mg, 0.013504mmole) was reacted with 2-MPPA (57mg, 0.2763mmole) under nitrogen atmosphere protection in 20mL DMSO for 6 hours, following with dialysis against DMF for 24 hours with changing of dialysis solvent every 8 hours to remove excess 2MPPA and byproducts. NMR chromatogram shows around 9 molecules of 2-MPPA were conjugated per 1 dendrimer.

### *6.2.7. Preparation of Dendrimer-2MPPA and Dendrimer-2MPPA-Cy5 conjugates*

The synthetic strategies for D-2MPPA were aimed to conjugate 2MPPA to G4-OH with a linker that can induce triggered release. The molecular structure of 2MPPA possesses three functional groups: two hydroxyl groups and a thiol group. Disulfide bond has been engaged in many bio-conjugation designs. It has demonstrated stability during circulation and other extracellular environment, yet, enabled glutathione (GSH) triggered intracellular release through thiol-disulfide exchange reaction [213, 214]. We chose the thiol group from 2MPPA molecule as the conjugation site, and aiming to conjugate 2MPPA to G4-OH through a disulfide bond. Toward this goal, we designed a 4-step synthesis scheme (Figure 7.1A-B). In the first three steps, the terminal hydroxyl groups of G4-OH were partially modified into a protected thiol groups, for the later formation of disulfide bonds with the thiol groups on 2MPPA molecules. In detail, Fmoc-glycine was conjugated to the surface of G4-OH in the presence of a catalytic amount of coupling reagent PyBOP and DIEA, to form intermediate 1. The Fmoc groups were then deprotected in the piperidine/DMF mix solution (piperidine/DMF = 2/8) under 0˚C for 30 min to form the amine-modified bifunctional dendrimer: intermediate 2a. We noticed some conjugated Fmoc-glycine were lost in the deprotection step due to the presence of piperidine. This led to around 13 surface amines on intermediate 2a. In the next step, the terminal amines of

intermediate 2a were further modified into protected thiol groups (intermediate 3a) by reacting with SPDP for 6 hours in the presence of TEA. In the last step, excess 2MPPA was added into the reaction mixture of intermediate 3a in situ. Reaction was allowed to go for 24 hours at room temperature. The final conjugates D-2MPPA were purified through dialysis against DMF (membrane MW cutoff 2000 Da), followed with lyophilization to form brown colored powder.

In order to study the brain distribution of D-2MPPA, we also prepared Cy5 labeled D-2MPPA (D-2MPPA-Cy5). To make sure the introduction of Cy5 molecule does not change the biodistribution of D-2MPPA, we limited the feeding ratio of Cy5 so that only one Cy5 was labeled per D-2MPPA molecule. The procedures for D-2MPPA-Cy5 preparation were based on the synthesis scheme of D-2MPPA, and were demonstrated in Figure 7.1C. In brief, amine terminated bifunctional dendrimer (intermediate 2a) was labeled with one Cy5-NHS molecule in the presence of excess TEA for 12 hours to generate intermediate 2b. The unreacted amines on intermediate 2b were further modified based on the D-2MPPA synthesis scheme to generate the final conjugate D-2MPPA-Cy5, following with purification through dialysis against DMF (membrane MW cutoff 2000 Da) and Size Exclusion Chromatography (SEC) using Sephadex G-25 column. All other conjugates were purified through dialysis against DMF (membrane MW cutoff 2000 Da). The intermediate compounds were characterized with 1H-NMR for their chemical structure and payload.

*6.2.8. HPLC analysis of D-MPPA conjugates*

The free 2-MPPA and purified dendrimer D-MPPA conjugate was analyzed using Waters HPLC instrument equipped with binary pump, photodiode array (PDI) detector, and auto sampler interfaced with Empower software. The HPLC chromatogram was monitored at 210 and 205 nm simultaneously using PDI detector. The H2O/acetonitrile (ACN) (0.1% w/w TFA) was freshly

prepared, filtered, degassed, and used as a mobile phase. Tosho TSK gel reverse phase column with 5μm particle size, 25cm length, and 4.6 mm internal diameter was used. A gradient flow was used with initial condition of 90:10 (H2O/ACN) and gradually increasing the gradient condition of 30:70 (H2O/ACN) till 15min to 50:50 (H2O/ACN) in 30 min and returning to 90:10 (H2O/ACN) in 40 min with flow rate of 1 mL/min.

*6.2.9. In vitro toxicity study*

The toxicity of D-2MPPA conjugate was evaluated on murine microglial cells (BV-2) passage 19, using MTT cell proliferation assay kit (Molecular probes, Invitrogen, Oregon, USA). The toxicity of D-2MPPA was expressed as percentage of cell viability, and was compared with G4-OH, which is considered to have low toxicity; and G4-NH2, which is considered to have higher toxicity [215]. BV-2 cells were plated in 96 well plates at a concentration of 1.0 × 104 / well. Cells were incubated in Dulbecco's modified Eagle's medium (DMEM, Life technologies, Grand Island, NY) supplemented with 5% heat in activated fetal bovine serum (Hi-FBS, Invitrogen Corp., Carlsbad, CA) and 1% antibiotics (penicillin/streptomycin) (Invitrogen Corp., Carlsbad, CA). After 24 h incubation at 37 °C, cells were treated with D-2MPPA, G4-OH and G4-NH2 at concentration ranging from 0.01 μg/mL to 100 μg/mL for 24 h before assessment.

*6.2.10. Release study of D-MPPA conjugates under intracellular level glutathione (GSH)*

D-MPPA conjugates (9 mg) were dissolved in 6 mL PBS buffer to form a solution of 1.5 mg/mL D-MPPA. 17.21 mg or 3.5 μg glutathione (GSH) were added into this solution to mimic the intracellular (10 mM) or extracellular GSH level, and to initiate the release of 2-MPPA. Another release study was done under 1× PBS solution with no GSH exposure. Samples were incubated under 37oC and 5% of CO2 and 400μL of solution collected at different time points (0min, 15min, 30 min, 45 min, 60 min, 2 h, 3 h, 4 h, 6 h, 8 h, 12 h, day1, day2, day3 and day4),

and immediately analyzed with RP-HPLC. For each time points, triplicate samples were measured. The release amount of free 2-MPPA was calculated by integrating the area under peak correspondent to free 2-MPPA in the HPLC chromatogram of collected sample, and fit this number with a calibration curve of free 2-MPPA.

*6.2.11. Primary glia cell extraction and culture*

Cerebral cortices from 1-3 day old New Zealand white rabbits were excised, meninges removed, and cortices were suspended in 5mL of 0.05% trypsin for 15min. DMEM media with 10% FBS and 1% penicillin and streptomycin (Corning Cellgro, Manassas, VA USA) was added to stop the trypsin reaction and the cortices were minced and triturated into small pieces to separate the cells. To remove debris, the cell suspension was filtered through a 70μm cell strainer, followed centrifugation at 1000 rpm for 5 min under 4° C. The pellet was re-suspended in DMEM media containing 4.5 g glucose, 1.4 mM L-glutamine (Corning Cellgro, Manassas, VA USA), 10% FBS and 1% penicillin and streptomycin. To culture the primary glia cells, cells were plated into 175 mL culture flask (Sigma Aldrich, St Louis, MO USA) and incubated at 37 ° C and 5% CO2 atmosphere. Media was changed every two days and cells were allowed to reach 90% confluence (day 9-13).

*6.2.12. Cell treatment and imaging*

To image the binding of D-MPPA to the GCPII receptor on the cell membrane, we reseeded glial cells onto 35mm glass bottom culture dish, allowed cells to reach confluence. Cells were then treated with 15μg/mL of D-MPPA-Cy5 and 15μg/mL of D-Cy5, followed with fixation at 1hr, 3 hr and 8hr post dendrimer treatment, with n=3 for each time point. To fix the cells, cells were incubated in 4% formalin solution (4oC) for 15min, then processed with 50:50 acetone/ethanol solution for 1 min to permeablize the cells. Fixed cells were store at 4oC before

imaging. For imaging study. Fixed cells were then incubation with Anti-GFAP (XXX) (1:500) for 48 h, followed by 5min incubation in DAPI solution (1:1000). Finally, cells were imaged under LSM710 Confocal microscope (Carl Zeiss, Hertfordshire, UK).

Brain slices were prepared based on modifications to previously published protocols [171]. In brief, rabbit brain slices were prepared form PND1 rabbit kits with CP. To prepare the brain slices, euthanized rabbit kits were decapitated under aseptic conditions. The brain was removed, dissected into two hemispheres and sectioned in a coronal direction immediately into 350 μm brain slices using Mcllwain tissue chopper (TED PELLA, Inc., USA). For each hemisphere, 6 consecutive slices at the level of the bregma were carefully separated in the dissection medium (3.2g Glucose/500ml HBSS, 1% of penicillin), while maintaining the intact. After separation, each brain slice was transferred onto a low-protein-binding membrane inserts (Millicell-CM, Millipore) which is fitting in 6-well tissue culture plates. 1 mL of dissection medium was prefilled into the well so that membrane is just in contact with the medium, but not submerged by the medium. All the brain slices were maintained overnight at 37 °C in a humidified atmosphere with 5% CO2 before therapeutic treatment.

To treat the brain slice with therapeutics, the dissection medium was first replaced with artificial cerebrospinal fluid (ACSF), 100 μL stock solution of PBS or 2MPPA or D-2MPPA in 1X sterile PBS was then applied directly on top of the brain slices to allow all the therapeutics gradually diffusing throughout the brain tissue. To evaluate the treatment efficacy, the treatment was terminated at 6 hours (short term) or 24 hours (long term) post incubation (Figure 7.3A). The culture medium and the brain slices were collected separately. All samples were stored in -80˚C before evaluation.

The glutamate concentration in liquid and tissue samples were assessed using glutamate assay kit (Abcam ab83389). Sample preparation and measurement followed the assay protocol. To avoid the variations caused by the different extent of injury from each CP kits, we chose an internal control from each rabbit kit, i.e. brain tissue that only received 6 hours of PBS treatment, and normalized the other samples from the same kits by the internal control. In this way, the measured of glutamate levels were normalized number and do not have a unit. The variation of glutamate inhibition within the same group was due to the variation of reaction of each slice to the same treatment.

*6.2.13. Animal CP model*

Time pregnant New Zealand white rabbits were ordered from Robinson Services Inc. (North Carolina, U.S.A.) and arrived at the facility one week before surgery. All animals were housed under ambient conditions (22°C, 50% relative humidity, and a 12-h light/dark cycle), and necessary precautions were undertaken throughout the study to minimize pain and stress associated with the experimental treatments. Experimental procedures were approved by the Johns Hopkins University Animal Care and Use Committee (IACUC). After one week of acclimation, the pregnant rabbits underwent laparotomy at gestational day 28 (G-28) and received a total of 3,200-6000 EU of LPS (E. coli serotype O127:B8, Sigma Aldrich, St Louis MO) injection along the wall of the uterus as previously described [156, 192]. The control group did not receive any intervention. The kits from the control and CP groups were born spontaneously on G31 (full term) and kept in incubators with the temperature of ~32-35°C and relative humidity of ~60-70%.

*6.2.14. Neurobehavior*

Neurobehavioral tests were carried out on PND1 before drug administration by personnel blinded to the experiments. Each animal was videotaped for 10 min and scored on a scale of 0–3 (0, worst; 3, best) for movements of head and limbs on a flat surface as previously described for rabbits [216, 217]. The kits were fed with rabbit milk and the suck/swallow and head turn during feeding were assessed on a scale of 0–3 (worst-best) [216]. The muscle tone of each limb was scaled at 0-4 (0, limb rigid in flexion or extension; 4, no increase in tone). The composite score was scaled at 0-28 (0, most severe; 28, healthiest).

*6.2.15. Immunohistochemistry*

To evaluate the microglia morphology, the rabbits were anesthetized and transcardially perfused with PBS, followed by 4% paraformaldehyde (PFA) in PBS. The brains were removed and post-fixed in 4% PFA overnight and cryoprotected in graded sucrose solutions. Coronal sections (30 μm, 1:6 series) were incubated in 0.3% hydrogen peroxide (H2O2) solution, blocked by 3% normal donkey serum in 0.1 M phosphate-buffered saline (PBS). Sections were then incubated overnight at 4°C with goat andti-IBA1 (1:500, abcam, MA. U.S.A.) Sections were subsequently washed and incubated with biotinylated secondary antibodies (1:250; Vector Laboratories, Burlingame, CA) for 4 h at room temperature. Next, the sections were incubated for 2 h in avidin–biotin substrate (ABC kit, Vector Laboratories, Burlingame, CA). All sections were then incubated for 2 min in 3,3'-diaminobenzidine (DAB) solution (Vector Laboratories). Sections were dehydrated in ethanol and Histo-ClearTM II (Fisher Scientific, Pittsburg, PA, U.S.A.), and cover-slipped using mounting medium. To evaluate the co-localization of D-2MPPA-cy5, GCPII and astrocytes or microglia, the sections were incubated overnight at 4°C with chicken anti-GFAP (1:250, abcam, MA. U.S.A.)/mouse anti-GCPII (1:200, GeneTex, CA,

U.S.A.), or goat anti-IBA1 (1:250, abcam, MA. U.S.A.)/mouse anti-GCPII (1:200, GeneTex, CA, U.S.A.). Sections were subsequently washed and incubated with fluorescent secondary antibodies (1:250; Life Technologies, MA, U.S.A.) for 2 h at room temperature. Next, the sections were incubated with DAPI (1:1000, Invitrogen) for 15 min. After wash, the slides were dried and cover slipped with mountain medium (Dako, Carpinteria, CA, USA). Confocal images were acquired with Zeiss ZEN LSM 710 (Zeiss, CA, U.S.A.) and processed with ZEN software.

*6.2.16. Pharmacokinetics (PK) study of 2MPPA/D-2MPPA*

The CP kits from the same litter were randomly divided free 2-MPPA and D-2MPPA groups. Animals received intravenous (i.v.) administration of free 2-MPPA (20 mg/kg, 200 µl) or D-MPPA (containing 20 mg/kg 2-MPPA, 200 µL) on postnatal day 1 (PND1), and sacrificed at 1, 3, 24 and 48 h post-injection and perfused with PBS. The plasma and the periventricular regions (PVR), including part of the corpus callosum, corona radiata, internal capsule, caudate and dorsal hippocampus, were harvested. 2-MPPA levels in the serum and PVR were measured using high-performance liquid chromatography with tandem mass spectrometry (LC-MS/MS) as previously described [218, 219]. In brief, a 180-µl serum sample (or 160 µL of matrix blank and 20 µL of stock for standards) was reacted with 10 µL of 100 mM NEM for 30 min along with structurally similar internal standard at 5 µg/ml in acetonitrile. The derivatized samples were extracted with methanol followed by vortexing and centrifugation at 10,000 rpm for 5 minutes. The supernatant (50 µL) was transferred to liquid chromatography vial and a volume of 5 µL used for LC-MS/MS. The tissue samples were processed in a manner similar to serum. In brief, tissue samples were weighed, followed by addition of phosphate-buffered saline buffer (also containing 10 µL of 100 mM NEM), and volume was adjusted to obtain all samples equal per gram of tissue. The samples were homogenized, vortexed, and extracted following the same

procedure as described for serum. The calibration range was 1 - 4000 ng/ml for 2-MPPA in serum and 50–50,000 ng/ml in tissue. Samples were analyzed on an Agilent 1100 HPLC (Agilent Technologies, Santa Clara, CA) coupled to API 3000 mass spectrometer (Applied Biosystems/MDS Sciex, Toronto, ON, Canada) Derivatized-2-MPPA was separated on a Luna C18 (2 mm) 30 × 4.60 mm, 5 µM column (Phenomenex, Torrance, CA). The mobile phase consisted of acetonitrile (A), and 0.1% formic acid in Milli-Q water (B). Separation was achieved using a gradient run, with 40% (A) going to 90% (A) over a period, maintaining at 90% for 3 minutes, and then re-equilibrating over 3 minutes (40% A) at a flow rate of 350 µL/min and total run time of 10 minutes. The mass spectrometry instrument was operated in a negative ion mode. The multiple reaction monitoring (MRM) transition of derivatized 2-MPPA was 330 > 205 (Q1/Q3) and for the internal standard, 645.3 > 323.3 with a declustering potential of 40 V, entrance potential 10 V, and collision energy of 21 V. The curtain gas, ion-spray voltage, temperature, nebulizer gas (GS1), and auxiliary gas (GS2) were set at 8 psi, 5500 V, 350°C, 8 psi, and 4 psi, respectively, and the interface heater was on.

*6.2.17. Total TGF-β1 ELISA*

The CP kits from the same litter were randomly divided into three groups: PBS, free 2-MPPA and D-2MPPA. Animals received intravenous (i.v.) administration of free 2-MPPA (20 mg/kg, 200 µl), D-MPPA (containing 20 mg/kg 2-MPPA, 200 µL) or PBS (200 µL) on postnatal day 1 (PND1), sacrificed at 24 and 48 h post-injection and perfused with PBS. Total protein was isolated from the PVR brain tissues using PBS solution (100 mg brain tissue/ 500 µL PBS). Protein concentration was determined by using the BCA kit (ThermoFisher Scientific, Waltham, MA, USA). The TGF-β1 protein level was measured using LEGEND MAXTM total TGF-β1 ELISA kit (Biolegend, CA, USA) according to the manufacturer's instructions.

*6.2.18. Statistics*

All data were processed with GraphPad Prism. Data were presented as mean values ± S.D. One way-ANOVA was used for group comparisons. Statistical significance was set at $p<0.05$ for all analyses.

## 6.3. Results

*6.3.1. Characterization of Dendrimer-2MPPA and Dendrimer-2MPPA-Cy5 conjugates*

To determine the chemical structure and payload of D-2MPPA and D-2MPPA-Cy5, we characterized them with 1H-NMR (Figure 7.2A). In the 1H-NMR spectrum of 2MPPA (Figure 7.2A, bottom), the proton peaks from 1.48-1.70 ppm represent the 6 protons at 2, 3, 5 position of 2MPPA molecule. These peaks were found at around the same region (1.50-1.78 ppm) in the 1H-NMR spectrum of D-2MPPA (Figure 7.2A, top) and D-2MPPA-Cy5. The proton peaks from 2.17-2.31 ppm and 2.43-2.47 ppm represent the 3 protons at 4, 6 position and 2 protons at 1 position of 2MPPA molecule (Figure 7.2A, bottom). Due to the formation of disulfide bonds between 2MPPA and intermediate 3a and 3b, the chemical environment of these protons have changed (Figure 7.1A, top), which lead to the chemical shift of corresponding peaks to 3.20-3.30 ppm and 2.80-2.88ppm for protons at 1 and 6 position. The peaks for proton at 4 position merged with the peaks represent the internal protons of G4-OH. The presence of 2MPPA proton in the D-2MPPA, D-2MPPA-Cy5 1H-NMR spectrum and the chemical shift of some 2MPPA protons on the spectrum confirmed the successful conjugation of 2MPPA to G4-OH. To determine the number of 2MPPA molecules per G4-OH, we integrated the area of peaks corresponding to 2MPPA protons (peak 2, 3, 5); the area of peaks corresponding to the shifted G4-OH internal protons (3.90-4.10 ppm), and compared these areas with the area of peaks related to the amide

protons from D-2MPPA and D-2MPPA-Cy5. The payload of D-2MPPA and D-2MPPA-Cy5 were calculated to be approximately 13.

To assess the purity of D-2MPPA and D-2MPPA-Cy5 conjugates, we then characterized the conjugates with HPLC. We did not observe the presence of free 2MPPA molecules in the chromatogram of D-2MPPA (Figure 7.2B left). The modification and conjugation of 2-MPPA changed the surface structure of G4-OH, demonstrated by the increased elution time of D-2MPPA (~15 min) compared with unmodified G4-OH (~12 min). We also noticed that the modification broadened the peak shape G4-OH, indicating the modification dispersed the payload distribution of D-2MPPA. The labeling of Cy5 molecule to D-2MPPA greatly changed the UV spectrum of D-2MPPA, as demonstrated by the presence of characteristic peak of Cy5 at 650 nm. Nevertheless, the labeling did not significantly vary the distribution and elution of D-2MPPA (Figure 7.2B right), with only a 0.6 min elution delay and negligible variation of the peak shape between D-2MPPA and D-2MPPA-Cy5.

We have demonstrated the relative small size and neutral ζ-potential of G4-OH play a key role in determine its favorable brain distribution and pharmacokinetics [183]. Next, we sought to determine whether D-2MPPA conjugates maintained these physical properties of G4-OH. The conjugation of each 2MPPA molecule introduces two carboxyl groups to, and consumes one hydroxyl group from G4-OH; therefore, we compared the theoretical molecular weight, ζ-potential and size of D-2MPPA with G4-OH, which possess 64 terminal hydroxyl groups; and with G3.5-COOH, which maintain 64 terminal carboxyl groups (Table 1). After forming D-2MPPA, the molecular weight of G4-OH increased to 19,017 g/mole, compared with its original molecular weight 14,279 g/mole. The size of D-2MPPA also slightly increased for 30% (G4-OH: 4.4 ± 0.2 nm, D-2MPPA: 5.9±0.6 nm). Interestingly, the introducing of more carboxyl groups to

G4-OH did not significantly reduce the ζ-potential of D-2MPPA (G4-OH: 4.5 ± 0.6 mV, D-2MPPA: 3.4 ± 5.5 mV). The ζ-potential of D-2MPPA is considered as neutral, especially when compared with the ζ-potential of G3.5-COOH (-28.6 ± 0.7 mV).

We then tested the toxicity of D-2MPPA against BV-2 cell lines to make sure the modification did not change the low toxicity nature of G4-OH. We chose amine terminated generation 4 PAMAM dendrimer (G4-NH2) as positive control in this study due to the relative higher toxicity of amine terminated PAMAM dendrimers [64, 220]. D-2MPPA had very similar toxicity on BV-2 cells as G4-OH (Figure 7.1C), with the cell availability fluctuating between 73% - 97% for D-2MPPA and 77% - 107% for G4-OH when tested at a dendrimer concentration range of 1 ng/mL to 100 μg/mL. As expected, the positive control G4-NH2 demonstrated higher toxicity. When the treatment concentration was increased to 10 μg/mL, the cell availability decreased to 2.3%.

*6.3.2. D-2MPPA is stable under physiological condition but release fast under intracellular GSH concentration.*

The *in vitro* release study was designed to evaluate the stability and the triggered release of D-2MPPA conjugates. To study the stability of D-2MPPA, we investigated the release of D-2MPPA under physiologically relevant solutions such as PBS (pH=7.4) and 2 μM GSH solution (designed to mimic the extracellular GSH concentration); to study whether D-2MPPA possess triggered release property, we tested the conjugate at 10 mM GSH solution (designed to mimic the intracellular GSH concentration). We saw D-2MPPA are stable under both PBS (pH=7.4) and 2 μM GSH, with only 6.3% and 5.3% of 2MPPA release from D-2MPPA at the end of incubation (~100 hours) (Figure 7.2D bottom). However, under 10 mM GSH (intracellular GSH concentration), D-2MPPA demonstrated a fast release, with ~50% and ~80% of 2MPPA release

within 2 hours and 12 hours of incubation respectively. In addition, in the HPLC chromatogram of collected release sample, the appearance of free 2MPPA and shifting of D-2MPPA due to the reduction of payload after 4-hour incubation also confirmed the release of 2MPPA from D-2MPPA.

*6.3.3. D-2MPPA is more efficient than 2MPPA in inhibiting extracellular glutamate.*

To evaluate the efficacy of D-2MPPA and compare that with 2MPPA, we assessed the potency of D-2MPPA in glutamate inhibition, a direct effect of 2MPPA as GCPII inhibitor. The glutamate pathway involves both activated neurons and glial cells. Brian slice from CP kits contains both cells types and preserved the activities of many biological pathways. In addition, since 2MPPA inhibits the production of extracellular glutamate in the CNS, which can be separately measured in the culture medium in this *ex vivo* slice culture system, we chose brain slices generated from PND1 CP rabbit kit as a platform for this study. To evaluate the dose response, we treated the brain slices with 0.1 μM (for 2MPPA, IC50 = 0.09 μM [221]) and 10 μM 2MPPA (~100-fold of IC50 dose, 2-fold of D-2MPPA accumulation in the PVR region from the CP kits). The positive control received PBS treatment. The slice preparation and treatment procedures were described in Figure 7.3A.

Since the brain slices were generated from the brain of CP rabbit kit, where both excitotoxicity and neuroinflammation were presented, an increased total glutamate concentration with time was expected. In the PBS treated group (Figure 7.3B), we saw a 5.9-fold increase of total glutamate production between 24 hours (4.19 units) and 6 hours (0.72 units).

In general, D-2MPPA is more effective in inhibiting extracellular glutamate production (measured from culture medium) than 2MPPA (Figure 7.3B). Specifically, at 6 hours, 0.1 μg/mL of 2-MPPA significantly inhibited the glutamate production for 29% (~0.51 unit) compared with

the PBS group (~0.72 unit); increasing the treatment dose to 10 μg/mL did not show better inhibitory effect, yet resulted in a slight reduction of glutamate inhibition (18% inhibition compared with PBS treated group). D-2MPPA had better inhibition effect (31% inhibition) at lower dose than 2MPPA. However, it is worth noting that increasing the D-2MPPA dose for 100-fold further enhanced the inhibitory effects to 54% inhibition. At 24 hours, newly produced extracellular glutamate diffused into the culture medium. A more pronounced inhibition was observed as a result of longer incubation time. 2MPPA inhibited glutamate production (2.1units) for 50% at lower dose compare to PBS treatment (4.2 units), yet still displayed worse inhibitory effect at higher dose (43%). Interestingly, D-2MPPA had better effect than 2MPPA at lower dose, with a 60% inhibition of glutamate production at lower dose, but demonstrated a strong inhibition at higher dose (81% glutamate inhibition). We also observed that both 2MPPA and D-2MPPA inhibited the tissue glutamate production, yet the inhibitory effect was not as strong as for the extracellular glutamate measured from the culture medium.

*6.3.4. D-2MPPA improve the TGF-β level of LPS treated BV-2 cells*

The inhibition of glutamate production is concomitant with the increase of NAAG in the CNS, which further activates mGluR3 and induces the release of TGF-β [222]. This can decrease microglial activation and potentially enable conversion of activated microglia to a more anti-inflammatory phenotype. Therefore, we sought to determine if D-2MPPA can improve the TGF-β level when microglial cells are activated. BV-2 cells were first treated with 100 ng/mL LPS for 3 hours to induce activation. We found LPS treatment suppressed the TGF-β expression for ~50% compared with control group (Figure 7.4). After exposing BV-2 cells to LPS, we then applied different doses of D-2MPPA/MPPA to BV-2 cells for 24 hours (i.e. 0.1 μg/mL, 1 μg/mL, and 10 μg/mL). BV-2 demonstrated a dose responsive effect to the 2MPPA treatment (Figure

7.4), with 20%, 68%, and 160% TGF-β improvement at 0.1 μg/mL, 1.0 μg/mL, and 10.0 μg/mL concentration of 2MPPA treatment. Interestingly, treatment of BV-2 cells with 0.1 μg/mL D-2MPPA dramatically improved the TGF-β level for 140%. This TGF-β enhancement is similar to the effect of 10.0 μg/mL 2MPPA treatment (160% enhancement). Even though D-2MPPA did not show significant dose response, the TGF-β levels in all D-2MPPA treated groups were close or higher than the TGF-β in the control groups, indicating the D-2MPPA enhanced the efficacy of 2MPPA.

*6.3.5. Dendrimer promotes the cell-specific 2-MPPA delivery*

To determine whether the dendrimer can deliver the 2MPPA in a cell specific manner, we systematically (i.v.) injected the D-2MPPA-cy5 on PND1 in endotoxin kits and analyzed the D-2MPPA-cy5 distribution in the PVR 24 h post-injection. We found that the D-2MPPA-cy5 is co-localized with GCPII in both activation microglia and astrocytes in endotoxin kits (Figure 7.4B).

*6.3.6. Dendrimers enhance the brain uptake of 2MPPA*

To determine whether the glial-specific targeting property of D-2MPPA can result in higher accumulation of 2-MPPA at the injury site, we intravenously (i.v.) administrated D-2MPPA (containing 20mg/kg of 2-MPPA) and 2-MPPA (20 mg/kg) to the CP kits and the healthy control kits. The concentration of 2-MPPA at the PVR region and in the serum were analyzed at 1, 3, 24 and 48 h post-injection (Figure 7.6A). We found that 2-MPPA level in the PVR region of D-2MPPA CP group at each time point was higher than the effective concentration (IC50 = 90 nM). The 2-MPPA level in the endotoxin D-2MPPA group peaked at 3 h post-injection (4.3 μM, ~50 fold of IC50), which was 7.2-fold higher than the endotoxin 2-MPPA group (0.6 μM), indicating the dendrimer enhanced the 2MPPA brain penetration. Whereas, this enhanced drug accumulation in PVR was not observed in the healthy control kits without injury. In the PVR

region of healthy control kits, the concentration of both D-2MPPA and 2MPPA decreased over time, and showed very similar level of accumulation at 3 hours (D-2MPPA: 0.9 μM, 2-MPPA: 0.5 μM) and 24 hours (D-2MPPA: 0.05 μM, 2MPPA: 0.5 μM).

We further analyzed the serum 2-MPPA level in D-2MMPA and 2-MPPA group to determine the association between brain uptake and serum 2-MPPA level. We found that the free 2-MPPA level was similar among all the groups at 1 h post-injection. The 2-MPPA level in the 2-MPPA group in CP kits and the healthy controls (D-2MPPA and 2-MPPA groups) rapidly decreased 1 h post-injection (Figure 7.6A), which is consistent with a previous study in a rat model of neuropathic pain, in which the free 2-MPPA was rapidly cleared out during the first hour after administrated intravenously [218]. However, the free 2-MPPA serum level in the D-2MPPA CP group kept elevated at 3 h post-injection and higher concentration in the serum at all the monitored time points. These results demonstrate that D-2MPPA enhanced the circulation time of free drug in the CP kits. Moreover, the higher serum 2-MPPA level may indicate the deficiency of clearance in the CP kits.

*6.3.7. The accumulation of 2-MPPA in the PVR correlates with the extent of brain injury*

To determine the correlation of the 2-MPPA level and the disease phenotype, we plotted the PVR 2-MPPA level against the disease phenotype in the CP kits. We found that the 2-MPPA brain uptake in the D-2MPPA endotoxin group is closely correlated with the disease phenotype, the more severe the disease phenotype, the higher level of the 2-MPPA uptake (Figure 7.6B), which may be related to the extent of the blood brain barrier injury.

*6.3.8. D-2MPPA treatment improved the short-term neurobehavior of CP rabbit.*

To evaluate the effect of D-2MPPA on neuroinflammation, we evaluated the short-term neurobehavior of healthy control, PBS, MPPA, DMPPA treated group at 0 h and 48 h post

treatment (Figure 7.7). The D-2MPPA significantly improved the sucking and swallowing, head movement and muscle tone, compared with the PBS or MPPA treated groups.

## 6.4. Discussion

Dendrimers could enhance the brain uptake of small molecule drugs, even though this has not been proved directly. Our study provided a direct proof that D-2MPPA enhanced the accumulation of 2MPPA in the injured brain, by measuring the 2MPPA concentration in the PVR region. We found a 7.2-fold increase of 2MPPA uptake enabled by D-2MPPA, when it reached its peak concentration in the PVR (Figure 7.6A). This enhanced brain uptake in the CP kits was associated with the upgraded serum concentration in the D-2MPPA injected group. The dendrimer pharmacokinetics and the pathology of CP both contributed to the increase in the 2MPPA concentration of the D-2MPPA injected group. PAMAM dendrimers are believed to enhance the systemic circulation time of free drug molecules [211]. We showed here D-2MPPA increased the serum concentration of 2MPPA in both CP and control kits. Interestingly, we also found dendrimer demonstrated a higher concentration in the serum of CP kits, than the serum of control kits. But this difference was observed among free 2MPPA injected groups. Renal filtration has been identified as the major clearance pathway for hydroxyl terminated G4 PAMAM dendrimers in many animal models [95, 183]. The increased 2MPPA concentration in the D-2MPPA injected CP kits was probably associated with the damaged renal function in these kits. However, this also provided a higher opportunity for D-2MPPA to passively diffuse across the leaked BBB and entering the brain.

In the CP kits, the 2MPPA accumulation in the PVR region of D-2MPPA injected group demonstrated large variation, which is not observed in the control kits. Therefore, we further

phenotyped the uptake of 2MPPA in CP rabbit kits, and demonstrated a positive correlation between 2MPPA uptake in the brain and the disease severity was shown in the D-2MPPA administrated group, and a lack of correlation of negative correlation was shown in the free 2MPPA injected group (Figure 7.6B). This finding was probably related to the dendrimers property to accumulate and retain in the brain where the BBB is more impaired, and population of activated microglial cells are alleviated, indicating the potential to use dendrimer as an imaging tool for the assessment of neuroinflammation [211]. The lack of positive correlation in the free 2MPPA injected group might limit their application in the treatment of severely injured patients in clinics, since 2MPPA demonstrated least accumulation in the severely injured brain. However, conjugating 2MPPA to dendrimer solved this problem, and increased the probability in the clinical translation of dendrimer-based nanomedicine.

As a member of GCPII inhibitor, 2MPPA impose its inhibitory effect by forming a complex with GCPII receptors, and therefore hindering the interaction of NAAG with GCPII receptors. Specifically, the glutarate (pentanedioic acid) portion of the 2MPPA can interact with the C-terminal glutamate recognition site of GCPII, and the thiol group of 2MPPA can form chelation with the active site zinc ion [223], although no study has shown both of these interactions are needed to interfere with the normal function of GCPII. In the presence of neuroinflammation, dendrimers could intrinsically target activated microglia and astrocytes [86], which have been shown to have upgraded expression of GCPII receptors on their cell members [224]. Therefore, we hypothesize that when conjugated with 2MPPA, dendrimers have the ability to increase the probability of 2MPPA to interact with GCPII by delivering 2MPPA to the GCPII expressing cells. In the rabbit model of CP, we successfully identified the expression of GCPII receptors on the activated astrocytes and microglial cells in the PVR region of PND1 CP kits. (Figure 4B).

We also observed the co-localization of D-2MPPA with LPS activated astrocytes *in vitro* (Figure 4A), and localization of D-2MPPA with GCPII receptor expressed on the activated microglia and astrocytes. This observation indicated that dendrimers not only increased the brain uptake of 2MPPA in the CP kits, but also favored the interaction between 2MPPA and GCPII receptor by targeted deliver 2MPPA to the GCPII expressing cells. Even when brain slices from CP kits were exposed to free 2MPPA and D-2MPPA at the same dose, this cell-specific delivery of 2MPPA enabled a better inhibition on extracellular glutamate production.

Lastly, we showed that targeting glutamate excitotoxicity also helped in attenuating neuroinflammation, indicating a new aspect in the treatment of CP.

## 6.5. Conclusion

In this study, we have showed that by covalently conjugating a GCPII inhibitor 2MPPA to the dendrimers, we could increase the accumulation of 2MPPA in the injured brain of CP kits. This accumulation of dendrimer delivered 2MPPA was positively correlated with the disease severity. D-2MPPA targeted the activated microglia and astrocytes and co-localized with the GCPII receptor expressed on these cells. This dendrimer-based targeted delivery resulted in a better effect in inhibiting the extracellular glutamate production in the brain tissue, improving the TGF-β level *in vitro*, and further attenuated the neuroinflammation *in vivo*, with significant clinical applications.

**Table 6.51. The characterization of theoretical molecular weight (Mw), size, and ζ-potential of dendrimers.**

| Dendrimer | Theoretical Mw (g/mole) | Size ± SEM (nm) | ζ-potential ± SEM (mV) |
|---|---|---|---|
| **G4-OH** | 14,279 | 4.4 ± 0.2 | 4.5 ± 0.6 |
| **G3.5-COOH** | 12,931 | 3.2±0.4 | -28.6 ± 0.7 |
| **D-2MPPA** | 19,017 | 5.9±0.6 | 3.4 ± 5.5 |
| **D-2MPPA-Cy5** | 19,555 | - | - |

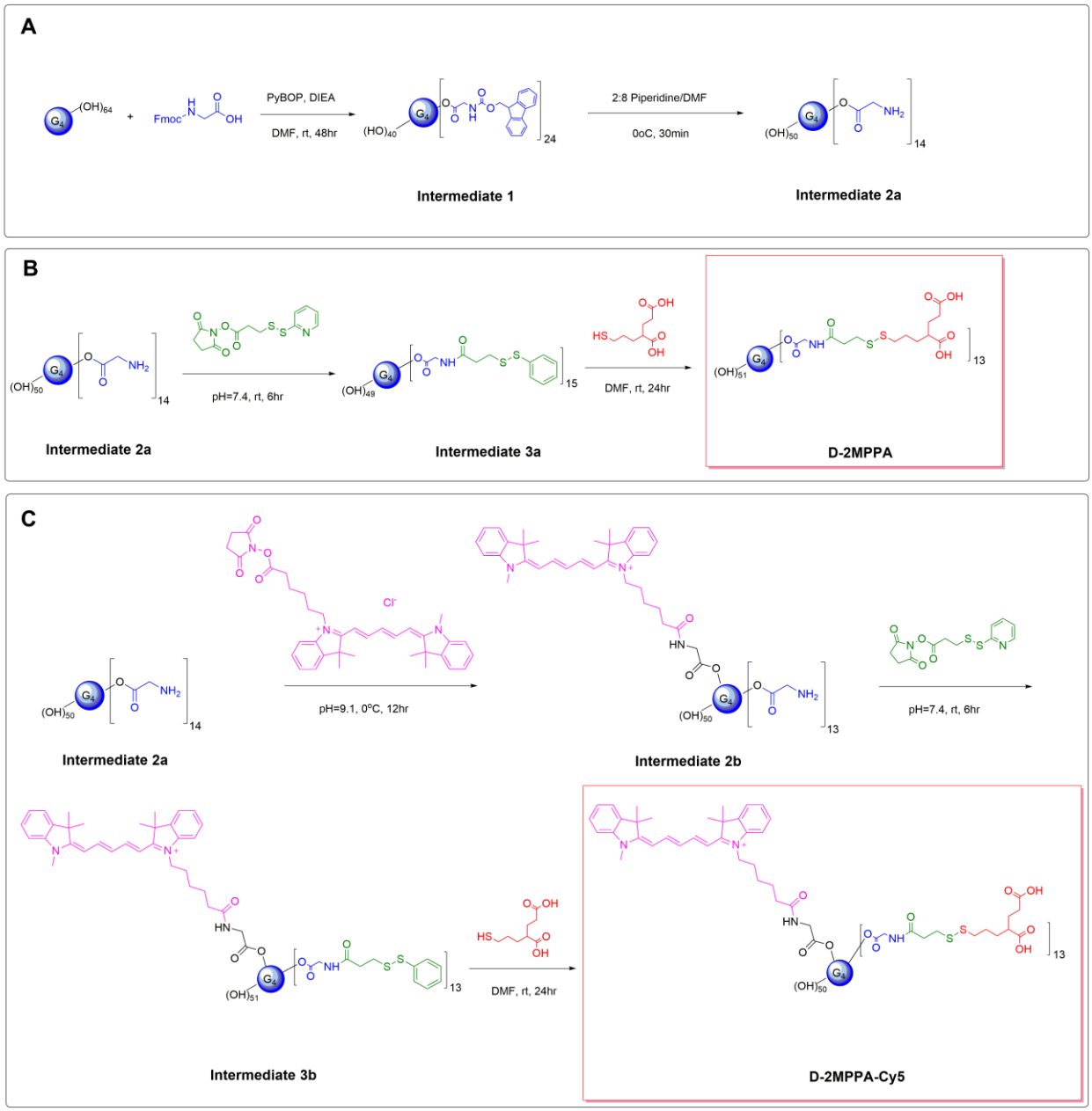


**Figure 6.5.1. Synthesis scheme of D-2MPPA and Cy5 labeled D-2MPPA (D-2MPPA-Cy5).**

(A) Preparation of amine functionalized bifunctional dendrimer (Intermediate 2a); (B) Preparation of Dendrimer-2-MPPA conjugate (D-2MPPA); (C) Preparation of Cy5 labeled Dendrimer-2-MPPA conjugate (D-2MPPA-Cy5)

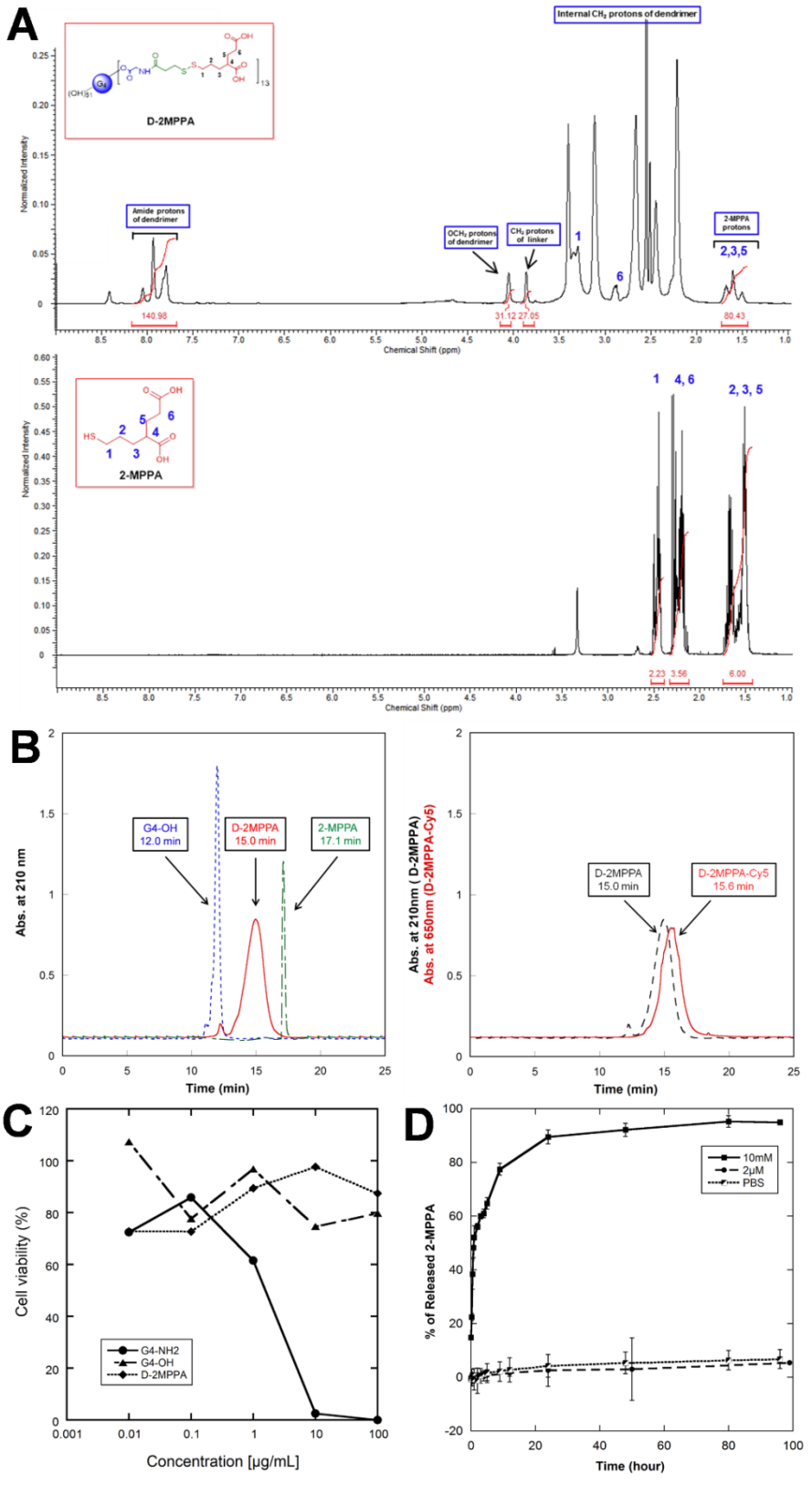
A
D-2MPPA
Internal CH2 protons of dendrimer
Amide protons of dendrimer
OCH2 protons of dendrimer
CH2 protons of linker
2-MPPA protons
1
6
2,3,5
140.98
31.12
27.05
80.43
Normalized Intensity
Chemical Shift (ppm)
2-MPPA
1
4, 6
2, 3, 5
2.23
3.56
6.00
B
G4-OH 12.0 min
D-2MPPA 15.0 min
2-MPPA 17.1 min
Abs. at 210 nm
Time (min)
D-2MPPA 15.0 min
D-2MPPA-Cy5 15.6 min
Abs. at 210nm ( D-2MPPA)
Abs. at 650nm (D-2MPPA-Cy5)
C
Cell viability (%)
G4-NH2
G4-OH
D-2MPPA
Concentration [μg/mL]
D
% of Released 2-MPPA
10mM
2μM
PBS
Time (hour)

**Figure 6.52. Characterization of D-2MPPA and D-2MPPA-Cy5.**

(A) 1H-NMR spectra of D-2MPPA (top), and 2MPPA (bottom). The appearance of 2MPPA protons (Figure 1A bottom, 1, 2, 3, 5, 6 positons in 2MPPA molecule) in D-2MPPA (Figure 1A top); the chemical shift of 2MPPA protons at position 1, 6 and internal protons from G4-OH confirmed the success of conjugation; the payload of 2MPPA was calculated to be around 13 based on integration of 2MPPA protons and compare to integration of amide protons from G4-OH. (B) The HPLC chromatogram of G4-OH, D-2MPPA, 2MPPA confirmed the purity and the successful conjugation of 2-MPPA to G4-OH. Left: the elution time for 2-MPPA (17.1 min), G4-OH (12.0 min), and D-2MPPA conjugate (15.0 min) are different from each other. All peaks were monitored at λ=212 nm. Right: the elution of D-2MPPA (15.0 min) and D-2MPPA-Cy5 (15.6 min). The slightly shift of retention time of D-2MPPA-Cy5 indicated the labeling of Cy5-NHS ester to the D-2MPPA. D-2MPPA-Cy5 was monitored under λ=650 nm. (C) The toxicity of G4-OH, D-2MPPA, and G4-NH2 against BV-2 cells lines. D-2MPPA demonstrated low toxicity against BV-2 cells as G4-OH, G4-NH2 displayed toxicity against BV-2 cells at a concentration of 1 μg/mL. (D) The release profile of D-2MPPA at different *in vitro* conditions, monitored by HPLC at λ=210nm. D-2MPPA is stable under physiological pH (pH=7.4) and extracellular GSH concentration (2 μM) during the ~100 hours of incubation time. The release of D-2MPPA is triggered by the intracellular concentration of GSH (10 mM), with 50% of 2MPPA released after 2 hours of incubation.

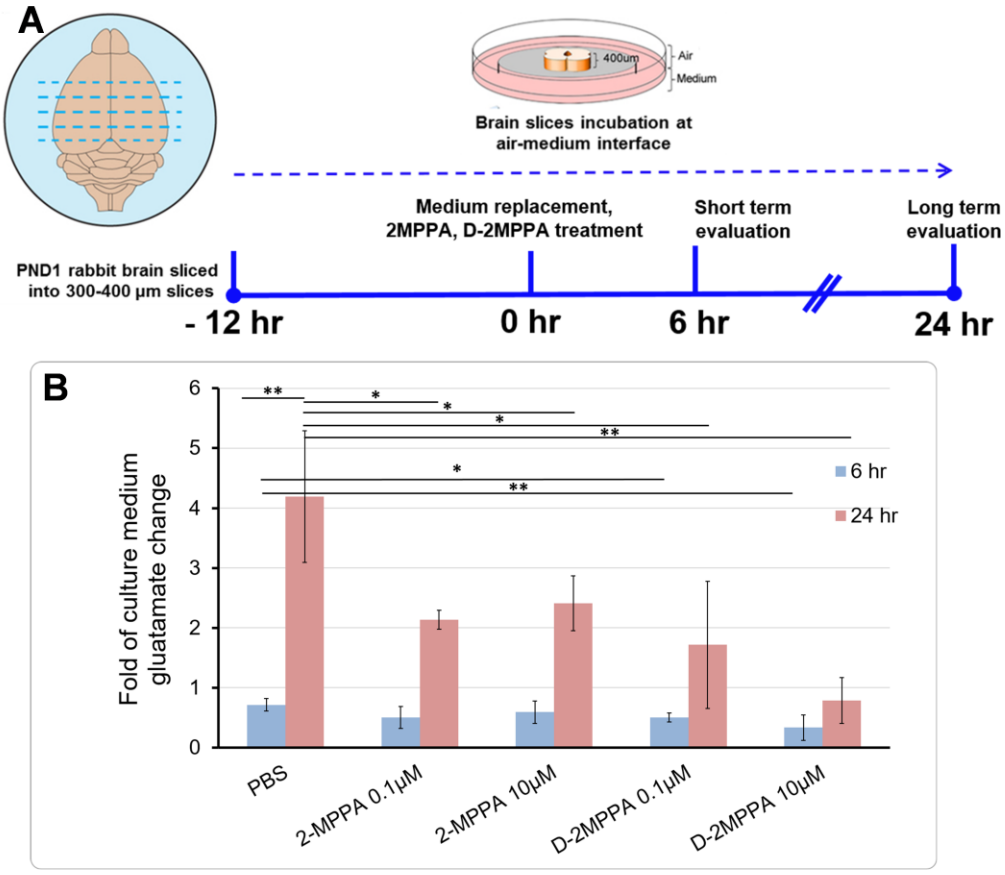


**Figure 6.53. D-2MPPA/2MPPA inhibited glutamate production in *ex vivo* brain slice culture.**

(A) *Ex vivo* brain slice culture experiment scheme. The brain slices were treated with different doses of PBS/D-2MPPA/2MPPA for 6 hours or 24 hours before the tissue and culture medium were collected. (B) The glutamate concentrations measured in the culture medium from each group. In *ex vivo* brain slice culture platform, the culture medium glutamate represents the extracellular glutamate. At similar dose, D-2MPPA inhibited extracellular glutamate production more efficiently than 2MPPA. The measured glutamate concentrations from all samples were normalized by the internal control (glutamate amount in the brain slice at 6 hours post PBS treatment). For each group, 4-6 slices from 3 different rabbit kits were measured.

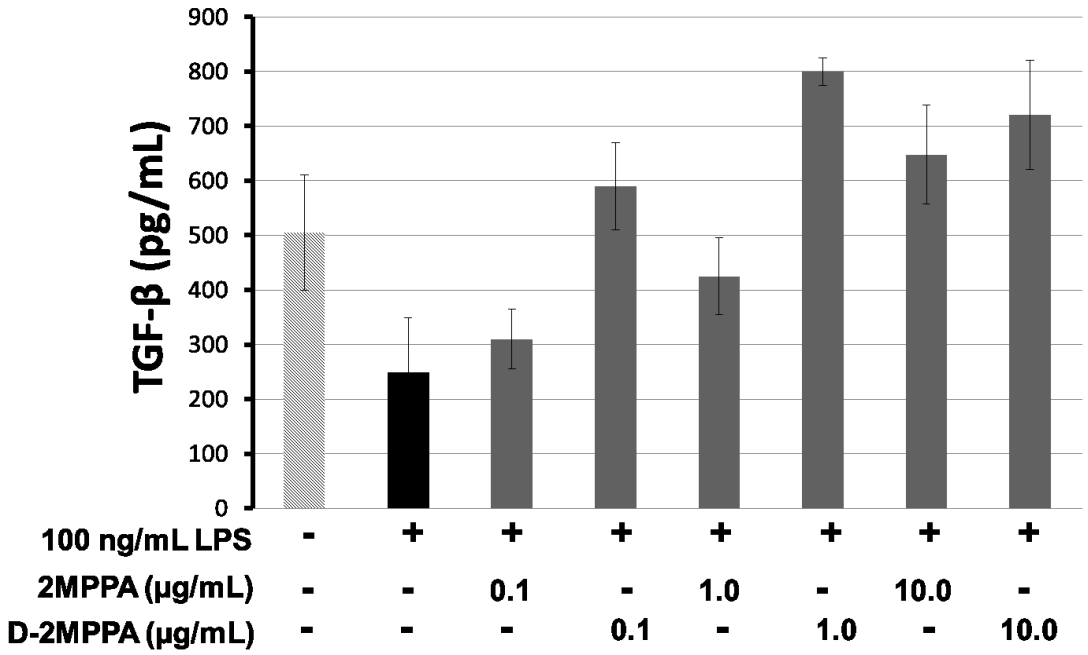


**Figure 6.54. D-2MPPA enhanced the TGF-β level in LPS treated BV-2 cells.**

Treatment of BV-2 cells with 100 ng/mL LPS for 3 hours suppressed the TGF-β for 50% (black bar) compared with the control group (shaded black bar). Gray bars: Treatment of LPS activated BV-2 cell with 2MPPA for 24 hours (0.1 µg/mL, 1 µg/mL, and 10 µg/mL) enhanced the TGF-β level in a dose responsive manner. Treatment of LPS activated BV-2 cell with D-2MPPA (0.1 µg/mL, 1 µg/mL, and 10 µg/mL) improved the TGF-β to concentrations that were close to or higher than the control group.

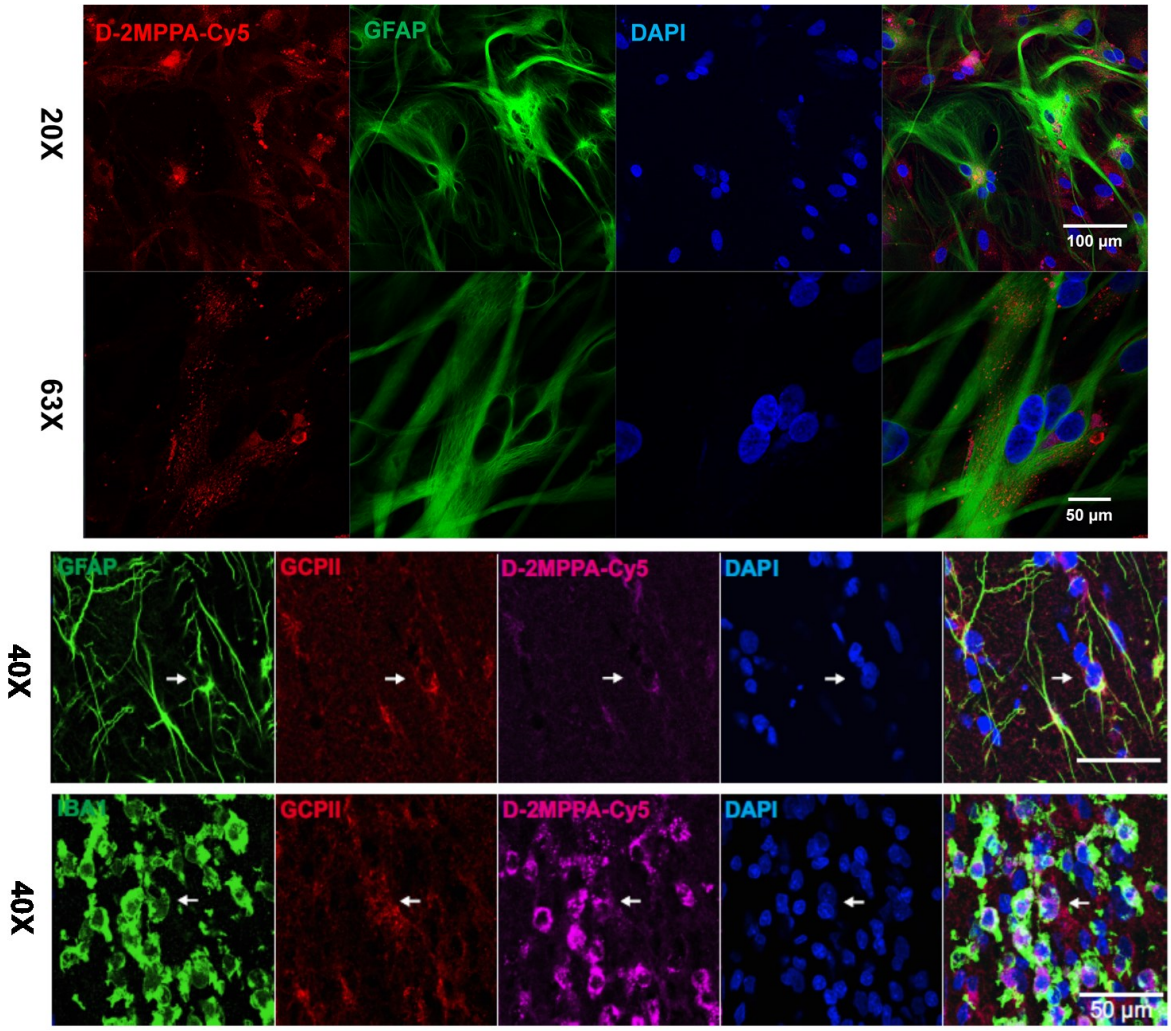


**Figure 6.55. *In vitro* and *in vivo* cell localization of D-2MPPA-Cy5 with microglia and astrocytes.**

(A) *In vitro* treatment of D-2MPPA-Cy5 on LPS activated the mixed glial cell culture, D-2MPPA-Cy5 was shown to co-localize with the activated astrocytes. Red: D-2MPPA-Cy5; Green: Anti-GFAP; Blue: DAPI. Scale bar: 50 µm. (B) The *in vivo* study showed the co-localization of D-2MPPA-Cy5 with GCPII receptors expressed on the activated microglia and astrocytes at 24 h post D-2MPPA administration. Images were taken at the PVR region of the brain form CP kits. Green: Anti-GFAP; Red: Anti-GCPII; Purple: D-2MPPA-Cy5; Blue: DAPI.

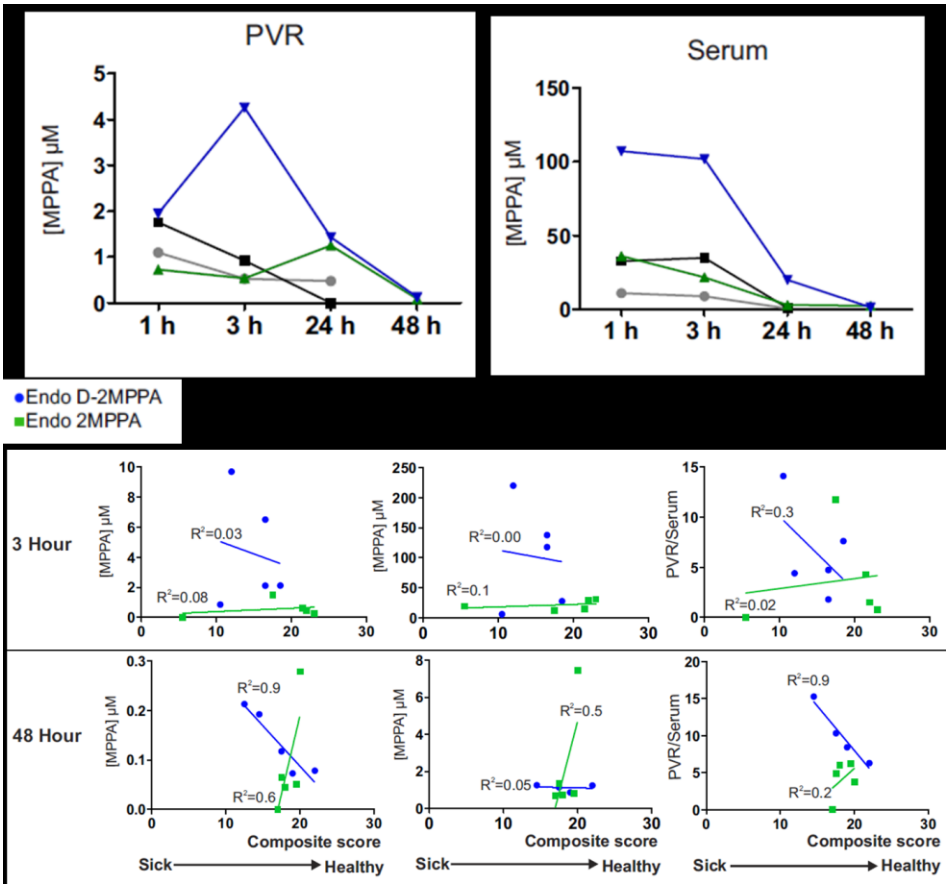


**Figure 6.56. The pharmacokinetic analysis of intravenously administrated D-2MPPA and 2MPPA.**

(A) The accumulation of 2MPPA in the in the PVR region and serum of CP and healthy control kits. D-2MPPA demonstrated the highest accumulation in the PVR of CP kits, with a peak accumulation at 3 hours (4.2 µM, ~50-fold of IC50 concentration, ~7.2-fold higher than free drug accumulation) post injection and gradually cleared out within 48 hours. In the PVR region of healthy control kits, the concentration of both 2MPPA and D-2MPPA decreased with time. In the serum, the concentration of free drug decreased rapidly within the first hour after administration, with 0.3%ID/mL and 1.0%ID/mL of 2MPPA left in the serum. Both D-2MPPA and free 2MPPA showed higher concentration in the serum of CP kits compared with those of healthy control. (B) For D-2MPPA injected groups, accumulation of 2MPPA in the PVR region of CP kits was

positively correlated with the disease severity.

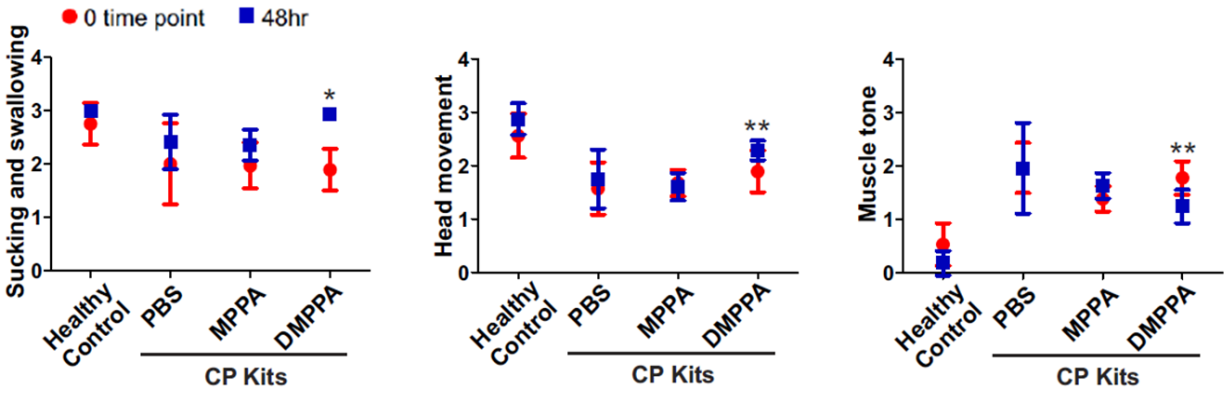


**Figure 6.57. D-2MPPA treatment improved the short-term neurobehavior of CP rabbit.**

## REFERENCES


[1] Krex D, Klink B, Hartmann C, von Deimling A, Pietsch T, Simon M, et al. Long-term survival with glioblastoma multiforme. Brain. 2007;130:2596-606.
[2] Kreuter J. Drug delivery to the central nervous system by polymeric nanoparticles: What do we know? Advanced Drug Delivery Reviews. 2014;71:2-14.
[3] Pardridge WM. The blood-brain barrier: bottleneck in brain drug development. NeuroRx : the journal of the American Society for Experimental NeuroTherapeutics. 2005;2:3-14.
[4] Abbott NJ, Patabendige AAK, Dolman DEM, Yusof SR, Begley DJ. Structure and function of the blood-brain barrier. Neurobiology of Disease. 2010;37:13-25.
[5] Schinkel AH. P-glycoprotein, a gatekeeper in the blood-brain barrier. Advanced Drug Delivery Reviews. 1999;36:179-94.
[6] Begley DJ. ABC transporters and the blood-brain barrier. Current Pharmaceutical Design. 2004;10:1295-312.
[7] Chuang VTG, Kragh-Hansen U, Otagiri M. Pharmaceutical strategies utilizing recombinant human serum albumin. Pharmaceutical Research. 2002;19:569-77.
[8] Jefferies WA, Brandon MR, Hunt SV, Williams AF, Gatter KC, Mason DY. TRANSFERRIN RECEPTOR ON ENDOTHELIUM OF BRAIN CAPILLARIES. Nature. 1984;312:162-3.
[9] Demeule M, Poirier J, Jodoin J, Bertrand Y, Desrosiers RR, Dagenais C, et al. High transcytosis of melanotransferrin (P97) across the blood brain barrier. Journal of Neurochemistry. 2002;83:924-33.
[10] Talukder MJR, Takeuchi T, Harada E. Receptor-mediated transport of lactoferrin into the cerebrospinal fluid via plasma in young calves. Journal of Veterinary Medical Science. 2003;65:957-64.
[11] Dehouck B, Fenart L, Dehouck MP, Pierce A, Torpier G, Cecchelli R. A new function for the LDL receptor: Transcytosis of LDL across the blood-brain barrier. Journal of Cell Biology. 1997;138:877-89.
[12] Zlokovic BV. The blood-brain barrier in health and chronic neurodegenerative disorders. Neuron. 2008;57:178-201.
[13] Hawkins BT, Davis TP. The blood-brain barrier/neurovascular unit in health and disease. Pharmacological Reviews. 2005;57:173-85.
[14] Krol S, Macrez R, Docagne F, Defer G, Laurent S, Rahman M, et al. Therapeutic benefits from nanoparticles: the potential significance of nanoscience in diseases with compromise to the blood brain barrier. Chemical reviews. 2013;113:1877-903.
[15] Munn LL. Aberrant vascular architecture in tumors and its importance in drug-based therapies. Drug discovery today. 2003;8:396-403.
[16] Bertossi M, Virgintino D, Maiorano E, Occhiogrosso M, Roncali L. Ultrastructural and morphometric investigation of human brain capillaries in normal and peritumoral tissues. Ultrastructural pathology. 1997;21:41-9.
[17] Meyers JD, Doane T, Burda C, Basilion JP. Nanoparticles for imaging and treating brain cancer. Nanomedicine (Lond). 2013;8:123-43.
[18] Cirrito JR, Deane R, Fagan AM, Spinner ML, Parsadanian M, Finn MB, et al. P-glycoprotein deficiency at the blood-brain barrier increases amyloid-beta deposition in an Alzheimer disease mouse model. Journal of Clinical Investigation. 2005;115:3285-90.
[19] Vogelgesang S, Cascorbi I, Schroeder E, Pahnke J, Kroemer HK, Siegmund W, et al. Deposition of Alzheimer's beta-amyloid is inversely correlated with P-glycoprotein expression in the brains of elderly non-demented humans. Pharmacogenetics. 2002;12:535-41.
[20] Deane R, Zlokovic BV. Role of the blood-brain barrier in the pathogenesis of Alzheimer's disease. Current Alzheimer Research. 2007;4:191-7.
[21] Bartels AL, Willemsen ATM, Kortekaas R, de Jong BM, de Vries R, de Klerk O, et al. Decreased blood-brain barrier P-glycoprotein function in the progression of Parkinson's disease, PSP and MSA. Journal of Neural Transmission. 2008;115:1001-9.

[22] Kortekaas R, Leenders KL, van Oostrom JCH, Vaalburg W, Bart J, Willemsen ATM, et al. Blood-brain barrier dysfunction in Parkinsonian midbrain in vivo. Annals of Neurology. 2005;57:176-9.
[23] Hanisch UK, Kettenmann H. Microglia: active sensor and versatile effector cells in the normal and pathologic brain. Nature Neuroscience. 2007;10:1387-94.
[24] Kettenmann H, Hanisch UK, Noda M, Verkhratsky A. Physiology of Microglia. Physiological Reviews. 2011;91:461-553.
[25] Charles NA, Holland EC, Gilbertson R, Glass R, Kettenmann H. The Brain Tumor Microenvironment. Glia. 2011;59:1169-80.
[26] Jack C, Ruffini F, Bar-Or A, Antel JP. Microglia and multiple sclerosis. Journal of Neuroscience Research. 2005;81:363-73.
[27] Watters JJ, Schartner JM, Badie B. Microglia function in brain tumors. Journal of Neuroscience Research. 2005;81:447-55.
[28] Glass CK, Saijo K, Winner B, Marchetto MC, Gage FH. Mechanisms Underlying Inflammation in Neurodegeneration. Cell. 2010;140:918-34.
[29] McGeer PL, McGeer EG. Targeting microglia for the treatment of Alzheimer's disease. Expert Opinion on Therapeutic Targets. 2015;19:497-506.
[30] Cherry JD, Olschowka JA, O'Banion MK. Neuroinflammation and M2 microglia: the good, the bad, and the inflamed. Journal of Neuroinflammation. 2014;11.
[31] Boche D, Perry VH, Nicoll JA. Review: activation patterns of microglia and their identification in the human brain. Neuropathol Appl Neurobiol. 2013;39:3-18.
[32] Liu T, Gao YJ, Ji RR. Emerging role of Toll-like receptors in the control of pain and itch. Neuroscience Bulletin. 2012;28:131-44.
[33] Moskowitz MA, Lo EH, Iadecola C. The Science of Stroke: Mechanisms in Search of Treatments. Neuron. 2010;67:181-98.
[34] Hu XM, Li PY, Guo YL, Wang HY, Leak RK, Chen SE, et al. Microglia/Macrophage Polarization Dynamics Reveal Novel Mechanism of Injury Expansion After Focal Cerebral Ischemia. Stroke. 2012;43:3063-U474.
[35] Evans MC, Couch Y, Sibson N, Turner MR. Inflammation and neurovascular changes in amyotrophic lateral sclerosis. Molecular and Cellular Neuroscience. 2013;53:34-41.
[36] Blandini F. Neural and Immune Mechanisms in the Pathogenesis of Parkinson's Disease. Journal of Neuroimmune Pharmacology. 2013;8:189-201.
[37] Tannahill GM, Iraci N, Gaude E, Frezza C, Pluchino S. Metabolic reprograming of mononuclear phagocytes in progressive multiple sclerosis. Frontiers in Immunology. 2015;6:7.
[38] Hwang O. Role of oxidative stress in Parkinson's disease. Experimental neurobiology. 2013;22:11-7.
[39] Michelucci A, Heurtaux T, Grandbarbe L, Morga E, Heuschling P. Characterization of the microglial phenotype under specific pro-inflammatory and anti-inflammatory conditions: Effects of oligomeric and fibrillar amyloid-beta. Journal of Neuroimmunology. 2009;210:3-12.
[40] Perry VH, Nicoll JA, Holmes C. Microglia in neurodegenerative disease. Nat Rev Neurol. 2010;6:193-201.
[41] S. Breza T J, Magro CM. Lichenoid and granulomatous dermatitis associated with atypical mycobacterium infections. J Cutan Pathol. 2006;33:512-5.
[42] Surace MJ, Block ML. Targeting microglia-mediated neurotoxicity: the potential of NOX2 inhibitors. Cellular and Molecular Life Sciences. 2012;69:2409-27.
[43] Chen H, Kim GS, Okami N, Narasimhan P, Chan PH. NADPH oxidase is involved in post-ischemic brain inflammation. Neurobiology of Disease. 2011;42:341-8.
[44] Nayak D, Huo Y, Kwang WXT, Pushparaj PN, Kumar SD, Ling EA, et al. SPHINGOSINE KINASE 1 REGULATES THE EXPRESSION OF PROINFLAMMATORY CYTOKINES AND NITRIC OXIDE IN ACTIVATED MICROGLIA. Neuroscience. 2010;166:132-44.

[45] Tikka T, Fiebich BL, Goldsteins G, Keinanen R, Koistinaho J. Minocycline, a tetracycline derivative, is neuroprotective against excitotoxicity by inhibiting activation and proliferation of microglia. Journal of Neuroscience. 2001;21:2580-8.
[46] Zhou Y, Ling E-A, Dheen ST. Dexamethasone suppresses monocyte chemoattractant protein-1 production via mitogen activated protein kinase phosphatase-1 dependent inhibition of Jun N-terminal kinase and p38 mitogen-activated protein kinase in activated rat microglia. Journal of Neurochemistry. 2007;102:667-78.
[47] da Fonseca AC, Badie B. Microglia and macrophages in malignant gliomas: recent discoveries and implications for promising therapies. Clin Dev Immunol. 2013;2013:264124.
[48] Komohara Y, Ohnishi K, Kuratsu J, Takeya M. Possible involvement of the M2 anti-inflammatory macrophage phenotype in growth of human gliomas. Journal of Pathology. 2008;216:15-24.
[49] Wu A, Wei J, Kong LY, Wang YT, Priebe W, Qiao W, et al. Glioma cancer stem cells induce immunosuppressive macrophages/microglia. Neuro-Oncology. 2010;12:1113-25.
[50] Noy R, Pollard JW. Tumor-associated macrophages: from mechanisms to therapy. Immunity. 2014;41:49-61.
[51] Wesolowska A, Kwiatkowska A, Slomnicki L, Dembinski M, Master A, Sliwa M, et al. Microglia-derived TGF-beta as an important regulator of glioblastoma invasion - an inhibition of TGF-beta-dependent effects by shRNA against human TGF-beta type II receptor. Oncogene. 2008;27:918-30.
[52] Markovic DS, Vinnakota K, Chirasani S, Synowitz M, Raguet H, Stock K, et al. Gliomas induce and exploit microglial MT1-MMP expression for tumor expansion. Proceedings of the National Academy of Sciences of the United States of America. 2009;106:12530-5.
[53] Held-Feindt J, Hattermann K, Mueerkoester SS, Wedderkopp H, Knerlich-Lukoschus F, Ungefroren H, et al. CX3CR1 promotes recruitment of human glioma-infiltrating microglia/macrophages (GIMs). Experimental Cell Research. 2010;316:1553-66.
[54] Zhai HY, Heppner FL, Tsirka SE. Microglia/Macrophages Promote Glioma Progression. Glia. 2011;59:472-85.
[55] Tomalia DA, Baker H, Dewald J, Hall M, Kallos G, Martin S, et al. A New Class of Polymers - Starburst-Dendritic Macromolecules. Polym J. 1985;17:117-32.
[56] Tomalia DA. Birth of a new macromolecular architecture: dendrimers as quantized building blocks for nanoscale synthetic polymer chemistry. Prog Polym Sci. 2005;30:294-324.
[57] Venuganti VV, Sahdev P, Hildreth M, Guan X, Perumal O. Structure-skin permeability relationship of dendrimers. Pharm Res. 2011;28:2246-60.
[58] Nanjwade BK, Bechra HM, Derkar GK, Manvi FV, Nanjwade VK. Dendrimers: emerging polymers for drug-delivery systems. European journal of pharmaceutical sciences : official journal of the European Federation for Pharmaceutical Sciences. 2009;38:185-96.
[59] Menjoge AR, Kannan RM, Tomalia DA. Dendrimer-based drug and imaging conjugates: design considerations for nanomedical applications. Drug Discov Today. 2010;15:171-85.
[60] Sadekar S, Ghandehari H. Transepithelial transport and toxicity of PAMAM dendrimers: implications for oral drug delivery. Adv Drug Deliv Rev. 2012;64:571-88.
[61] Bhadra D, Bhadra S, Jain S, Jain NK. A PEGylated dendritic nanoparticulate carrier of fluorouracil. International journal of pharmaceutics. 2003;257:111-24.
[62] Ding BS, Dziubla T, Shuvaev VV, Muro S, Muzykantov VR. Advanced drug delivery systems that target the vascular endothelium. Mol Interv. 2006;6:98-112.
[63] Duncan R, Izzo L. Dendrimer biocompatibility and toxicity. Advanced Drug Delivery Reviews. 2005;57:2215-37.
[64] Greish K, Thiagarajan G, Herd H, Price R, Bauer H, Hubbard D, et al. Size and surface charge significantly influence the toxicity of silica and dendritic nanoparticles. Nanotoxicology. 2012;6:713-23.
[65] Thiagarajan G, Greish K, Ghandehari H. Charge affects the oral toxicity of poly(amidoamine) dendrimers. Eur J Pharm Biopharm. 2013;84:330-4.

[66] Kulhari H, Pooja D, Prajapati SK, Chauhan AS. Performance evaluation of PAMAM dendrimer based simvastatin formulations. International journal of pharmaceutics. 2011;405:203-9.
[67] Albertazzi L, Gherardini L, Brondi M, Sulis Sato S, Bifone A, Pizzorusso T, et al. In vivo distribution and toxicity of PAMAM dendrimers in the central nervous system depend on their surface chemistry. Mol Pharm. 2013;10:249-60.
[68] Heiden TCK, Dengler E, Kao WJ, Heideman W, Peterson RE. Developmental toxicity of low generation PAMAM dendrimers in zebrafish. Toxicol Appl Pharm. 2007;225:70-9.
[69] Malik N, Wiwattanapatapee R, Klopsch R, Lorenz K, Frey H, Weener JW, et al. Dendrimers: relationship between structure and biocompatibility in vitro, and preliminary studies on the biodistribution of 125I-labelled polyamidoamine dendrimers in vivo. Journal of controlled release : official journal of the Controlled Release Society. 2000;65:133-48.
[70] Schwartzbaum JA, Fisher JL, Aldape KD, Wrensch M. Epidemiology and molecular pathology of glioma. Nature clinical practice Neurology. 2006;2:494-503; quiz 1 p following 16.
[71] Bregy A, Shah AH, Diaz MV, Pierce HE, Ames PL, Diaz D, et al. The role of Gliadel wafers in the treatment of high-grade gliomas. Expert review of anticancer therapy. 2013;13:1453-61.
[72] Jain RK, Stylianopoulos T. Delivering nanomedicine to solid tumors. Nature reviews Clinical oncology. 2010;7:653-64.
[73] Rittierodt M, Harada K. Repetitive doxorubicin treatment of glioblastoma enhances the PGP expression--a special role for endothelial cells. Experimental and toxicologic pathology : official journal of the Gesellschaft fur Toxikologische Pathologie. 2003;55:39-44.
[74] Heath JR, Davis ME. Nanotechnology and cancer. Annual review of medicine. 2008;59:251-65.
[75] Cabral H, Matsumoto Y, Mizuno K, Chen Q, Murakami M, Kimura M, et al. Accumulation of sub-100 nm polymeric micelles in poorly permeable tumours depends on size. Nature nanotechnology. 2011;6:815-23.
[76] Wu W, Driessen W, Jiang XQ. Oligo(ethylene glycol)-Based Thermosensitive Dendrimers and Their Tumor Accumulation and Penetration. J Am Chem Soc. 2014;136:3145-55.
[77] Tang L, Gabrielson NP, Uckun FM, Fan TM, Cheng JJ. Size-Dependent Tumor Penetration and in Vivo Efficacy of Monodisperse Drug-Silica Nanoconjugates. Mol Pharm. 2013;10:883-92.
[78] Schadlich A, Caysa H, Mueller T, Tenambergen F, Rose C, Gopferich A, et al. Tumor Accumulation of NIR Fluorescent PEG PLA Nanoparticles: Impact of Particle Size and Human Xenograft Tumor Model. Acs Nano. 2011;5:8710-20.
[79] Tzeng SY, Green JJ. Therapeutic nanomedicine for brain cancer. Therapeutic delivery. 2013;4:687-704.
[80] Sarin H, Kanevsky AS, Wu H, Brimacombe KR, Fung SH, Sousa AA, et al. Effective transvascular delivery of nanoparticles across the blood-brain tumor barrier into malignant glioma cells. Journal of translational medicine. 2008;6:80.
[81] Sarin H. Recent progress towards development of effective systemic chemotherapy for the treatment of malignant brain tumors. Journal of translational medicine. 2009;7:77.
[82] Sarin H. Effective Transvascular Delivery of Chemotherapy into Cancer Cells with Imageable Nanoparticles in the 7 to 10 Nanometer Size Range. In: Slevin M, editor. Current Advances in the Medical Application of Nanotechnology: Bentham Science Publishers Ltd.; 2012. p. 10-24.
[83] Hobbs SK, Monsky WL, Yuan F, Roberts WG, Griffith L, Torchilin VP, et al. Regulation of transport pathways in tumor vessels: role of tumor type and microenvironment. Proc Natl Acad Sci U S A. 1998;95:4607-12.
[84] Mishra MK, Beaty CA, Lesniak WG, Kambhampati SR, Zhang F, Wilson MA, et al. Dendrimer Brain Uptake and Targeted Therapy for Brain Injury in a Large Animal Model of Hypothermic Circulatory Arrest. Acs Nano. 2014;8:2134-47.
[85] Sykova E, Nicholson C. Diffusion in brain extracellular space. Physiol Rev. 2008;88:1277-340.

[86] Kannan S, Dai H, Navath RS, Balakrishnan B, Jyoti A, Janisse J, et al. Dendrimer-based postnatal therapy for neuroinflammation and cerebral palsy in a rabbit model. Sci Transl Med. 2012;4:130ra46.
[87] El Andaloussi A, Sonabend AM, Han Y, Lesniak MS. Stimulation of TLR9 with CpG ODN enhances apoptosis of glioma and prolongs the survival of mice with experimental brain tumors. Glia. 2006;54:526-35.
[88] Hussain SF, Kong LY, Jordan J, Conrad C, Madden T, Fokt I, et al. A novel small molecule inhibitor of signal transducers and activators of transcription 3 reverses immune tolerance in malignant glioma patients. Cancer research. 2007;67:9630-6.
[89] Gabrusiewicz K, Ellert-Miklaszewska A, Lipko M, Sielska M, Frankowska M, Kaminska B. Characteristics of the alternative phenotype of microglia/macrophages and its modulation in experimental gliomas. PloS one. 2011;6:e23902.
[90] Markovic DS, Vinnakota K, van Rooijen N, Kiwit J, Synowitz M, Glass R, et al. Minocycline reduces glioma expansion and invasion by attenuating microglial MT1-MMP expression. Brain, behavior, and immunity. 2011;25:624-8.
[91] Dreaden EC, Mwakwari SC, Austin LA, Kieffer MJ, Oyelere AK, El-Sayed MA. Small molecule-gold nanorod conjugates selectively target and induce macrophage cytotoxicity towards breast cancer cells. Small. 2012;8:2819-22.
[92] Zhu SJ, Niu MM, O'Mary H, Cui ZR. Targeting of Tumor-Associated Macrophages Made Possible by PEG-Sheddable, Mannose-Modified Nanoparticles. Mol Pharm. 2013;10:3525-30.
[93] VanHandel M, Alizadeh D, Zhang L, Kateb B, Bronikowski M, Manohara H, et al. Selective uptake of multi-walled carbon nanotubes by tumor macrophages in a murine glioma model. J Neuroimmunol. 2009;208:3-9.
[94] Alizadeh D, Zhang L, Hwang J, Schluep T, Badie B. Tumor-associated macrophages are predominant carriers of cyclodextrin-based nanoparticles into gliomas. Nanomedicine : nanotechnology, biology, and medicine. 2010;6:382-90.
[95] Lesniak WG, Mishra MK, Jyoti A, Balakrishnan B, Zhang F, Nance E, et al. Biodistribution of fluorescently labeled PAMAM dendrimers in neonatal rabbits: effect of neuroinflammation. Mol Pharm. 2013;10:4560-71.
[96] Recinos VR, Tyler BM, Bekelis K, Sunshine SB, Vellimana A, Li KW, et al. Combination of intracranial temozolomide with intracranial carmustine improves survival when compared with either treatment alone in a rodent glioma model. Neurosurgery. 2010;66:530-7; discussion 7.
[97] Kamat M, El-Boubbou K, Zhu DC, Lansdell T, Lu X, Li W, et al. Hyaluronic acid immobilized magnetic nanoparticles for active targeting and imaging of macrophages. Bioconjug Chem. 2010;21:2128-35.
[98] Orr AG, Orr AL, Li XJ, Gross RE, Traynelis SF. Adenosine A(2A) receptor mediates microglial process retraction. Nat Neurosci. 2009;12:872-8.
[99] Komohara Y, Ohnishi K, Kuratsu J, Takeya M. Possible involvement of the M2 anti-inflammatory macrophage phenotype in growth of human gliomas. The Journal of pathology. 2008;216:15-24.
[100] Badie B, Schartner J. Role of microglia in glioma pathology. Microscopy research and technique. 2001:106-13.
[101] Roggendorf W, Strupp S, Paulus W. Distribution and characterization of microglia/macrophages in human brain tumors. Acta neuropathologica. 1996;92:288-93.
[102] Hussain SF, Yang D, Suki D, Aldape K, Grimm E, Heimberger AB. The role of human glioma-infiltrating microglia/macrophages in mediating antitumor immune responses. Neuro Oncol. 2006;8:261-79.
[103] Wohlfart S, Khalansky AS, Gelperina S, Begley D, Kreuter J. Kinetics of transport of doxorubicin bound to nanoparticles across the blood-brain barrier. Journal of controlled release : official journal of the Controlled Release Society. 2011;154:103-7.

[104] Noell S, Mayer D, Strauss WSL, Tatagiba MS, Ritz R. Selective enrichment of hypericin in malignant glioma: Pioneering in vivo results. Int J Oncol. 2011;38:1343-8.
[105] Dave N, Gudelsky GA, Desai PB. The pharmacokinetics of letrozole in brain and brain tumor in rats with orthotopically implanted C6 glioma, assessed using intracerebral microdialysis. Cancer chemotherapy and pharmacology. 2013;72:349-57.
[106] Wu W, Driessen W, Jiang X. Oligo(ethylene glycol)-based thermosensitive dendrimers and their tumor accumulation and penetration. J Am Chem Soc. 2014;136:3145-55.
[107] Lee CC, Gillies ER, Fox ME, Guillaudeu SJ, Frechet JM, Dy EE, et al. A single dose of doxorubicin-functionalized bow-tie dendrimer cures mice bearing C-26 colon carcinomas. Proc Natl Acad Sci U S A. 2006;103:16649-54.
[108] Brigger I, Morizet J, Laudani L, Aubert G, Appel M, Velasco V, et al. Negative preclinical results with stealth nanospheres-encapsulated Doxorubicin in an orthotopic murine brain tumor model. Journal of Controlled Release. 2004;100:29-40.
[109] Arnold RD, Mager DE, Slack JE, Straubinger RM. Effect of repetitive administration of doxorubicin-containing liposomes on plasma pharmacokinetics and drug biodistribution in a rat brain tumor model. Clin Cancer Res. 2005;11:8856-65.
[110] Chertok B, David AE, Moffat BA, Yang VC. Substantiating in vivo magnetic brain tumor targeting of cationic iron oxide nanocarriers via adsorptive surface masking. Biomaterials. 2009;30:6780-7.
[111] Siegal T. Which drug or drug delivery system can change clinical practice for brain tumor therapy? Neuro Oncol. 2013;15:656-69.
[112] Chauhan VP, Jain RK. Strategies for advancing cancer nanomedicine. Nature materials. 2013;12:958-62.
[113] Perrault SD, Walkey C, Jennings T, Fischer HC, Chan WCW. Mediating Tumor Targeting Efficiency of Nanoparticles Through Design. Nano Lett. 2009;9:1909-15.
[114] Wang K, Zhang X, Liu Y, Liu C, Jiang B, Jiang Y. Tumor penetrability and anti-angiogenesis using iRGD-mediated delivery of doxorubicin-polymer conjugates. Biomaterials. 2014;35:8735-47.
[115] Nance E, Zhang C, Shih TY, Xu Q, Schuster BS, Hanes J. Brain-penetrating nanoparticles improve paclitaxel efficacy in malignant glioma following local administration. Acs Nano. 2014;8:10655-64.
[116] Yoshii Y, Sugiyama K. Intercapillary distance in the proliferating area of human glioma. Cancer research. 1988;48:2938-41.
[117] Bax M, Goldstein M, Rosenbaum P, Leviton A, Paneth N, Dan B, et al. Proposed definition and classification of cerebral palsy, April 2005. Developmental medicine and child neurology. 2005;47:571-6.
[118] Koman LA, Smith BP, Shilt JS. Cerebral palsy. Lancet. 2004;363:1619-31.
[119] Centers for Disease C, Prevention. Economic costs associated with mental retardation, cerebral palsy, hearing loss, and vision impairment--United States, 2003. MMWR Morbidity and mortality weekly report. 2004;53:57-9.
[120] Stoll BJ, Hansen NI, Bell EF, Shankaran S, Laptook AR, Walsh MC, et al. Neonatal Outcomes of Extremely Preterm Infants From the NICHD Neonatal Research Network. Pediatrics. 2010;126:443-56.
[121] Pakula AT, Braun KV, Yeargin-Allsopp M. Cerebral Palsy: Classification and Epidemiology. Phys Med Rehabil Cli. 2009;20:427-+.
[122] Haynes RL, Baud O, Li J, Kinney HC, Volpe JJ, Folkerth RD. Oxidative and nitrative injury in periventricular leukomalacia: A review. Brain Pathol. 2005;15:225-33.
[123] Hagberg H, Gressens P, Mallard C. Inflammation during fetal and neonatal life: implications for neurologic and neuropsychiatric disease in children and adults. Ann Neurol. 2012;71:444-57.
[124] Balakrishnan B, Nance E, Johnston MV, Kannan R, Kannan S. Nanomedicine in cerebral palsy. Int J Nanomed. 2013;8:4183-95.
[125] Dai H, Navath RS, Balakrishnan B, Guru BR, Mishra MK, Romero R, et al. Intrinsic targeting of inflammatory cells in the brain by polyamidoamine dendrimers upon subarachnoid administration. Nanomedicine : nanotechnology, biology, and medicine. 2010;5:1317-29.

[126] Kannan S, Dai H, Navath RS, Balakrishnan B, Jyoti A, Janisse J, et al. Dendrimer-Based Postnatal Therapy for Neuroinflammation and Cerebral Palsy in a Rabbit Model. Sci Transl Med. 2012;4.
[127] Tita AT, Andrews WW. Diagnosis and management of clinical chorioamnionitis. Clin Perinatol. 2010;37:339-54.
[128] Sadekar S, Thiagarajan G, Bartlett K, Hubbard D, Ray A, McGill LD, et al. Poly(amido amine) dendrimers as absorption enhancers for oral delivery of camptothecin. International journal of pharmaceutics. 2013;456:175-85.
[129] Burd I, Zhang F, Dada T, Mishra MK, Borbiev T, Lesniak WG, et al. Fetal uptake of intra-amniotically delivered dendrimers in a mouse model of intrauterine inflammation and preterm birth. Nanomedicine : nanotechnology, biology, and medicine. 2014;10:1343-51.
[130] Thiagarajan G, Sadekar S, Greish K, Ray A, Ghandehari H. Evidence of Oral Translocation of Anionic G6.5 Dendrimers in Mice. Mol Pharmaceut. 2013;10:988-98.
[131] Hubbard D, Ghandehari H, Brayden DJ. Transepithelial Transport of PAMAM Dendrimers across Isolated Rat Jejunal Mucosae in Ussing Chambers. Biomacromolecules. 2014;15:2889-95.
[132] Sadekar S, Ghandehari H. Transepithelial transport and toxicity of PAMAM dendrimers: Implications for oral drug delivery. Adv Drug Deliver Rev. 2012;64:571-88.
[133] Cornford EM, Cornford ME. Nutrient transport and the blood-brain barrier in developing animals. Fed Proc. 1986;45:2065-72.
[134] Cornford EM, Braun LD, Oldendorf WH. Developmental Modulations of Blood-Brain Barrier Permeability as an Indicator of Changing Nutritional Requirements in the Brain. Pediatr Res. 1982;16:324-8.
[135] Saadani-Makki F, Kannan S, Lu X, Janisse J, Dawe E, Edwin S, et al. Intrauterine administration of endotoxin leads to motor deficits in a rabbit model: a link between prenatal infection and cerebral palsy. Am J Obstet Gynecol. 2008;199.
[136] Thiagarajan G, Sadekar S, Greish K, Ray A, Ghandehari H. Evidence of oral translocation of anionic G6.5 dendrimers in mice. Mol Pharm. 2013;10:988-98.
[137] Yang Y, Sunoqrot S, Stowell C, Ji J, Lee CW, Kim JW, et al. Effect of size, surface charge, and hydrophobicity of poly(amidoamine) dendrimers on their skin penetration. Biomacromolecules. 2012;13:2154-62.
[138] Bicker J, Alves G, Fortuna A, Falcao A. Blood-brain barrier models and their relevance for a successful development of CNS drug delivery systems: A review. Eur J Pharm Biopharm. 2014;87:409-32.
[139] Saadani-Makki F, Kannan S, Makki M, Muzik O, Janisse J, Romero R, et al. Intrauterine endotoxin administration leads to white matter diffusivity changes in newborn rabbits. J Child Neurol. 2009;24:1179-89.
[140] Balakrishnan B, Nance E, Johnston MV, Kannan R, Kannan S. Nanomedicine in cerebral palsy. Int J Nanomedicine. 2013;8:4183-95.
[141] Kreutzberg GW. Microglia: A sensor for pathological events in the CNS. Trends Neurosci. 1996;19:312-8.
[142] Stoll G, Jander S. The role of microglia and macrophages in the pathophysiology of the CNS. Prog Neurobiol. 1999;58:233-47.
[143] Kettenmann H, Hanisch UK, Noda M, Verkhratsky A. Physiology of microglia. Physiological reviews. 2011;91:461-553.
[144] Nimmerjahn A, Kirchhoff F, Helmchen F. Resting microglial cells are highly dynamic surveillants of brain parenchyma in vivo. Science. 2005;308:1314-8.
[145] Stence N, Waite M, Dailey ME. Dynamics of microglial activation: a confocal time-lapse analysis in hippocampal slices. Glia. 2001;33:256-66.

[146] Nolte C, Moller T, Walter T, Kettenmann H. Complement 5a controls motility of murine microglial cells in vitro via activation of an inhibitory G-protein and the rearrangement of the actin cytoskeleton. Neuroscience. 1996;73:1091-107.
[147] Loane DJ, Byrnes KR. Role of microglia in neurotrauma. Neurotherapeutics. 2010;7:366-77.
[148] Mannix RC, Whalen MJ. Traumatic brain injury, microglia, and Beta amyloid. Int J Alzheimers Dis. 2012;2012:608732.
[149] Lively S, Schlichter LC. The microglial activation state regulates migration and roles of matrix-dissolving enzymes for invasion. J Neuroinflammation. 2013;10:75.
[150] Orr AG, Orr AL, Li XJ, Gross RE, Traynelis SF. Adenosine A(2A) receptor mediates microglial process retraction. Nat Neurosci. 2009;12:872-U84.
[151] De Simone R, Niturad CE, De Nuccio C, Ajmone-Cat MA, Visentin S, Minghetti L. TGF-beta and LPS modulate ADP-induced migration of microglial cells through P2Y1 and P2Y12 receptor expression. Journal of Neurochemistry. 2010;115:450-9.
[152] Brown GC, Neher JJ. Microglial phagocytosis of live neurons. Nature reviews Neuroscience. 2014;15:209-16.
[153] Biber K, Owens T, Boddeke E. What is microglia neurotoxicity (Not)? Glia. 2014;62:841-54.
[154] Block ML, Zecca L, Hong JS. Microglia-mediated neurotoxicity: uncovering the molecular mechanisms. Nature reviews Neuroscience. 2007;8:57-69.
[155] Indaram M, Ma W, Zhao L, Fariss RN, Rodriguez IR, Wong WT. 7-Ketocholesterol Increases Retinal Microglial Migration, Activation, and Angiogenicity: A Potential Pathogenic Mechanism Underlying Age-related Macular Degeneration. Scientific reports. 2015;5:9144.
[156] Kannan S, Saadani-Makki F, Balakrishnan B, Dai H, Chakraborty PK, Janisse J, et al. Decreased cortical serotonin in neonatal rabbits exposed to endotoxin in utero. Journal of cerebral blood flow and metabolism : official journal of the International Society of Cerebral Blood Flow and Metabolism. 2011;31:738-49.
[157] Nance EA, Woodworth GF, Sailor KA, Shih TY, Xu Q, Swaminathan G, et al. A dense poly(ethylene glycol) coating improves penetration of large polymeric nanoparticles within brain tissue. Sci Transl Med. 2012;4:149ra19.
[158] Rao SM, Lin ZL, Drobyshevsky A, Chen LN, Ji XH, Ji HT, et al. Involvement of Neuronal Nitric Oxide Synthase in Ongoing Fetal Brain Injury following Near-Term Rabbit Hypoxia-Ischemia. Dev Neurosci-Basel. 2011;33:288-98.
[159] Su T, Paradiso B, Long YS, Liao WP, Simonato M. Evaluation of cell damage in organotypic hippocampal slice culture from adult mouse: a potential model system to study neuroprotection. Brain research. 2011;1385:68-76.
[160] Kannan S, Saadani-Makki F, Muzik O, Chakraborty P, Mangner TJ, Janisse J, et al. Microglial activation in perinatal rabbit brain induced by intrauterine inflammation: detection with 11C-(R)-PK11195 and small-animal PET. Journal of nuclear medicine : official publication, Society of Nuclear Medicine. 2007;48:946-54.
[161] Fraley SI, Feng Y, Krishnamurthy R, Kim DH, Celedon A, Longmore GD, et al. A distinctive role for focal adhesion proteins in three-dimensional cell motility. Nature cell biology. 2010;12:598-604.
[162] Cho S, Wood A, Bowlby MR. Brain slices as models for neurodegenerative disease and screening platforms to identify novel therapeutics. Current neuropharmacology. 2007;5:19-33.
[163] Tamashiro TT, Dalgard CL, Byrnes KR. Primary microglia isolation from mixed glial cell cultures of neonatal rat brain tissue. Journal of visualized experiments : JoVE. 2012:e3814.
[164] Smithpeter CL, Dunn AK, Welch AJ, Richards-Kortum R. Penetration depth limits of in vivo confocal reflectance imaging. Applied optics. 1998;37:2749-54.
[165] Dailey ME, Eyo U, Fuller L, Hass J, Kurpius D. Imaging microglia in brain slices and slice cultures. Cold Spring Harbor protocols. 2013;2013:1142-8.

[166] Dailey ME, Waite M. Confocal imaging of microglial cell dynamics in hippocampal slice cultures. Methods. 1999;18:222-30, 177.
[167] van Rossum D, Hanisch UK. Microglia. Metabolic brain disease. 2004;19:393-411.
[168] Carbonell WS, Murase S, Horwitz AF, Mandell JW. Migration of perilesional microglia after focal brain injury and modulation by CC chemokine receptor 5: an in situ time-lapse confocal imaging study. The Journal of neuroscience : the official journal of the Society for Neuroscience. 2005;25:7040-7.
[169] Sieger D, Moritz C, Ziegenhals T, Prykhozhij S, Peri F. Long-range Ca2+ waves transmit brain-damage signals to microglia. Developmental cell. 2012;22:1138-48.
[170] Dibaj P, Nadrigny F, Steffens H, Scheller A, Hirrlinger J, Schomburg ED, et al. NO Mediates Microglial Response to Acute Spinal Cord Injury Under ATP Control In Vivo. Glia. 2010;58:1133-44.
[171] Petersen MA, Dailey ME. Diverse microglial motility behaviors during clearance of dead cells in hippocampal slices. Glia. 2004;46:195-206.
[172] Liu HC, Zheng MH, Du YL, Wang L, Kuang F, Qin HY, et al. N9 microglial cells polarized by LPS and IL4 show differential responses to secondary environmental stimuli. Cell Immunol. 2012;278:84-90.
[173] Chhor V, Le Charpentier T, Lebon S, Ore MV, Celador IL, Josserand J, et al. Characterization of phenotype markers and neuronotoxic potential of polarised primary microglia in vitro. Brain, behavior, and immunity. 2013;32:70-85.
[174] Block ML, Zecca L, Hong JS. Microglia-mediated neurotoxicity: uncovering the molecular mechanisms. Nature Reviews Neuroscience. 2007;8:57-69.
[175] Chang WK, Carmona-Fontaine C, Xavier JB. Tumour-stromal interactions generate emergent persistence in collective cancer cell migration. Interface focus. 2013;3:20130017.
[176] Dujardin DL, Barnhart LE, Stehman SA, Gomes ER, Gundersen GG, Vallee RB. A role for cytoplasmic dynein and LIS1 in directed cell movement. The Journal of cell biology. 2003;163:1205-11.
[177] Danen EHJ, van Rheenen J, Franken W, Huveneers S, Sonneveld P, Jalink K, et al. Integrins control motile strategy through a Rho-cofilin pathway. Journal of Cell Biology. 2005;169:515-26.
[178] Weiner OD. Regulation of cell polarity during eukaryotic chemotaxis: the chemotactic compass. Curr Opin Cell Biol. 2002;14:196-202.
[179] Milner R, Campbell IL. The integrin family of cell adhesion molecules has multiple functions within the CNS. Journal of Neuroscience Research. 2002;69:286-91.
[180] Milner R, Campbell IL. The extracellular matrix and cytokines regulate microglial integrin expression and activation. Journal of immunology. 2003;170:3850-8.
[181] Pickard MR, Chari DM. Robust uptake of magnetic nanoparticles (MNPs) by central nervous system (CNS) microglia: implications for particle uptake in mixed neural cell populations. International journal of molecular sciences. 2010;11:967-81.
[182] Kambhampati SP, Clunies-Ross AJ, Bhutto I, Mishra MK, Edwards M, McLeod DS, et al. Systemic and Intravitreal Delivery of Dendrimers to Activated Microglia/Macrophage in Ischemia/Reperfusion Mouse Retina. Invest Ophthalmol Vis Sci. 2015;56:4413-24.
[183] Zhang F, Mastorakos P, Mishra MK, Mangraviti A, Hwang L, Zhou J, et al. Uniform brain tumor distribution and tumor associated macrophage targeting of systemically administered dendrimers. Biomaterials. 2015;52:507-16.
[184] Hayder M, Varilh M, Turrin CO, Saoudi A, Caminade AM, Poupot R, et al. Phosphorus-Based Dendrimer ABP Treats Neuroinflammation by Promoting IL-10-Producing CD4 T Cells. Biomacromolecules. 2015.
[185] Boridy S, Soliman GM, Maysinger D. Modulation of inflammatory signaling and cytokine release from microglia by celastrol incorporated into dendrimer nanocarriers. Nanomedicine (Lond). 2012;7:1149-65.
[186] Wong HL, Wu XY, Bendayan R. Nanotechnological advances for the delivery of CNS therapeutics. Adv Drug Deliver Rev. 2012;64:686-700.

[187] Pardridge WM. The blood-brain barrier: bottleneck in brain drug development. NeuroRx. 2005;2:3-14.
[188] van Tellingen O, Yetkin-Arik B, de Gooijer MC, Wesseling P, Wurdinger T, de Vries HE. Overcoming the blood-brain tumor barrier for effective glioblastoma treatment. Drug Resist Updat. 2015;19:1-12.
[189] Thorne RG, Nicholson C. In vivo diffusion analysis with quantum dots and dextrans predicts the width of brain extracellular space. Proc Natl Acad Sci U S A. 2006;103:5567-72.
[190] Nance E, Porambo M, Zhang F, Mishra MK, Buelow M, Getzenberg R, et al. Systemic dendrimer-drug treatment of ischemia-induced neonatal white matter injury. Journal of controlled release : official journal of the Controlled Release Society. 2015;214:112-20.
[191] Kannan S, Saadani-Makki F, Balakrishnan B, Chakraborty P, Janisse J, Lu X, et al. Magnitude of [(11)C]PK11195 binding is related to severity of motor deficits in a rabbit model of cerebral palsy induced by intrauterine endotoxin exposure. Dev Neurosci. 2011;33:231-40.
[192] Saadani-Makki F, Kannan S, Lu X, Janisse J, Dawe E, Edwin S, et al. Intrauterine administration of endotoxin leads to motor deficits in a rabbit model: a link between prenatal infection and cerebral palsy. American journal of obstetrics and gynecology. 2008;199:651 e1-7.
[193] Tang L, Yang X, Yin Q, Cai K, Wang H, Chaudhury I, et al. Investigating the optimal size of anticancer nanomedicine. Proc Natl Acad Sci U S A. 2014;111:15344-9.
[194] Weissleder R, Nahrendorf M, Pittet MJ. Imaging macrophages with nanoparticles. Nat Mater. 2014;13:125-38.
[195] Sadekar S, Linares O, Noh G, Hubbard D, Ray A, Janat-Amsbury M, et al. Comparative Pharmacokinetics of Pamam-Oh Dendrimers and Hpma Copolymers in Ovarian-Tumor-Bearing Mice. Drug Deliv Transl Res. 2013;3:260-71.
[196] Win-Shwe TT, Sone H, Kurokawa Y, Zeng Y, Zeng Q, Nitta H, et al. Effects of PAMAM dendrimers in the mouse brain after a single intranasal instillation. Toxicol Lett. 2014;228:207-15.
[197] Wang SF, Li YB, Fan JJ, Wang ZY, Zeng X, Sun Y, et al. The role of autophagy in the neurotoxicity of cationic PAMAM dendrimers. Biomaterials. 2014;35:7588-97.
[198] Tilleux S, Hermans E. Neuroinflammation and regulation of glial glutamate uptake in neurological disorders. J Neurosci Res. 2007;85:2059-70.
[199] Frank-Cannon TC, Alto LT, McAlpine FE, Tansey MG. Does neuroinflammation fan the flame in neurodegenerative diseases? Mol Neurodegener. 2009;4.
[200] Dong XX, Wang Y, Qin ZH. Molecular mechanisms of excitotoxicity and their relevance to pathogenesis of neurodegenerative diseases. Acta Pharmacol Sin. 2009;30:379-87.
[201] Maragakis NJ, Rothstein JD. Mechanisms of Disease: astrocytes in neurodegenerative disease. Nat Clin Pract Neurol. 2006;2:679-89.
[202] Cavaletti G, Slusher B. Regulation of glutamate synthesis via inhibition of glutamate carboxypeptidase II (GCPII): an effective method to treat central and peripheral nervous system disorders. Current medicinal chemistry. 2012;19:1259-60.
[203] Wozniak KM, Wu Y, Vornov JJ, Lapidus R, Rais R, Rojas C, et al. The orally active glutamate carboxypeptidase II inhibitor E2072 exhibits sustained nerve exposure and attenuates peripheral neuropathy. The Journal of pharmacology and experimental therapeutics. 2012;343:746-54.
[204] Carozzi VA, Ceresa C. The role of glutamate in diabetic and in chemotherapy induced peripheral neuropathies and its regulation by glutamate carboxypeptidase II. Current medicinal chemistry. 2012;19:1261-8.
[205] Barinka C, Rojas C, Slusher B, Pomper M. Glutamate carboxypeptidase II in diagnosis and treatment of neurologic disorders and prostate cancer. Current medicinal chemistry. 2012;19:856-70.
[206] Zhou J, Neale JH, Pomper MG, Kozikowski AP. NAAG peptidase inhibitors and their potential for diagnosis and therapy. Nature reviews Drug discovery. 2005;4:1015-26.

[207] Ali SS, Hardt JI, Dugan LL. SOD Activity of carboxyfullerenes predicts their neuroprotective efficacy: a structure-activity study. Nanomed-Nanotechnol. 2008;4:283-94.
[208] Dugan LL, Gabrielsen JK, Yu SP, Lin TS, Choi DW. Buckminsterfullerenol free radical scavengers reduce excitotoxic and apoptotic death of cultured cortical neurons. Neurobiol Dis. 1996;3:129-35.
[209] Jin H, Chen WQ, Tang XW, Chiang LY, Yang CY, Schloss JV, et al. Polyhydroxylated C(60), fullerenols, as glutamate receptor antagonists and neuroprotective agents. J Neurosci Res. 2000;62:600-7.
[210] Kim JH, Kim GH, Jeong JH, Lee IH, Lee YJ, Lee NS, et al. Neuroprotective Effect of Estradiol-Loaded Poly(lactic-co-glycolic acid) Nanoparticles on Glutamate-Induced Excitotoxic Neuronal Death. J Nanosci Nanotechno. 2014;14:8390-7.
[211] Kannan RM, Nance E, Kannan S, Tomalia DA. Emerging concepts in dendrimer-based nanomedicine: from design principles to clinical applications. J Intern Med. 2014;276:579-617.
[212] Lee CC, MacKay JA, Frechet JM, Szoka FC. Designing dendrimers for biological applications. Nat Biotechnol. 2005;23:1517-26.
[213] Kurtoglu YE, Navath RS, Wang B, Kannan S, Romero R, Kannan RM. Poly(amidoamine) dendrimer-drug conjugates with disulfide linkages for intracellular drug delivery. Biomaterials. 2009;30:2112-21.
[214] Saito G, Swanson JA, Lee KD. Drug delivery strategy utilizing conjugation via reversible disulfide linkages: role and site of cellular reducing activities. Adv Drug Deliv Rev. 2003;55:199-215.
[215] Duncan R, Izzo L. Dendrimer biocompatibility and toxicity. Adv Drug Deliv Rev. 2005;57:2215-37.
[216] Derrick M, Luo NL, Bregman JC, Jilling T, Ji X, Fisher K, et al. Preterm fetal hypoxia-ischemia causes hypertonia and motor deficits in the neonatal rabbit: a model for human cerebral palsy? The Journal of neuroscience : the official journal of the Society for Neuroscience. 2004;24:24-34.
[217] Zhang Z, Saraswati M, Koehler RC, Robertson C, Kannan S. A New Rabbit Model of Pediatric Traumatic Brain Injury. Journal of neurotrauma. 2015.
[218] Vornov JJ, Wozniak KM, Wu Y, Rojas C, Rais R, Slusher BS. Pharmacokinetics and pharmacodynamics of the glutamate carboxypeptidase II inhibitor 2-MPPA show prolonged alleviation of neuropathic pain through an indirect mechanism. The Journal of pharmacology and experimental therapeutics. 2013;346:406-13.
[219] Rais R, Hoover R, Wozniak K, Rudek MA, Tsukamoto T, Alt J, et al. Reversible disulfide formation of the glutamate carboxypeptidase II inhibitor E2072 results in prolonged systemic exposures in vivo. Drug metabolism and disposition: the biological fate of chemicals. 2012;40:2315-23.
[220] Li Y, Zhu H, Wang S, Qian X, Fan J, Wang Z, et al. Interplay of Oxidative Stress and Autophagy in PAMAM Dendrimers-Induced Neuronal Cell Death. Theranostics. 2015;5:1363-77.
[221] Majer P, Jackson PF, Delahanty G, Grella BS, Ko YS, Li W, et al. Synthesis and biological evaluation of thiol-based inhibitors of glutamate carboxypeptidase II: discovery of an orally active GCP II inhibitor. J Med Chem. 2003;46:1989-96.
[222] Neale JH, Olszewski RT, Zuo D, Janczura KJ, Profaci CP, Lavin KM, et al. Advances in understanding the peptide neurotransmitter NAAG and appearance of a new member of the NAAG neuropeptide family. J Neurochem. 2011;118:490-8.
[223] Tsukamoto T, Wozniak KM, Slusher BS. Progress in the discovery and development of glutamate carboxypeptidase II inhibitors. Drug Discov Today. 2007;12:767-76.
[224] Berger UV, Luthi-Carter R, Passani LA, Elkabes S, Black I, Konradi C, et al. Glutamate carboxypeptidase II is expressed by astrocytes in the adult rat nervous system. J Comp Neurol. 1999;415:52-64.

# FAN ZHANG

Email: fzhang18@jhu.edu 400 N. Broadway, Smith Building, 6001
Phone: (313) 452-3438
Baltimore, MD 21231

**EDUCATION/TRAINING**

**Ph.D., Materials Science & Engineering,** The Johns Hopkins University, Baltimore, USA — Expected 05.2016

# FAN ZHANG

Email: fzhang18@jhu.edu
Phone: (313) 452-3438
400 N. Broadway, Smith Building, 6001
Baltimore, MD 21231

**EDUCATION/TRAINING**

**Ph.D., Materials Science & Engineering,** The Johns Hopkins University, Baltimore, USA 2016

**B.E., Materials Science & Engineering,** Donghua University, Shanghai, China 2010

Honors: Outstanding Student, Top 10 GPA

## II. RESEARCH EXPERIENCE

2011-current Ph.D. Candidate, Materials Science and Engineering
Center for Nanomedicine, Johns Hopkins School of Medicine, Baltimore, MD
Advisor: Rangaramanujam M. Kannan, Ph.D.

Thesis: Dendrimer Based Targeted Therapy for CNS Disorders

- Determined the mechanism of how polyamidoamine (PAMAM) dendrimers intrinsically target neuroinflammation at global (systemic) and local (tissue and cell) levels in a spectrum of neurological disorders using an integrative engineering approach. This knowledge builds the guiding principles for designing nanomedicine that can efficiently target and resolve neuroinflammation.
- Studied dendrimer kinetics and uptake mechanisms in multiple models ranging from small rodents (mice, rats and rabbits) to a more human-representative large animal (canine). These studies enabled understanding in translating nanomedicine from research into clinics.
- Developed a novel *ex vivo* system using neuroscience and immunology appro aches which addresses the role of 'activated' microglial cells as the major CNS innate immune cells in neuroinflammation by studying their ability to migrate and phagocytose dendrimers.
- Engineered dendrimer-based intravenous therapeutics (Doxorubicin, GCPII inhibitor, MEK pathway inhibitor, etc.) that can target activated microglia/macrophages in multiple disease models through bio-conjugation chemistry, and achieved controlled release triggered by glutathione concentration and pH level.

**Highlights of lab experience**

- Collaborated with research teams composed of researchers from multiple field s, including neurosurgery, cardiac surgery, engineering, neurology and neuroscience.
- Developed key research results that formed the basis of more than $4 million successful NIH-based research funds (R01) and other research funding sources.
- Led and mentored 4 students including master, undergraduate, and high school students in developing dendrimer based therapies for various

neurological diseases.

**III. PUBLICATIONS** * *Equal contribution*

**Peer reviewed**

[1] **Zhang F**, Nance E, Alnasser Y, Kannan RM, Kannan S. Microglia migration and interactions with dendrimer in brain in the presence of neuroinflammation. J Neuroinflammation. *accepted*

[2] **Zhang F***, Lin YA*, Kannan S, Kannan RM, Targeting Specific Cells in the Brain with Nanomedicines for CNS Therapies. J Control Release. 2015. pii: S0168-3659(15)30265-0.

[3] Nance E, Porambo M, **Zhang F**, Mishra MK, Buelow M, Getzenberg R, Johnston M, Kannan RM, Fatemi A, Kannan S. Systemic dendrimer-drug treatment of ischemia-induced neonatal white matter injury. J Control Release. 2015. 214:112-20.

[4] **Zhang F***, Mastorakos P*, Mishra M, Mangraviti A, Hwang L, Zhou J, Hanes J, Brem H, Olivi A, Tyler B, Kannan RM. PAMAM Dendrimer Biodistribution in Glioblastoma and Intrinsic Targeting of Tumor Associated Macrophages. Biomaterials. 2015. 52:507-16.

[5] Burd I*, **Zhang F***, Dada T, Mishra MK, Borbiev T, Lesniak WG, Baghlaf H, Kannan S, Kannan RM. Fetal uptake of intra-amniotically delivered dendrimers in a mouse model of intrauterine inflammation and preterm birth. Nanomedicine. 2014. 10(6):1343-51.

[6] Mishra MK, Beaty CA, Lesniak WG, Kambhampati SP, **Zhang F**, Wilson MA, Blue ME, Troncoso JC, Kannan S, Johnston MV, Baumgartner WA, Kannan RM. Dendrimer brain uptake and targeted therapy for brain injury in a large animal model of hypothermic circulatory arrest. ACS Nano. 2014. 8:2134-47.

[7] Lesniak WG, Mishra MK, Jyoti A, Balakrishnan B, **Zhang F**, Nance E, Romero R, Kannan S, Kannan RM. Biodistribution of fluorescently labeled PAMAM dendrimers in neonatal rabbits: effect of neuroinflammation. Mol Pharm. 2013. 10:4560-71.

[8] SK UH, Kambhampati SP, Mishra MK, Lesniak WG, **Zhang F**, Kannan RM. Enhancing the efficacy of Ara-C through conjugation with PAMAM dendrimer and linear PEG: a comparative study. Biomacromolecules. 2013. 14:801-10.

[9] **Zhang F**, Nance E, Jasty V, Mishra MK, Kambhampati SP, Zhang Z, Kannan RM, Kannan S. Surface functionality affects the biodistribution and targeting to neuroinflammation for intra-amniotically delivered dendrimers. J. *under revision*

[10] Nance E, **Zhang F**, Mishra M, Zhang Z, Kambhampati SP, In vivo mechanism of dendrimer-mediated delivery in pediatric brain disorders. Biomaterials. *under review*

**Manuscript in submission (Papers written, to be submitted)**

[11] **Zhang F***, Zhang Z*, Alt J, Kambhampati SP, Nance E, Rojas C, Slusher B, Kannan RM, Kannan S. Dendrimer-GCPII Inhibitor Decreases Neuroinflammation and Glutamate Excitotoxicity in a Rabbit Model of Cerebral Palsy. *Manuscript in preparation.*

[12] Grimm JC*, **Zhang F***, Beaty CA, Mishra MK, Magruder JT, Kannan R, Shah A, The injury-targeted accumulation and cellular localization of dendrimer particles in an ex-vivo ischemia- reperfusion model of acute lung injury. *Manuscript in submission.*

[13] Balakrishnan B, Mishra MK, **Zhang F**, Eberhart C, Romero R, Kannan RM, Kannan S. In vivo toxicity of hydroxyl-functionalized PAMAM dendrimers in neonatal rabbit kits. *Manuscript in submission.*

[14] Alnasser Y, Kambampatti SP, Nance E, **Zhang F**, Rajbhandari L, Shrestha S,

Venkatesan A, Kannan RM, Kannan S. Mechanisms of cellular uptake of dendrimer based nanodevices by primary glial cells.

[15] Nemeth CL, Drummond GT, Mishra MK, **Zhang F**, Carr P, Kannan RM, Fatemi A, Johnston MV, Kannan S, Wilson MA. Quantitative assessment of biodistribution and dendrimer-drug uptake in a neonatal mouse model of hypoxic-ischemic encephalopathy. *Manuscript in preparation.*

## IV. PATENTS

[1] Kannan RM, Tyler B, **Zhang F**, Mastorakos P, Mishra M, Mangraviti A. APPROACHES FOR SYSTEMIC TARGETING OF TUMOR MACROPHAGES IN BRAIN TUMORS, U.S. Provisional Application (P13214-01), 2014, filed at The Johns Hopkins University. *Licensed*

[2] Kannan RM, Kannan, S, Nance E, Blue M, Johnston M, Baumgartner W, **Zhang F**, Wilson MA, Slusher B. DENDRIMER-DRUG DELIVERY SYSTEMS FOR TREATMENT OF RETT SYNDROME AND CNS DISORDERS, U.S. Provisional Application (JHU C13169), 2015, filed at The Johns Hopkins University. *Licensed*

[3] Kannan RM, Kannan, S, Fatemi A, **Zhang F**, Turk B. NANOPARTICLES FOR THE TREATMENT OF LEUKODYSTROPHIES INCLUDING X-LINKED ADRENOLEUKODYSTROPHY, U.S. Provisional Application (JHU C13801), 2015, filed at The Johns Hopkins University.

[4] Kannan RM, Hackam D, Kannan S, Nino DF, **Zhang F**. NANOPARTICLES FOR THE DIAGNOSIS AND TREATMENT OF NEONATAL NECROTIZING ENTEROCOLITIS, Provisional Application (JHU C13800), 2015, filed at The Johns Hopkins University.

## V. SELECTED PRESENTATIONS

[1] **Zhang F**, Mastorakos P, Mishra M, Mangraviti A, Hwang L, Zhou J, Hanes J, Brem H, Olivi A, Tyler B, Kannan RM *Dendrimer based systemic therapies for the treatment of Glioblastoma.* Poster session, September, 2015, Seattle, USA

[2] **Zhang F**, Mastorakos P, Mishra M, Mangraviti A, Hwang L, Zhou J, Hanes J, Brem H, Olivi A, Tyler B, Kannan RM *Dendrimer based systemic therapies for the treatment of Glioblastoma.* Poster session, The Johns Hopkins University Nano-Bio Symposium, April, 2015, Baltimore, USA

[3] **Zhang F**, Nance E, Alnasser Y, Kannan RM, Kannan S. *Microglia migration and interactions with dendrimer in brain in the presence of neuroinflammation*. Poster session, Biomedical Engineering Society Annual Meeting, Oct, 2014, San Antonio, USA.

[4] **Zhang F**, Nance E, Alnasser Y, Kannan RM, Kannan S. *Microglia migration and interactions with dendrimer in brain in the presence of neuroinflammation.* Poster session, Society of Neuroscience Conference, Nov. 2014, Washington DC. USA

[5] Nance E, **Zhang F**, Balakrishnan B, Mishra M, Kambhampati SP. *Mechanism of Nanoparticle-mediated Therapeutic Delivery in a Rabbit Model of Cerebral Palsy.* Poster session, Society of Neuroscience Conference, Nov. 2014, Washington DC. USA

[6] **Zhang F**, Nance E, Alnasser Y, Kannan RM, Kannan S. *Study of Microglia Movement and Interactions in Brain Slice of Cerebral Palsy Rabbit Model.* Poster session, Pediatric Academic Societies Annual Meeting, May, 2014, Vancouver, Canada

[7] Kannan S, Mishra M, Nance E, **Zhang F**, Kannan RM. *Mechanisms of Nanoparticle Uptake in Neuroinflammation-induced Pediatric Brian Injury.* Poster session, Society of Critical Care Medicine Annual Conference, 2014, San Francisco, USA. ***Annual Scientific Award***

[8] **Zhang F**, Nance E, Alnasser Y, Kannan RM, Kannan S. *Microglia migration and interactions with dendrimer in brain in the presence of neuroinflammation.* Poster session, Johns Hopkins Anesthesiology & Critical Care Medicine Annual Meeting, November, 2013, Baltimore, USA

## VI. TEACHING/MENTORING

01/2015-05/2015 Teaching assistant, The Johns Hopkins University, USA
Course: Micro-and Nano Structured Materials and Devices

01/2013-05/2014 Teaching assistant, The Johns Hopkins University, USA
Course: Modern Alchemy

08/2010-05/2011 Teaching assistant, Wayne State University, USA
Course: Fundamentals of Material Science and Engineering.

- Led scheduling and lecturing the lab section of the course (scheduling the whole curriculum, drafting the lecture notes, lab manual, preparing and maintaining lab equipment).

Mentored one graduate student (Jiangyu Li, 01/2015-now), two undergraduate students (Venkatasai Jasty, 01/2014-10/2014; Josiah Yu, 05/2014-09/2014) and one high school student (Fredrick Eisenbiegler, 07/2015-08/2015) for their research in Professor Rangaramanujam M. Kannan's lab.

## VII. HONORS/AWARDS

[1] Donghua Scholarship (equivalent to Outstanding Student), **2009**, Shanghai, China
[2] Outstanding Scientific and Technological Innovation and Research, **2009**, Shanghai, China
[3] Academic Excellence Award, **2007 and 2008** ***2 consecutive times***, Shanghai, China

## VIII. RESEARCH FUNDING

*Experimental contributions to the following successful funded grants:*

9/1/2014-6/30/2018 NIH/NHLBI2R01HL091541-20 (Baumgartner & Kannan)

*Excitotoxicity in circulatory arrest-brain injury*
12/1/2013-11/30/2014 Astra Zeneca Corporation AstraZeneca116601 (Kannan & Tyler)

*Dendrimer-based therapies targeted to tumor-associated macrophages in Glioma*

## IX. PROFESSIONAL AFFILIATIONS

Biomedical Engineering Society, 2014-present
Society of Neuroscience, 2014-present
American Society for Nanomedicine, 2015-present

## X. JOURNAL REVIEWS

*Contributed to manuscript revisions as part of the peer-review process for the following journals:*

Biomacromolecules
Molecular Pharmaceutics
Journal of the American Chemical Society (JACS)
Theranostics
Nanotoxicology
European Journal of Pharmaceutical Sciences
European Journal of Nanomedicine

## XI. REFERENCES

**Rangaramanujam M. Kannan**, Ph.D. (Doctoral thesis advisor)
Professor, Center for Nanomedicine, Ophthalmology, Johns Hopkins School of Medicine
400 North Broadway, Smith Building, RM 6023, Baltimore, MD, 21231
Phone: (443) 287-8634
Email: krangar1@jhmi.edu

**Sujatha Kannan**, MD. Ph.D. (Research advisor)
Associate Professor, Anesthesiology and Critical Care Medicine, Johns Hopkins School of Medicine
600N Wolfe Street, Blalock 901 Baltimore, MD 21287
Phone: (410) 955-7610
Email: skannan3@jhmi.edu

**Justin Hanes**, PhD.
Professor and Director of Center for Nanomedicine, Ophthalmology, Johns Hopkins School of Medicine
400 North Broadway, Smith Building, RM 6017, Baltimore, MD, 21231
Phone: (443) 287-7921
Email: hanes@jhu.edu